ANALYSIS AND DESIGN OF MEMS SCAN MIRRORS USING PERIODICALLY STIFFENED SILICON NITRIDE

by

Bert Jeffrey Lutzenberger

A dissertation submitted in partial fulfillment
of the requirements for the degree

of

Doctor of Philosophy

in

Civil Engineering

MONTANA STATE UNIVERSITY
Bozeman, Montana

April 2006

©COPYRIGHT

by

Bert Jeffrey Lutzenberger

2006

All Rights Reserved

APPROVAL

of a dissertation submitted by

Bert Jeffrey Lutzenberger

This dissertation has been read by each member of the dissertation committee and has been found to be satisfactory regarding content, English usage, format, citations, bibliographic style, and consistency, and is ready for submission to the Division of Graduate Education.

Dr. Robert Oakberg
Committee Chair

Dr. David L. Dickensheets
Committee Co-Chair

Approved for the Department of Civil Engineering

Dr. Brett Gunnink
Department Head

Approved for the Division of Graduate Education

Dr. Joseph J. Fedock
Interim Graduate Dean

STATEMENT OF PERMISSION OF USE

In presenting this dissertation in partial fulfillment of the requirements for a doctoral degree at Montana State University, I agree that the Library shall make it available to borrowers under the rules of the Library. I further agree that copying of this dissertation is allowable only for scholarly purposes, consistent with "fair use" as prescribed in the U. S. Copyright Law. Request for extensive copying or reproduction of this dissertation should be referred to Bell & Howell Information and Learning, 300 North Zeeb Road, Ann Arbor, Michigan 48106, to whom I have granted "the exclusive right to reproduce and distribute my dissertation in and from micoform along with the non-exclusive right to reproduce and distribute my abstract in any format whole or in part."

Bert Jeffrey Lutzenberger
April 2006

ACKNOWLEDGEMENTS

I would like to thank David Dickensheets for broadening my mechanics-centric perspective of the physical world. I would like to thank Robert Oakberg for reminding me just how important a mechanist's perspective can be. Thanks to both of you for helping me study this topic from both perspectives.

I would also like to thank my colleagues for many thought-provoking and insightful discussions. To Phil, Eric (Yanni), and Marshal, thanks for your help along the way.

To my family and friends, Mom, Dad, Julie, Jeremy, Christy, Steve, Harry, Virginia, Joanne, Vern, Shade and Tanner thanks for always believing in me.

Most importantly, to my loving wife and kids, Chris, Davey, Faith and John, thank you for all your sacrifices, help and support along the way.

TABLE OF CONTENTS

1. INTRODUCTION 1

Motivation 4
Device Overview 9
Material Properties 12
Research Overview 13
First Generation Prototype Devices 14
Second Generation Fabrication Run 16
Thesis Organization 17
Research Summary 18

2. MECHANICAL STIFFENING BACKGROUND 19

Introduction 19
Motivation 19
Stiffening Methods 22
Design Considerations 23
Micro Scale Stiffening Techniques 25
Stiffening Techniques 26
Rib-reinforced Structures 27
Sandwich Materials with Cellular Cores 31
Ribbed Shells 33
Finite Element Approach 33
Mechanical Stiffening Summary 34

3. FABRICATION 36

Chapter Overview 36
Fabrication facilities 36
Process Flow 36
Mirror Release 43
Sacrificial layer etch 44
Bulk silicon etch 49
Fabrication Summary 50

4. FIRST GENERATION BIAXIAL MICRO MIRROR 52

Background 52
Motivation 52
Fabrication and Release 53
Mechanical Characteristics 54

TABLE OF CONTENTS - CONTINUED

Optical Characteristics 56
Conclusion 62

5. VALIDATION OF DETAILED NUMERICAL MODELS 63

Resonant Frequency Experiment Setup 64
Cantilever Properties 65
Film Properties 66
Periodically Stiffened Cantilever Measurements 72
Conclusion 77

6. STIFFENED FILM MODELS 78

Film Parameters 79
Stiffness Analysis 80
Bending Stiffness 80
Flexural Rigidity 87
Effective Young's Modulus Calculation 93
Summary 102

7. MIRROR ANALYSIS AND NUMERICAL MODEL VALIDATION 103

Experimental Mirrors 103
Surface Profile Analysis and Characterizations 106
Electrostatic Force 106
Post-release Thermal Strain 113
Dynamic Deformation 118
Chapter Summary 122

8. DISCUSSION AND CONCLUSION 124

Fabrication Discussion 125
Fabrication Limitations 125
Mirror Discussion 126
Mirror Limitations 127
Modeling Discussion 127
Modeling Limitations 128
Future Work 128
Modeling Refinements 128
Self Assembled Devices 129
Conclusion 129

TABLE OF CONTENTS - CONTINUED

REFERENCES CITED..... 131

LIST OF TABLES

Table Page

1. Cross-section area and moment of inertia for different types of beams 28

2. Measured and predicted resonance for periodically stiffened cantilevers 76

3. Effective bending stiffness for silicon nitride stiffened with hexagonal cells 84

4. Coefficients for curve fit to bending stiffnesses given in Table 3 85

5. Effective bending stiffness for silicon nitride stiffened with square cells 87

6. Coefficients for curve fit to bending stiffnesses given in Table 5 87

7. Effective flexural rigidity for silicon nitride stiffened with hexagonal cells 91

8. Coefficients for curve fit to bending stiffnesses given in Table 7 91

9. Effective flexural rigidity for silicon nitride stiffened with square cells 92

10. Coefficients for curve fit to bending stiffnesses given in Table 9 92

11. Geometric parameters for the validation single axis mirror 105

LIST OF FIGURES

Figure Page

1. Conceptual images of micro mirrors 7

2. Three main fabrication layers and a released cantilever 9

3. SEM showing the cross-section of a micro cantilever 10

4. Depiction of a stiffened, single axis scan mirror 11

5. SEM of the back of a stiffened, single axis scan mirror 11

6. First generation biaxial scan mirror 15

7. FEA plot showing normal stress (x-direction) in the silicon and silicon nitride 21

8. FEA plot of normal stress near the boundary of the silicon and silicon nitride 22

9. Three cross-section with different bending rigidities 28

10. Plot of stiffen film rigidity versus equivalent un-stiffened film rigidity (0-6um) 30

11. Plot of stiff film rigidity versus equivalent un-stiffened film rigidity (0-50um) .. 30

12. Detail of the fabrication process 38

13. Detail of stiffened silicon nitride fins 40

14. SEM cross-section of a micro cantilever showing nitride, silicon and oxide 42

15. SEM showing a cross-section view of a silicon nitride fin 42

16. AFM output showing surface characteristics of the stiffened film 44

17. SEM showing residual oxide around etch vias 45

18. Cross-section of a partially released biaxial scan mirror 46

19. SEM showing how the silicon can undercut the silicon nitride 47

20. Surface profile of a scan mirror before and after residual oxide etch 48

LIST OF FIGURES – CONTINUED

Figure Page

21. SEM showing a rough bottom due to an aggressive silicon etch 50

22. Rib-reinforced biaxial scan mirror..... 55

23. Plot showing the step-response for both axes of a stiffened biaxial scan mirror.. 56

24. Front and back of a stiffened biaxial scan mirror 57

25. Schematic of an experimental optical switch 58

26. Plot of the poser loss in the experimental optical switch..... 59

27. Plot of power decoupling through the experimental switch 60

28. Surface profile across the optical surface of a stiffend biaxial mirror..... 61

29. Surface profile across the optical surface of a stiffend biaxial mirror..... 61

30. Schematic of experimental setup used to measure resonant frequency..... 65

31. Characteristic cell dimensions for each cell configuration..... 66

32. SEM close-up of the silicon nitride layer 67

33. Plot of experimental and predicted frequency response of a micro cantilever..... 68

34. FEA models of flat micro cantilevers..... 72

35. FEA model of a micro cantilver stiffened with x-oriented hexagonal cells..... 73

36. FEA model of a micro cantilver stiffened with y-oriented hexagonal cells..... 73

37. FEA model of a micro cantilver stiffened with y-oriented offset square cells..... 74

38. FEA model of a micro cantilver stiffened with x-oriented offset square cells..... 74

39. Tip response of micro cantilever stiffened with x-oriented hexagonal cells..... 75

40. Tip response of micro cantilever stiffened with x-oriented offset square cells.... 75

LIST OF FIGURES – CONTINUED

Figure Page

41. Tip response of micro cantilever stiffened with y-oriented offset square cells 76

42. Characteristic cell dimensions for square and hexagonal cell configurations 79

43. Geometry and boundary conditions for model used to find bending rigidity..... 82

44. FEA model showing vertical displacement of a detailed, stiffened cantilever..... 83

45. Effective moment of inertia for 25 and 50 um hexagonal cells..... 84

46. Effective moment of inertia for 25 and 50 um square cells..... 86

47. Geometry and boundary conditions for the model used to find flexural rigidity . 89

48. FEA model showing the vertical displacment of a detailed, stiffened plate..... 89

49. Effective flexural rigidity for 25 and 50 um hexagonal cells 90

50. Effective flexural rigidity for 25 and 50 um square cells 92

51. Geometry and boundary conditions for models used to determine E_{eff}..... 95

52. FEA model showing vertical displacment of a detailed, stiffened cantilever 96

53. FEA model showing vertical displacment of a simplified cantilever using E_{eff}... 97

54. FEA model showing vertical displacment of a detailed, stiffened cantilever 98

55. FEA model showing vertical displacment of a simplified cantilever using E_{eff}... 99

56. FEA model showing vertical displacment of a simplified cantilever using E_{eff}. 101

57. Single axis scan mirror stiffened with hexagonal fins..... 104

58. Front and back of a single axis scan mirror stiffened with hexagonal fins 105

59. Plot of voltage versus rotation for a 1500 um diameter single axis scan mirror 108

60. FEA model showing the electrostatic load and resulting mirror rotation..... 109

LIST OF FIGURES – CONTINUED

Figure Page

61. FEA model showing nodal rotation due to an electrostatic load 110

62. Plot of nodal rotation shown in Figure 61 111

63. Plot of nodal rotation for a stiffened mirror with an electrostatic load..... 112

64. Interference fringes across the optical surface of single axis scan mirror 115

65. Surface profile of 1500 um diameter mirror stiffened with 50 um square cells . 116

66. Surface profile of 1500 um diameter mirror stiffened with 25 um square cells . 116

67. Surface profile of 1500 um diameter mirror stiffened with 50 um hex cells..... 117

68. Surface profile of 1500 um diameter mirror stiffened with 25 um hex cells..... 117

69. Predicted surface deformation of an unstiffened mirror due to interia..... 120

70. Measured surface deformation due to inertia for 25 um square cell mirror 121

71. Measured surface deformation due to inertia for 50 um hexagonal cell mirror . 121

72. Predicted surface deformation of a stiffened mirror due to interia at 15 kHz 122

73. Depiction of how cell size can limit etch rate during an anisotropic etch 126

ABSTRACT

This research presents a novel fabrication method combining surface and bulk micromachining techniques to deposit mechanically stiffened silicon nitride films for use in MEMS fabrication. The stiffened silicon nitride film consists of a thin (~1.5 um) top sheet with stiffening fins molded to the back of the film. In the final configuration, the fins extend between 15 um and 40 um vertically from the back of the film. The molded fins are arranged into periodic square and hexagonal cell configurations ranging in size from 10 um to 250 um. The periodic cells significantly increase the bending stiffness of LPCVD silicon nitride films resulting in a film with a high strength-to-weight ratio.

Larger aperture, silicon nitride micro mirrors are fabricated with the mechanically stiffened silicon nitride film. The mirrors demonstrate that deformation due to post-release thermal strain and inertia during dynamic actuation can be mitigated by employing the proposed stiffening technique. Furthermore, the mirrors are fabricated with a minimal amount of processing making the proposed microfabrication technique an attractive solution for various MEMS applications

Finally, homogenized material properties are obtained for the periodically stiffened silicon nitride film. The homogenized material properties are then used to simplify finite element models of biaxial and single axis torsion micro mirrors fabricated from the proposed film. The resulting finite element models are shown to be in excellent agreement with the experimental models. The presented numerical analysis method significantly simplifies model complexity while simultaneously reducing the computational cost associated with simulating MEMS built from a periodically stiffened thin film.

CHAPTER 1

INTRODUCTION

In 1982, the first mass-produced micro-electromechanical system (MEMS) entered high volume production. This device, a micromachined automotive manifold pressure sensor, marked the first successful use of MEMS in a commercially available product. It was quickly followed by a micromachined disposable blood pressure sensor in 1983 [20]. The financial success of these mass-produced micro systems set the stage for a new field of research and development focused on producing high performance micro electromechanical systems. Since that time, MEMS have changed the nature of many high technology industries including biomedicine and telecommunications and personal entertainment. Some of the most familiar commercial applications utilizing MEMS technology include projection displays [14], ink-jet print heads, accelerometers, and optical switches [1].

Despite the pervasive use of MEMS in modern technology, present microfabrication processes limit the complexity of such systems. In particular, the planar nature of standard microfabrication techniques such as photolithography, thin film deposition, etching and wafer bonding, imposes significant restraints on modern MEMS. This fundamental restriction results in MEMS with minimal surface topography, limited complexity and low mechanical efficiency.

A further restriction in MEMS design results from the use of thin films as primary structural materials. The most commonly used thin films such as silicon dioxide, silicon

nitride and polysilicon serve as lightweight structural materials with excellent optical and electrical properties. However, these materials lack bending rigidity due in large part to the manner in which they are deposited. Thin films are typically deposited onto a substrate material such as silicon using low-pressure chemical vapor deposition (LPCVD), plasma-enhanced chemical vapor deposition (PECVD) and plasma sputtering. While each of these techniques allow for precise control over the thickness of the deposited film, they also result in a flexible film with minimal surface topography.

Most notably, LPCVD films are often desired due to the high quality of the film resulting from this deposition technique. Although low-pressure deposition produces an optically smooth thin film with a uniform cross-section, thermal stresses develop in the unreleased film once the film and substrate composite is removed from the deposition furnace and allowed to cool to room temperature. The development of thermal stress occurs due to the combination of elevated deposition temperature (above 600º C) and a CTE (coefficient of thermal expansion) mismatch between the deposited film and substrate material. Once the film is released from the substrate, the film undergoes strain as the built-in stress relaxes[1]. This delayed strain coupled with the compliant nature of LPCVD films can lead to significant deformation in a device once it has been selectively released from the substrate.

Built-in stress in an unreleased film can be determined by comparing the curvature of a wafer before and after film deposition. At this stage of fabrication, the built-in initial stress is relatively inert and apparently harmless. However, when

[1] This phenomenon is often referred to as residual stress in MEMS literature. A distinction is made here to emphasis the mechanism leading to the delayed strain once the material is released from the substrate.

selectively patterned and released from the substrate the release of built-in stress can cause the film to curve or cup away from the substrate. This phenomenon imposes significant geometric, mechanical and optical constraints on MEMS fabricated from thin films.

Adding vertical fins to a thin film can increase its bending stiffness by increasing its cross-sectional moment of inertia. Fins can be added by etching vertical trenches into a <100> silicon wafer forming a mold onto which a thin film can be deposited. Orienting the trenches in a periodic pattern such as a repeated hexagon or square mesh will result in a deposited film with periodic stiffening ribs molded to the backside of the film. In order for the resulting material to be of practical interest to the MEMS community a design methodology for the stiffened film is required. Specifically, material models are needed to aid the design and optimization of devices fabricated from the proposed stiffened film.

This research will address the challenge of designing and fabricating MEMS using stiffened thin films. A novel fabrication technique to produce a structurally stiffened LPCVD silicon nitride film will be employed. The resulting material will retain the excellent optical and electrical properties of a traditional LPCVD silicon nitride film with the added benefit of increased flexural rigidity and a high strength-to-weight ratio. Numerical models of the stiffened film will be presented. The models will account for the cell geometry including cell size, cell type, fin thickness and fin height.

In order to fully address the challenges of designing and fabricating MEMS with a structurally stiffened thin film this research will be divided into two phases:

1. A fabrication technique will be developed to produce a periodically stiffened LPCVD silicon nitride film. In a series of design/build iterations, several micro mirrors and micro cantilevers will be fabricated with the proposed film.
2. Numerical models will be developed that predict the behavior of MEMS fabricated with the film. The models will rely on an averaging technique to develop a homogeneous constitutive model for the cellular material thus significantly simplifying numerical computations. Numerical models will be used to simulate devices built in Phase 1. These simulations will be compared with experimental devices to validate the proposed constitutive model.

Ultimately, a fabrication technique with the accompanying homogeneous constitutive model and design methodology will be presented as a method to efficiently design, fabricate, analyze and optimize MEMS built from periodically stiffened thin films. This research will represent a significant advance in both microfabrication technology and the mechanical analysis of MEMS fabricated with periodically stiffened thin films.

Motivation

Traditionally, microfabrication has consisted of two dominant techniques. *Surface micromachining* is the process whereby thin films are deposited and extruded over the substrate and/or sacrificial layers. *Bulk micromachining* is the process whereby bulk portions of the substrate are removed to define a device. Traditional MEMS were often either surface or bulk micromachined. However, many modern microfabrication

techniques, including the technique presented in this research, have combined both techniques to yield unique and useful devices.

Thermal stress in a deposited film must be considered when choosing surface micromachining techniques. Thermal stresses arise after a film has been deposited and removed from the deposition furnace. Because of these built-in stresses, devices with high length-to-thickness ratios can deform considerably when released from the substrate. For example, the tip of a prismatic cantilever beam fabricated from low-stress, low-pressure chemical-vapor deposited (LPCVD) silicon nitride will tend to bend upward when released from the substrate. This phenomenon can lead to undesirable and sometimes catastrophic deformation in a released device.

One class of device particularly sensitive to surface deformation are micro optoelectromechanical systems (MOEMS) such as micro mirrors. Micro mirrors are useful in miniaturized optical systems such as optical cross-connects and scanned-beam imaging systems. Large aperture micro mirrors with high resonant frequencies and low actuation voltages are often desirable for these systems. High performance micro mirrors can be achieved by fabricating mirrors from an optically smooth thin film like LPCVD silicon nitride.

Silicon nitride is an attractive and readily available microfabrication material, exhibiting excellent mechanical, optical and electrical properties. However, as with many micromachining materials, it must be deposited as a thin film to achieve these qualities. LPCVD silicon nitride is typically deposited across a 4, 6 or 8-inch silicon wafer at a deposition rate in the range of 3 nm to 4 nm per minute yielding a smooth, uniform layer

of silicon nitride on the order of microns in thickness. However, this process is slow. For example, at an assumed deposition rate of 3.5 nm per minute a 2.5 um layer of silicon nitride takes approximately 14 hours including 1 hour ramp-up and ramp-down phases in the deposition chamber. Since deposition rate is relatively constant over time a 5 um layer of the same film can require in excess of 26 hours. At such slow deposition rates depositing any more than around 5 microns of silicon nitride is a costly step in the overall fabrication cycle.

Furthermore, it is often desirable to minimize the mass of the MEMS, particularly for torsion scan mirrors since a lower mass translates directly to a higher resonant frequency. Clearly, it is desirable to minimize the thickness of the film while maximizing or at least maintaining adequate stiffness.

CTE mismatch between the silicon, silicon-nitride and reflective layers is inevitable in MEMS. This CTE mismatch coupled with elevated deposition temperatures can cause devices to deform significantly once they have been released from the substrate. The resulting deformation can in turn lead to excess insertion loss in optical switches and poor fidelity in imaging systems. While it is understood that built-in stress can be partially reduced by: 1) controlling deposition conditions, 2) annealing deposited films, and 3) depositing multiple layers of films to balance stresses in a laminate structure; each of these solutions has limitations. Deposition conditions remain variable in most systems, maximum annealing temperature is material dependent and laminated structures can be tedious to fabricate. Furthermore, the film must be able to resist bending due to forced vibration, especially in optical devices that often require high-speed

actuation. A solution is needed that can increase the tolerance of a design to variations in film stress and inertia effects while maintaining a simple and efficient fabrication process.

Obviously, increasing the cross-sectional moment of inertia of a micromachined structural material can significantly reduce deformation due to the release of internal stress in MEMS fabricated with thin films. An ideal solution would adequately increase the moment of inertia of a film while minimizing the complexity of the associated fabrication process. Attempts have been made to produce mechanically stiffened thin film structural materials. MEMS fabricated from thin structural materials have employed vertical, high aspect ratio geometries to increase the bending stiffness of a structural material while minimizing additional mass added to the system [21], [27]. Figure 1 depicts two examples. The figure on the left shows a conceptual corrugated mirror similar to those fabricated by Lin et. al (2000), while the figure on the right depicts a rib stiffened micro mirror.

It is has been clearly demonstrated that micromachined vertical stiffeners result in structural materials with high strength-to-weight ratios [21]. However, little research has been conducted on the mechanical properties of materials resulting from these techniques making them useful only for specialized applications usually involving multiple design/build iterations.

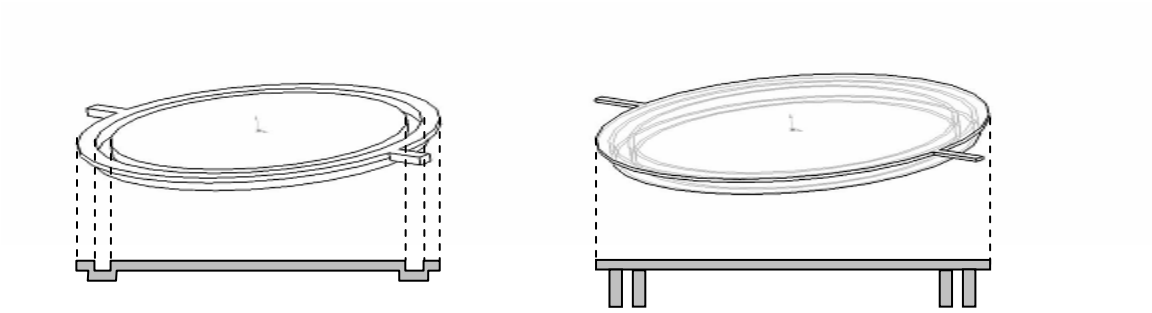


Figure 1 Two conceptual images of micro mirrors showing corrugated and ribbed stiffeners.

This research addresses these problems by proposing a novel and efficient process to produce mechanically stiffened surface micromachined structures fabricated from a thin film of silicon nitride (on the order of microns thick), with nearly arbitrary control over the depth and pattern of the vertical stiffening fins. The film significantly reduces deformation due to the release of built-in stress as well as deformation due to forced oscillation as demonstrated by several torsion micro mirrors. An average Young's modulus and Poisson ratio will be obtained for the material. This will be accomplished by assuming that the periodically stiffened material can be treated as a homogenous material. This assumption will require that the size of each individual cell remains small relative to the overall scale of the stiffened device. The averaged material properties will be used to simplify finite element simulations of micro cantilevers, single axis torsion micro mirrors and biaxial torsion micro mirrors. Experimentally obtained deformed shapes of several torsion micro mirrors will validate the finite element models showing that homogeneous material properties can be used to adequately model MEMS fabricated with periodically stiffened thin films.

Device Overview

Figure 2 depicts a typical released micro cantilever with two vertical molded stiffeners running the length of the beam. The proposed microfabrication technique consists of three essential layers as depicted in Figure 2. A bulk silicon etch is performed defining trenches which are subsequently filled with a conformal layer of silicon nitride (~1.5 um). A sacrificial oxide layer is deposited between the silicon and silicon nitride layers to give an aqueous anisotropic silicon etchant access to the silicon. The sacrificial oxide layer is removed with an aqueous hydrogen fluoride (HF) etch. The bulk silicon is then etched in a tetra methyl ammonium hydroxide (TMAH) solution. An additional metal layer, not shown in Figure 2, may be selectively deposited on the silicon nitride devices to serve as a reflective and/or conductive layer.

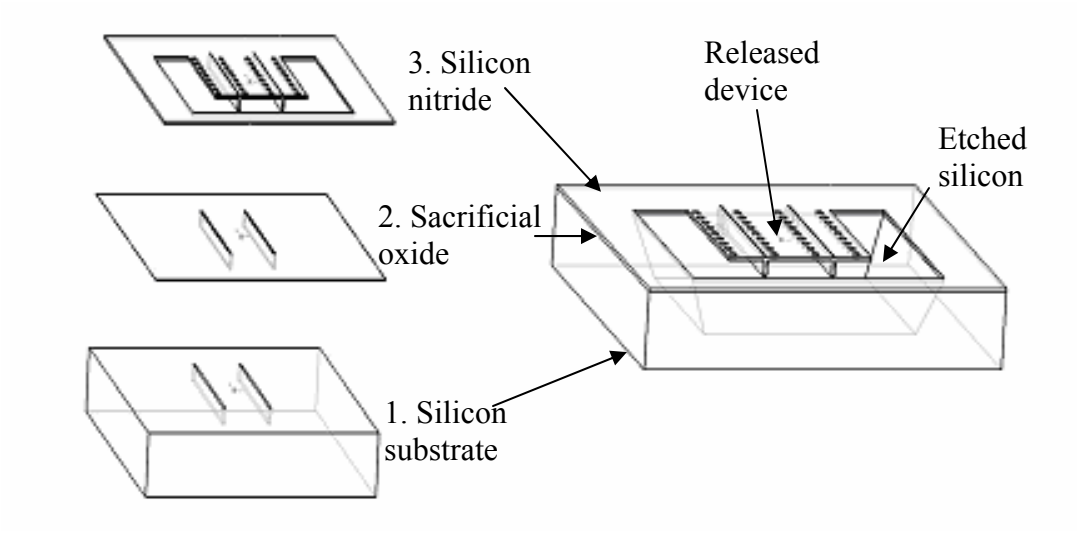


Figure 2 This figure shows the three main layers in the fabrication process along with a depiction of a released micro cantilever. The depiction on the left shows an expanded view of the silicon-nitride, oxide and etched silicon substrate while the image on the right shows a molded silicon-nitride cantilever suspended over an etched silicon substrate.

Figure 3 shows the cross-section of a micromachined cantilever beam. In this figure the sacrificial oxide has been removed clearly showing the separation between the silicon and silicon nitride within the etch window. An anisotropic etch in TMAH or KOH is required to fully release the beam.

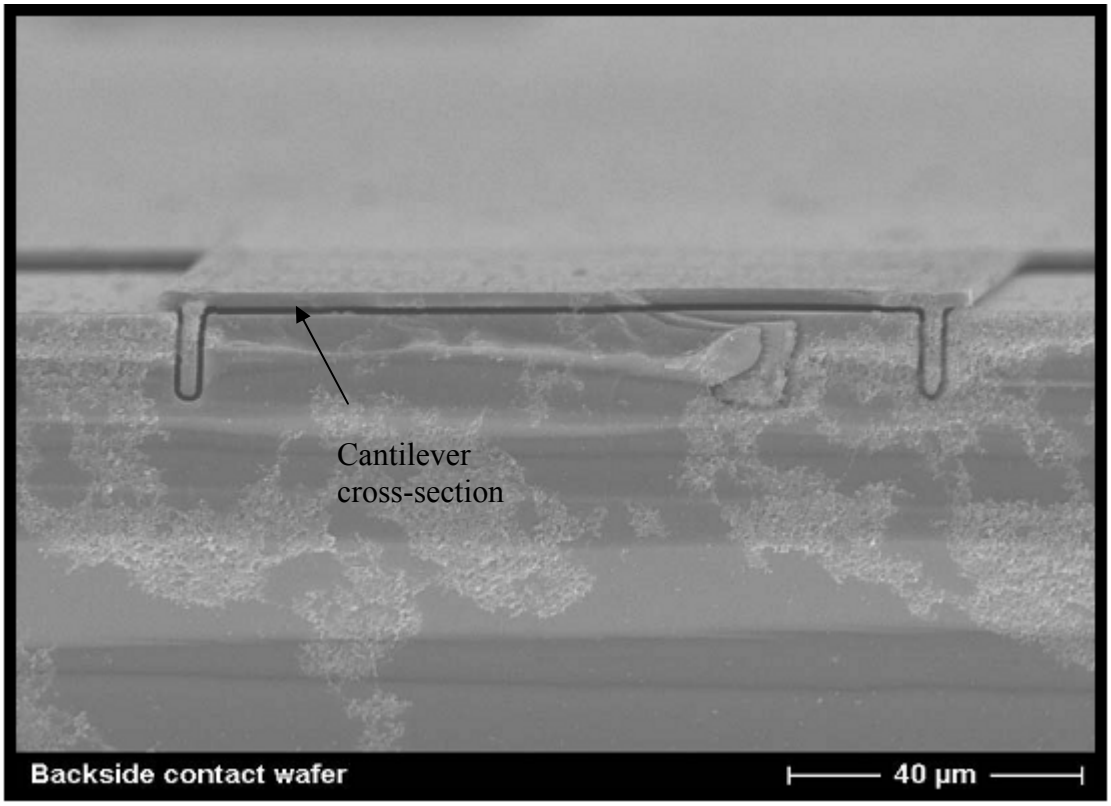


Figure 3 The scanned-beam electron micrograph in this figure shows the cross-section of a micro cantilever similar to the one depicted in the Figure 2. The oxide layer has been etched to enhance the contrast between the silicon substrate and the silicon-nitride structural material.

Figure 4 depicts a single axis micro torsion mirror fabricated with a periodically stiffened film. Average or bulk material properties will be obtained for the periodically stiffened silicon nitride film depicted in this figure. The bulk material properties can then be used to simplify modeling efforts to simulate MEMS constructed from the proposed

mechanically stiffened silicon nitride film. Figure 5 shows a scanning electron micrograph (SEM) of the backside of a large area single axis scan mirror stiffened with 50 um honeycomb cells.

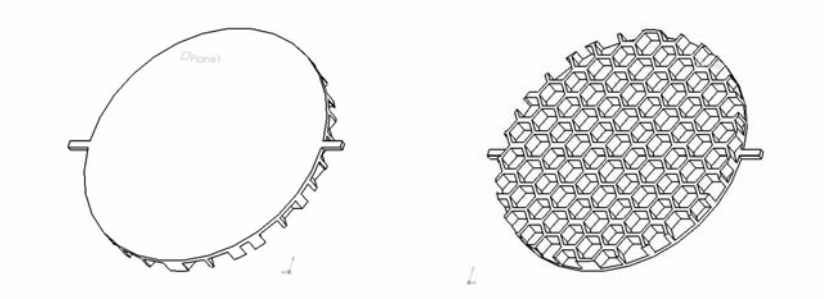


Figure 4 This figure depicts the front and back of a simple single axis scan mirror fabricated with a periodically stiffened thin film.

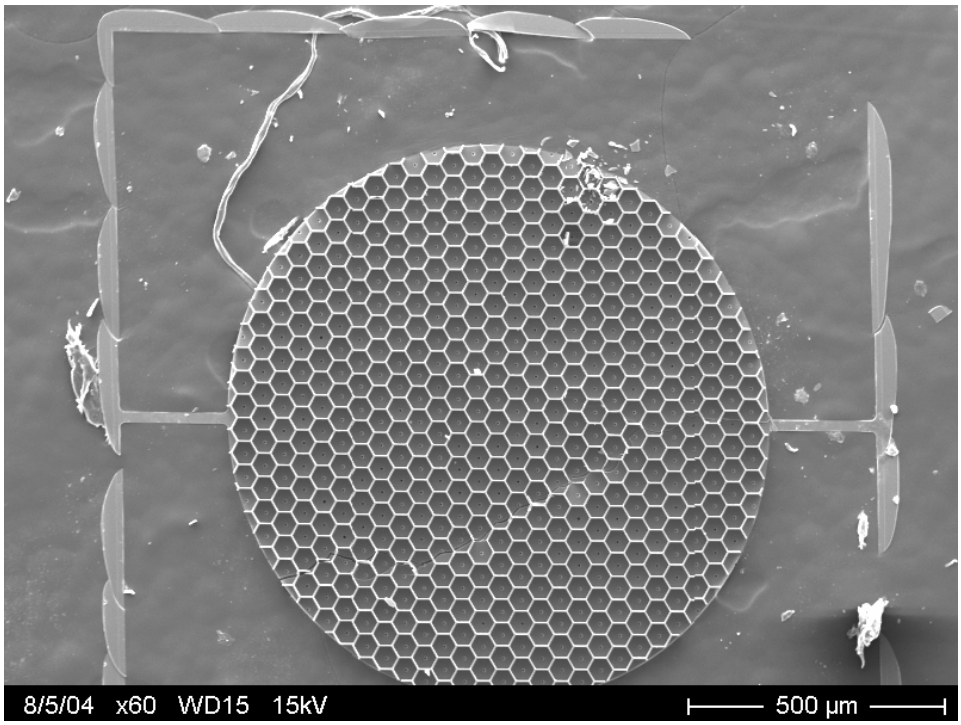


Figure 5 The SEM in this figure shows the back of a single axis scan mirror fabricated from a mesh of 50 um hexagons.

Material Properties

MEMS fabricated with periodically stiffened thin silicon nitride films can be tedious to simulate. A naïve numerical simulation might consist of a finite element model with each individual cell of the stiffened film explicitly modeled. This modeling approach has severe limitations. Specifically, as the overall dimensions of the MEMS to be simulated becomes large relative to the cell size, the finite element model quickly becomes computationally expensive. As an alternative approach, the periodically stiffened material can be approximated as a homogeneous material if the cell size remains small relative to the characteristic dimensions of the model. This latter approach, which has been successfully used on large-scale sandwich laminate materials for decades [4], will be adopted for this research.

Asymptotic homogenization analysis is applicable for a material when the period of regular, periodic structures is much smaller than the characteristic dimensions of a material. Homogenized models of plates with periodic inhomogeneities were developed in this way by Duvaut [7], Duvaut and Metellus [8], Artola and Duvaut [3] and, most recently, Andrianov and Manevich [2]. The most recent work by Parton and Kudryavtsev [28] presents a concise analysis of the current state-of-the-art in homogenized plate theory. In this research, I will show that the stiffened film can be treated as a homogenized material under certain circumstances. Due to the film's asymmetric cross-section, however, the equations presented by the above authors cannot be directly applied to periodically stiffened silicon nitride films. Therefore, a numerical

method for quickly obtaining material properties that is valid for almost any periodic cell is proposed.

Experimentally obtained material properties will be compared with results obtained by numerical models. The numerical results will be obtained with finite element models of stiffened micro cantilevers.

The homogenized material will be treated as a transversely isotropic material. It is important to note that in general the material properties require a fully anisotropic material model if the cell geometry becomes exceedingly complex. In this research, we consider simple square and hexagonal cells, which are treated, as transversely isotropic due symmetry. The homogenized material properties will be used to simplify modeling efforts to simulate MEMS constructed from the proposed mechanically stiffened silicon nitride film. The technique will be demonstrated on finite element models of single axis and biaxial micro mirrors. Numerical simulations of surface deformation due to the release of built-in stress and force vibration of single axis micro mirrors will be shown to be in good agreement with experimental results.

Research Overview

This research presents a fabrication method combining surface and bulk micromachining techniques to deposit mechanically stiffened silicon nitride films for use in MEMS fabrication. Biaxial and single axis micro mirrors are fabricated with the proposed technique. The stiffened silicon nitride film consists of a thin (~1.5 um) top sheet with stiffening fins molded to the backside of the film. In the final configuration, the fins extend 35 um vertically from the backside of the top sheet. The molded fins

consist of periodic square and hexagonal cells. Cells range in size from 10 um to 250 um. Homogenized material properties are obtained for the periodically stiffened silicon nitride film. The homogenized material properties are then used to simplify finite element models of biaxial and single axis torsion micro mirrors. The resulting finite element models are shown to be in good agreement with the experimental models.

First Generation Prototype Devices

Silicon nitride mirrors and test structures were fabricated at the Stanford Nano-fabrication Facility (SNF) in 2001 and 2002. This fabrication run produced biaxial micro mirrors and test structures made of mechanically stiffened silicon nitride [23]. Mechanical stiffening was achieve by depositing a thin film of silicon nitride onto an etched silicon mold to form a thin structural film with vertical stiffeners molded to the backside of the silicon nitride film. The resulting mechanically stiffened devices minimized surface deformation due to thermal stress and forced vibration. Several test structures were used to characterize the material properties of silicon nitride film. The test structures included Guckle rings [11], pointing devices [34] and cantilever beams [10]. The test structures and mirrors provided proof-of-concept devices supporting the use of mechanical stiffeners on electrostatically actuated MEMS devices using silicon nitride as a structural material.

Biaxial mirrors with optical surfaces up to 400 um in diameter were successfully fabricated from a 1.5 um thick layer of silicon nitride with mechanical stiffening flanges. These mirrors can be considered “stretched-film” mirrors since the optical surface was not stiffened but rather supported by a latticed stiffening frame around the perimeter of

the optical surface as shown in Figure 6. In this research, I consider both stretched-film and fully stiffened mirrors.

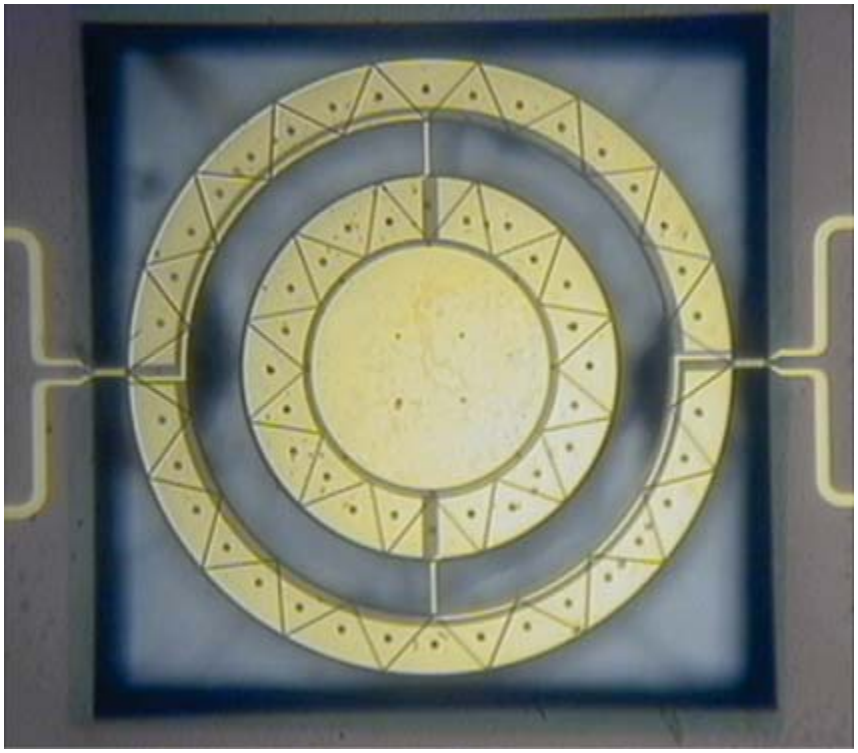


Figure 6 This figure shows a first generation biaxial "stretched-film" scan mirror. The optical surface (inner disk) for these mirrors was supported by a latticed stiffening frame at the perimeter of the inner disk leaving the actual optical surface free of stiffening ribs.

A 1x2 optical switch was constructed with these mirrors, demonstrating their usefulness as switch elements in optical systems [23]. These devices inspired a second-generation fabrication focused on further characterizing the mechanically stiffened silicon nitride film and achieving larger diameter micro mirrors.

Second Generation Fabrication Run

A second fabrication run was completed in 2004. This fabrication run used a new mask set based on the concepts and results gathered from the first fabrication run. The new mask set refined the stiffening technique by focusing on periodic stiffening structures. Hexagonal and square patterns were used for the periodic stiffening structures.

Cantilever beams constructed in this fabrication cycle were used to obtain the bending stiffness of the mechanically stiffened film. These test structures were vibrated with a piezo-electric material using a varying frequency sinusoidal input signal. The fundamental frequency corresponding to beam bending was used to obtain the bending rigidity of the film.

The test structures were also mechanically loaded by an atomic force microscope (AFM) [29]. The AFM was operated in contact mode in an attempt to achieve a known deflection and a corresponding force. Force versus deflection measurements were intended to be used to determine the bending rigidity of the micro cantilevers. Unfortunately, this experiment was found to be unreliable due to difficulties in calibrating the AFM.

Finally, several large area biaxial and single axis torsion micro mirrors were fabricated to demonstrate the improved flatness control and increased size of devices achieved with mechanically enhanced silicon nitride films. The demonstration devices were fabricated with periodic stiffeners to improve the stiffness of the devices while maintaining a high strength-to-weight ratio.

Thesis Organization

This thesis is divided into theory, fabrication, first generation device characterization, second-generation device design, material property analysis, and conclusion chapters. The theory chapter discusses homogenization theory and presents past and previous work related to mechanically stiffened thin films. The microfabrication technique presented in this research produces a stiffened film similar to a sandwich laminate structure devoid of a bottom sheet. This slight modification significantly alters traditional theory for sandwich laminates with heterogeneous core materials and requires special attention.

The fabrication chapter describes the mixed surface and bulk micromachining technique used to create mechanically stiffened silicon nitride films. Both fabrication and release processes are covered in the fabrication chapter. The chapter on first generation devices presents data collected on biaxial mirrors fabricated with mechanically stiffened silicon nitride. Mechanical and optical measurements were made for the mirrors produced during this fabrication cycle and a two port optical switch was demonstrated. The second-generation device design chapter details efforts to produce flat, lightweight micro mirrors using the knowledge gained from the first generation fabrication cycle. This chapter also discusses test structures used to obtain homogenized material properties including homogenized Young's modulus and homogenized Poisson's ratio for hexagonal and square cells over several cell sizes. A detailed analysis of biaxial and single axis mirrors is also presented. The mirror analysis includes static and dynamic surface profile measurements illustrating flatness control of the film.

The material property analysis chapters discuss the homogenization of the periodically stiffened silicon nitride. Experimental results are compared with finite element results. The material properties are then used to simplify finite element models of several biaxial and single axis mirrors. Finally, the conclusion chapter gives a detail discussion of using homogenized material properties to simulate periodically stiffened silicon nitride films. Performance of the mirrors is also discussed. A brief discussion of possible future work is also presented.

Research Summary

Periodic stiffeners will be shown to significantly increase the bending stiffness of LPCVD silicon nitride films while achieving a high strength-to-weight ratio. Larger aperture, silicon nitride micro mirrors were achieved with the mechanically stiffened silicon nitride film. The film adequately controlled deformation due to post-release thermal strain and inertial effects. The heterogeneous silicon nitride film was successfully modeled as a homogenized material resulting in accurate simulations for biaxial and single axis torsion mirrors at a reduced computational cost. Fabrication of the mirrors was achieved with a minimal amount of processing making the proposed microfabrication technique an attractive solution for various MEMS applications. The presented numerical analysis method was shown to simplify model complexity while simultaneously reducing the computational cost associated with simulating MEMS build from a periodically stiffened thin film.

CHAPTER 2

MECHANICAL STIFFENING BACKGROUND

Introduction

MEMS are commonly fabricated from materials such as, silicon, polysilicon, and silicon nitride (Kovacs, 1998). These films are either deposited onto a substrate material or patterned from the substrate itself. Low-pressure chemical vapor deposition (LPCVD) is an attractive deposition technique that results in a smooth thin film with excellent electrical properties. Designing MEMS with mechanically flexible films deposited in this manner can severely limit the mechanical and geometric characteristics of a device. Several attempts to overcome this limitation have been employed [16], [21], [17], and [18].

Motivation

When dealing with optical MEMS there are three major design considerations driving the need for stiffer structural microfabrication materials. First, the material must be rigid enough to resist surface bending due to electrostatic actuation. The material must also resist bending due to inertial accelerations during dynamic oscillation. Finally, the material must be capable of resisting curvature due to post-release thermal strain.

The mirrors considered in this work are driven by electrostatic actuation. Electrodes on the mirror surface are energized while the substrate under the mirror is grounded. This creates an electric field and produces a torque on the mirror causing it to

rotate about the flexures of the mirror. This type of actuation was chosen because of its simplicity and effectiveness. However, electrostatic actuation requires the mirror surface be as rigid as possible to resist deformation as the electrodes are energized and pulled toward the substrate.

Secondly, since these mirrors are proposed for scanning applications, the mirror surface must resist bending during dynamic oscillation. In this case, the mirror is considered to be oscillating at speeds and amplitudes capable of producing significant inertia on the mirror. The resistance of motion (inertia) can cause the mirror surface to deform as the mirror oscillates, especially when the mirror rotation is at its maximum amplitude. At this point, the kinetic energy in the system goes to zero while the potential energy is maximized. Ideally, the potential energy in a scan mirror would be stored only in the flexures but in reality, some of the potential energy is stored by deforming the mirror surface since it is not perfectly rigid. This dynamically induced deformation must be minimized in order to maintain fidelity in an optical wavefront.

Finally, the mirror surface must adequately resist post-release thermal strain in the fabricated film. Thermal stress develops in the film through a combination of elevated deposition temperature (above 600º C) and a CTE (coefficient of thermal expansion) mismatch between the deposited film and substrate material. When the film is deposited onto the silicon substrate the thermal stress in the material is approximately zero. However, once the composite material is removed from the deposition furnace each of the layers tend to shrink by a different amount. The constraint at the interface between the silicon nitride and silicon substrate results in a stress differential. Once released from the

substrate the film strains as the built-in stress relax. The CTE mismatch between the silicon nitride (CTE ~= 3.6e-6 1/ºC) and the silicon substrate (CTE~= 2.6e-6 1/ºC) results in a net tensile thermal stress in the silicon nitride film [25]. The delayed strain resulting from this tensile stress coupled with the compliant nature of LPCVD films can lead to significant deformation in a device once it has been selectively released from the substrate. Figure 7 shows the predicted normal stress in each layer of material once it has been removed from the furnace and cooled to room temperature. In this analysis, the silicon nitride layer is given a CTE of 3.6e-6 1/ºC and the silicon layer is given a CTE of 2.6e-6 1/ºC. The initial temperature has been set to 700ºC and then cooled to 20ºC resulting in a temperature change of 680ºC. The finite element simulation shows the normal stress in the silicon nitride layer near the center of the model to be approximately 94 MPa which agrees well with the experimental result of approximately 90 MPa based on Guckel ring measurements [11].

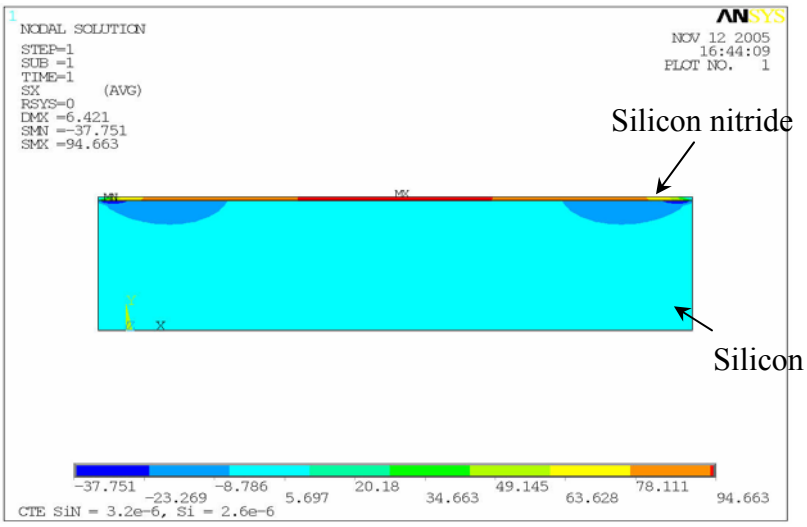


Figure 7 The finite element model in this figure shows the normal stress in the unreleased silicon nitride layer to be approximately 94 MPa which agrees well the measured results of 90 MPa.

Figure 8 shows a close up of the right edge of the model clearly showing a significant stress gradient.

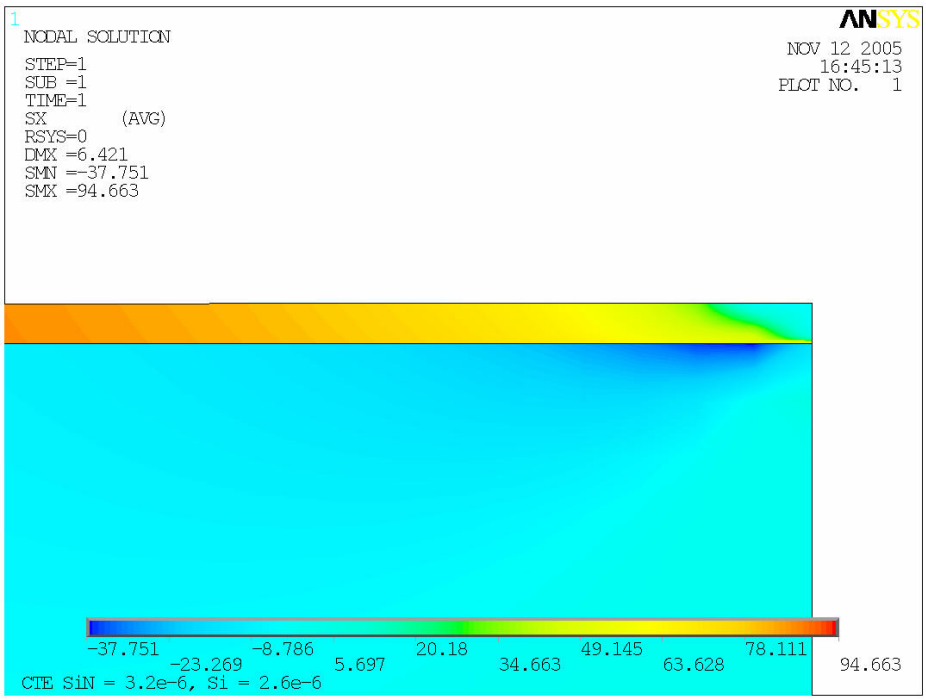


Figure 8 The finite element model in this figure shows the normal stress distribution near the edge of the silicon/silicon nitride composite.

Stiffening Methods

The most common method to achieve a stiffer structural material is to employ a bulk micromachining process. With bulk micromachining techniques, a much thicker structural material can be achieved [12]. However, this technique yields a material with a limited strength-to-weight ratio and the choice of materials for such a method is limited. While a deep reactive ion etch on the backside of a bulk micromachined device can be used to selectively remove material and increase the strength-to-weight ratio, this approach can be tedious and additional precautions must be taken to protect the front side

of the material. An additional bonding step may also be required to mount actuation or grounding electrodes under the device after backside etching.

Alternatively, MEMS fabricated from thin structural materials can employ molded vertical stiffeners and corrugations to increase the bending stiffness of the structural material while minimizing additional mass added to the system. A film of this type is both light weight and rigid making it ideal for micro-optical devices.

Several useful devices have been fabricated from molded thin films that demonstrate increased bending stiffness due to vertical stiffeners. These devices include micro mirrors, polysilicon cantilevers, and accelerometers [16], [27] and [18]. Techniques to produce corrugations and vertical fins rely on a deep reactive ion etch (DRIE) to form a mold into the substrate, which is back-filled with a film to obtain a molded, stiffened material.

Design Considerations

Once a process to produce molded fins or corrugations in a film has been selected, a corrugation pattern must be selected early in the initial design phase. For example, periodic stiffening cells such as a honeycomb structure may be an ideal solution for general stiffening, as this configuration can simplify design details. However, such a general periodic stiffening scheme may not result in the most efficient device since stiffening fins can be tailored to fit the specific geometry of a device thus achieving an optimal strength-to-weight ratio. This latter solution may be beneficial when the device specifications and tolerances are well known.

In addition to the stiffening techniques mentioned above, asymmetrical stiffeners coupled with thermal stain in MEMS-based structural materials can result in a novel method to control deformation in a film. For example, this technique can be used to control the twist in a released cantilever. While not addressed in detail in this thesis, devices demonstrating this behavior have been fabricated and measured [24].

Ultimately, with adequate knowledge of the mechanical behavior of periodically stiffened films it is possible to treat the material as homogeneous. By applying a homogenization technique to periodically stiffened thin films, numerical simulations can be greatly simplified. However, in order to validate numerical models, a thorough set of test devices is required to characterize the stiffened film.

One goal of this research is to establish test cases that demonstrate the use of periodic stiffening structures in MEMS design and obtain homogenized material properties for these materials. To achieve this, several micro cantilevers will be tested. The micro cantilevers will be used to obtain the bending rigidity and Poisson ratio for a variety of hexagonal and square cells. Numerical model that accurately predict the bending rigidity and Poisson's ratio of the micro cantilevers will be created. Once the numerical models have been shown to be in agreement with experimental results, the numerical modeling methodology will be proposed as an accurate and rapid means to predict the homogenized material properties of periodically stiffened films with arbitrary cell shape and size.

Micro Scale Stiffening Techniques

Before proposing any fabrication or analysis methods, however, we first consider recent research in this area. Currently there are several groups contributing research to the field of micro scale thin film stiffening. One of the most notable research efforts has come from Keller and Howe [18]. Keller and Howe introduced a method to create a structured, high aspect ratio polysilicon mesh using a surface micromachining technique aptly referred to as HEXSIL. The technique has been used to fabricate mechanically and thermally actuated micro tweezers for assembling MEMS components. The process was also used to produce read heads for data storage devices [15]. Keller and Howe also presented a method to visually detect device release by building stress gradients into cantilever HEXSIL beams [17].

However, the first and perhaps most seminal work of Jerman in 1990 [16] showed that thin membranes could be stiffened with corrugated rings on the perimeter of the membrane. More recent work conducted by Lin and Fang [22] applied Jerman's results to create corrugated cantilever beams and micro mirrors. Fang and Lin used corrugated cantilever beams fabricated from silicon nitride to demonstrate the effects of corrugation width on bending stiffness. Their studied of several cross-sectional configurations supported the theoretical prediction that maximum bending stiffness was achieved at the intermediate cross-sectional shape between T- and channel-shaped corrugations.

Recently, sandwich laminate beams with periodic cellular cores such as hexagonal honeycombs have been successfully fabricated [33]. Whitesides et. al. molded stiffening structures with soft lithography and used adhesives to bond a thin material to a

high aspect ratio frame producing a micro sandwich laminate material. However, their fabrication technique appears to be limited in its use for MEMS devices and is must be kept below the melting point of PMMA (Poly methyl methacrylate) once infused with the polymer. Whitesides et. al. performed four-point bending tests on sandwich beams measuring 1 mm to 3 mm in length.

Another notable effort from Berkeley was conducted by Muller et. al. [27]. Their work focused on rib-reinforcement techniques to stiffen micromachined beams. Muller et. al. used the molded polysilicon structures introduced by Keller and Howe [18] to reduce cross-axis sensitivity of flexures and avoid coupled-mode response in a gimbaled micro actuator.

The research presented in this thesis focuses on achieving stiffened thin films using principles similar to those presented by Keller and Howe and Muller et. al.. In this research, however, I present a numerical method to simplify the analysis and design of MEMS fabricated with thin films stiffened by periodic molded vertical ribs.

Stiffening Techniques

Finally, we consider different stiffening techniques used in modern macro-scale engineering. Mechanical stiffening techniques have been extensively used in large-scale structures. Of particular interest are: 1) structures incorporating engineered stiffening structures, for example, rib-reinforced concrete decks and, 2) sandwich laminate materials such as those used for aircraft skin. Once the fundamental mechanisms governing the mechanical behavior of macro-scale stiffening techniques are understood we can begin to examine these techniques at the MEMS scale.

Rib-reinforced Structures

The most intuitive and straightforward method to stiffen a thin material is with corrugations or ribs. It is well known that the curvature, k, of a beam subjected to a moment M will bend according to the following relation,

$$\frac{\partial \theta}{\partial x} = k = -\frac{M}{EI}. \tag{1}$$

In this equation E is the modulus of elasticity, I is the moment of inertia of the cross-sectional area with respect to the neutral axis and θ is the slope of the centerline of the beam. As a simple example, we consider a beam with a rectangular cross-section of height h and width b. Then the moment of inertia for this cross-section with respect to the neutral axis is,

$$I = \frac{bh^3}{12}. \tag{2}$$

Substituting Equation 2 into Equation 1 we see that the curvature k of the beam decreases proportional to the cube of the height of the beam. Thus, for a beam with a rectangular cross section and a fixed width, increasing the film thickness by a factor of x decreases the curvature by $1/x^3$.

Now we consider composite T- and channel-shaped beams. For a composite cross-section such as those shown in Figure 7, the moment of inertia is,

$$I_{xx} = \sum \left(I_{xx_n} + A_n d_n^2 \right). \tag{3}$$

In this equation I_{xxn} is the moment of inertia of the nth piece, A_n is the area of the nth piece and d_n is the perpendicular distance between the centroid of the nth piece and the centroid of the entire composite cross-section.

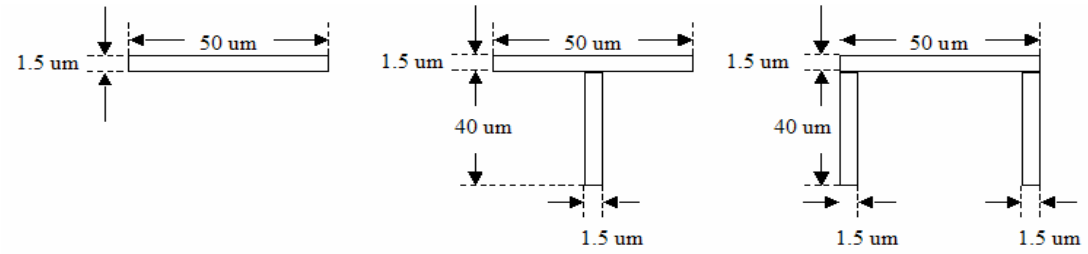


Figure 9 This figure shows flat, T- and channel-shaped cross sections used to demonstrate how cross-section influences bending rigidity.

Figure 9 shows dimensions for three beams fabricated on the first generation wafers. A detailed analysis of these beams can be found in Lutzenberger and Dickensheets 2002 [24]. Here we briefly consider these beams as an example to illustrate the increased film stiffness achieved with the proposed microfabrication technique. The composite moment of inertia is calculated for the cross-sections shown in Figure 9 to demonstrate the increased bending stiffnesses. Table 1 shows the area and moments of inertia for the flat, T-beam and C-beam. Clearly, both the T-beam and C-beam are much stiffer than the flat beam.

Table 1 Cross-section area and moments of inertia for different types of beams.

Cross-Section	Area, um^2	I_{xx}, um^4
Flat	75	14
T	135	22366
C	195	35886

As a final MEMS specific validation, two thin films with equivalent cross-sectional moments of inertia but different cross-section configurations are compared. One film is stiffened with vertical ribs resulting in a cross-section resembling a c-shaped beam, while the other film is a solid material with a rectangular cross-section. The moment of inertia of the rib-reinforced film is determined by Equation 3 while the moment of inertia of the solid film is given by Equation 2.

$$I(a,h,t)_{square} = \frac{t}{12(a+2h)}\left(4h^4 + 8ah^3 + 12ath^2 + 8aht^2 + a^2t^2\right) \tag{4}$$

In the above equation a is the distance between the ribs, t is the thickness of the film and h is the height of the fin. Combining Equations 4 and 5 and solving for the equivalent solid film thickness yields an equation for the equivalent solid film thickness in terms of fin depth, cells size and film thickness:

$$t_{equivalent\,solid} = \sqrt[3]{\frac{12I(a,h,t)_{square}}{a}} \tag{5}$$

Consider now a film stiffened with vertical ribs. The top-sheet thickness of the film, t, is 1.5 um and the fin thickness is 3.0 um. The fin depth, h, ranges between 0 and 50 um and the distance between the stiffening fins, a, ranges between 5 and 50 um. The following figures show the theoretical un-stiffened film thickness of a solid film required to match the moment of inertia of an equivalent stiffened film. It is clear from Figures 10 and 9 that the bending rigidity of the stiffened film quickly exceeds the practical limit for a solid material. In order to better explain the plots below consider an example case of for a solid film thickness of 5 um. According to Figure 10 a solid film with a thickness of 5

um has the same bending rigidity as a 1.5 um thick film stiffened with vertical fins just over 3 um deep with a fin spacing of 5 um.

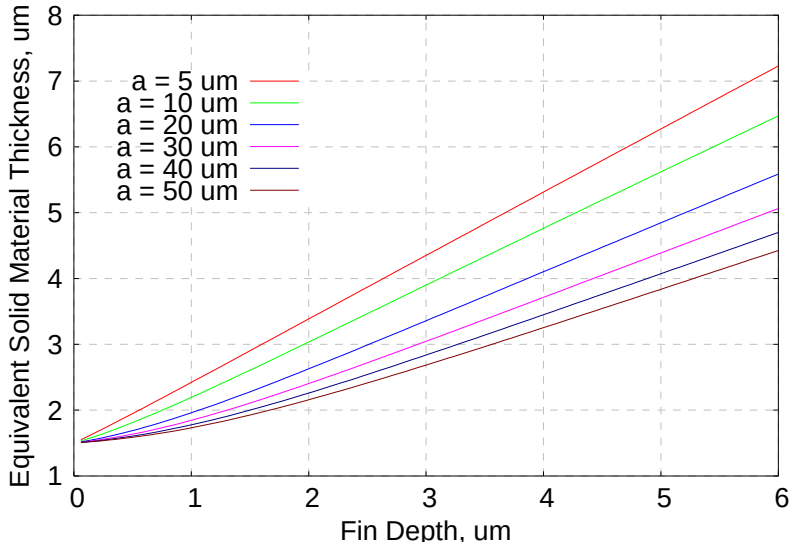


Figure 10 This figure shows the equivalent solid film thickness required to match the stiffness of a stiffened film for a variety of cell sizes with a fin height ranging between 0 and 6 um.

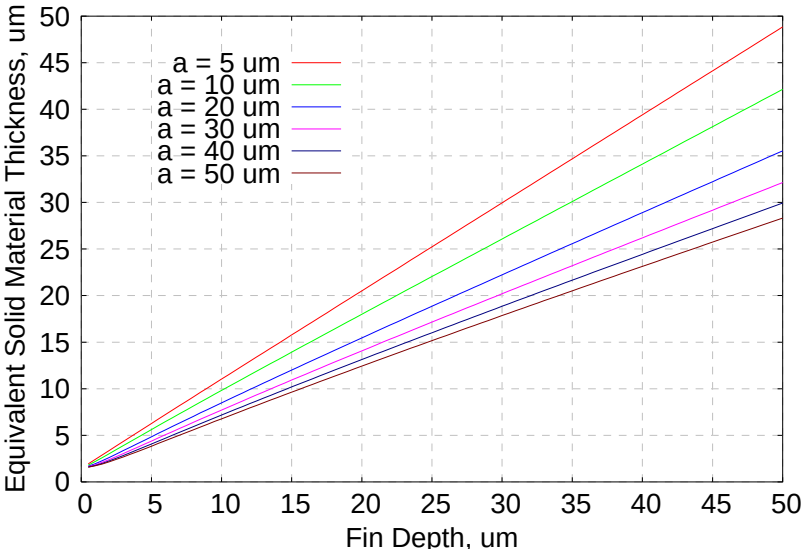


Figure 11 This figure shows the equivalent solid film thickness required to match the stiffness of a stiffened film for a variety of cell sizes with a fin height ranging between 0 and 50 um.

Silicon nitride fins have been etched and backfilled as deep as 50 um with the technique proposed in this research. According to Equation 4 a square cell with 50 um fins separated by 5 um has a moment of inertia of 48,500 um^4. This value cannot be practically achieved by depositing the equivalent amount of solid material. In fact, based on a deposition rate of 35 Å per minute approximately 226 hours or close to 10 days in a deposition furnace are required to obtain the equivalent 49 um of LPCVD silicon nitride needed to match the moment of inertia produced by adding 3.0 um wide vertical fins 50 um deep spaced 5 um apart.

Sandwich Materials with Cellular Cores

Extensive research on composite materials has been conducted by the aerospace industry since the early 1960's [19]. Of particular interest are sandwich laminate materials with periodic core materials. These materials offer a high strength-to-weight ratio making them efficient structures for various engineering applications.

Hexagonal and square cell cores are the two most commonly used cell geometries in lightweight sandwich materials. The role of the core in a sandwich laminate is twofold. First, the core material maintains a constant separation distance between the two face skins. Secondly, the core material contributes to the in-plane stiffness of the sandwich laminate material [9]. It has been shown by Becker and others that the effective core stiffness is not a linear function of thickness. This expected result significantly increases the complexity of closed-form solutions of the effective stiffness of sandwich laminate materials.

The effective moduli of honeycombs have been extensively studied both analytically and experimentally since the late 1950's [19]. Considerable discrepancies exist among early analytic solutions as well as between early analytic solutions and experimental results [30] and [31].

More recently, it has been shown that equivalent constitutive equations for hexagonal and square cell core materials can be obtained using unit force and unit displacement methods coupled with averaging techniques [32]. A more accurate approach relies on the theory of homogenization of heterogeneous periodic media. This theory was first presented by Bensoussan et. al. [4] and applied to hexagonal honeycomb core materials by Shi and Tong. Shi and Tong presented closed-form homogenization equations for honeycomb sandwich plates using the theory of homogenization of heterogeneous periodic media. Their solution has been shown to handle cases when the core thickness is much larger than the cell dimension as well as cases when the core thickness and the cell dimension are of the same order [30].

Shi and Tong have developed equations for the shear and tensile moduli for honeycomb core materials. These equations do not account for the added stiffness and warping constraints gained with the addition of face panels thus eliminating the dependency in the constitutive equations on the overall height of the core material. These equations are useful to obtain a reasonable lower bound for the equivalent moduli of mechanically stiffened silicon nitride films. For a regular hexagonal cell the effective moduli are given by:

$$E_{xx} = E_{yy} = \frac{tE}{2a\sqrt{3}} \tag{6}$$

$$G_{xy} = \frac{5E}{4\sqrt{3}}\left(\frac{t}{a}\right)^3 \tag{7}$$

In the above equation E is Young's modulus for the isotropic material, t is the thickness of the cell wall, and a is the length of each wall in the hexagonal cell.

Ribbed Shells

The thin film material presented in this research is essentially a rib-reinforced shell. Parton and Kudryavtsev [28] presented an analytic solution for the effective moduli of orthogonal rib-reinforced shells. Their theories reportedly agree well with classic structural theories presented in Russian literature in the 1970's and 1980's by Korolev [2].

Finite Element Approach

While the above-mentioned work represents a large portion of closed-form analysis of stiffened plates and honeycomb materials, they are not directly applicable to the film presented in this work. Due to the asymmetry in the cross section of the film presented in this research the above equation, do not yield accurate results for the sizes and types of cells tested in this research. Fortunately, a growing body of work exists on numerical computation of effective elastic moduli for heterogeneous materials [5]. Berggren et. al. (2001), note that effective material properties of non-homogeneous media are "quite natural from a physical point of view;" an observation that is often masked by complexity in modern mathematical literature on effective material properties of non-

homogeneous media. Displacement methods remain the method of choice when using numerical analysis to determine effective elastic moduli of non-homogeneous media. This is an intuitive and effective approach when using the finite element method for numerical computations.

The stiffened thin film presented in this research is an example of a heterogeneous material with periodicity. Employing the techniques proposed by Berggen et. al. and others, finite element models can be used to determine the effective flexural rigidity of this material. Various cell geometries can be simulated using finite element models making this approach an attractive method to rapidly determine effective material properties of periodically stiffened thin films. In this research, the use of finite element models to determine the effective rigidity of thin films periodically stiffened with square and hexagonal cells is demonstrated. The resulting material properties will be used to simplify finite element models of experimental MEMS fabricated with stiffened thin films. The experimental devices will be used to show that this technique can accurately simulate MEMS fabricated with the proposed stiffening technique.

Mechanical Stiffening Summary

Although there are several mathematical theories to determine effective elastic moduli of rib-reinforced and sandwich materials, there are obvious discrepancies and inconsistencies among them. Additionally, equations for cell geometries other than square or hexagonal honeycombs are tedious to derive. While the theories presented in this chapter are appropriate for validation purposes, they are simply not a practical design tool to optimize MEMS fabricated from rib-reinforced thin films with periodic cells. On

the other hand, numerical computation of elastic moduli can be a rapid and accurate method to determine the elastic moduli of the proposed thin film. Furthermore, parametric models with varying film thickness, rib height, and cell size can be rapidly build and analyzed allowing engineers to determine a wide range of effective elastic moduli. Curves can be constructed from the resulting data yielding equations for the elastic moduli as a function of film thickness, rib height and cell size. This method is presented to the MEMS community as a tool to simplify the design and optimization of MEMS fabricated with periodically stiffened thin films.

CHAPTER 3

FABRICATION

Chapter Overview

This chapter outlines the steps to produce micro mirrors and test structures fabricated with a mechanically stiffened silicon nitride film. Silicon nitride etch stops used by Himmer inspired the mechanical stiffeners [13]. The original process flow was proposed by Dickensheets, Himmer, Lutzenberger, Friholm and Kaiser [23]. It was implemented in 2001 to fabricate biaxial mirrors with optically flat surfaces measuring 400 um in diameter [24]. Special thanks go to Dr. Eric Peroziello for his help in developing and implementing the fabrication process.

Fabrication facilities

Devices were fabricated at the Stanford Nanofabrication Facility (SNF) through participation in the National Science Foundation's NNUN (National Nanofabrication Users Network) program. The Stanford facility, the Center for Integrated Systems, was selected because of the availability of LPCVD (low pressure chemical vapor deposition) equipment for growing silicon nitride thin films.

Process Flow

The mechanically stiffened silicon nitride film was fabricated with four photolithography steps, four material depositions, and five etch steps. The simple

processes and minimal lithography steps make this an attractive technique for fabricating various MEMS devices.

n-Type silicon wafers with a (100) crystal orientation were used to achieve a large air gap under devices by anisotropic etching the silicon in a 10% solution of tetramethyl ammonium hydroxide (TMAH) at 100°C. The backs of the silicon wafers were doped to enhance the conductivity of the silicon substrate. The back was also blanket-coated with chrome and gold. The original process flow for the first generation of devices included an additional thermal oxide wet etch and an additional nitride deposition. The thermal oxide etch was performed on first generation devices to produce an etch stop during the release process. However, the anisotropic silicon etch in TMAH and preferential nature of the oxide etch resulted in minimal undercutting of the silicon at the silicon-silicon nitride interface. Therefore, the oxide etch was omitted in the second-generation devices. Additionally, the second nitride layer was included in the first generation devices to achieve thin flexures and thus decrease actuation voltages. This was not a requirement for the second generation of devices. The second-generation process flow is shown in Figure 12 and described in detail below.

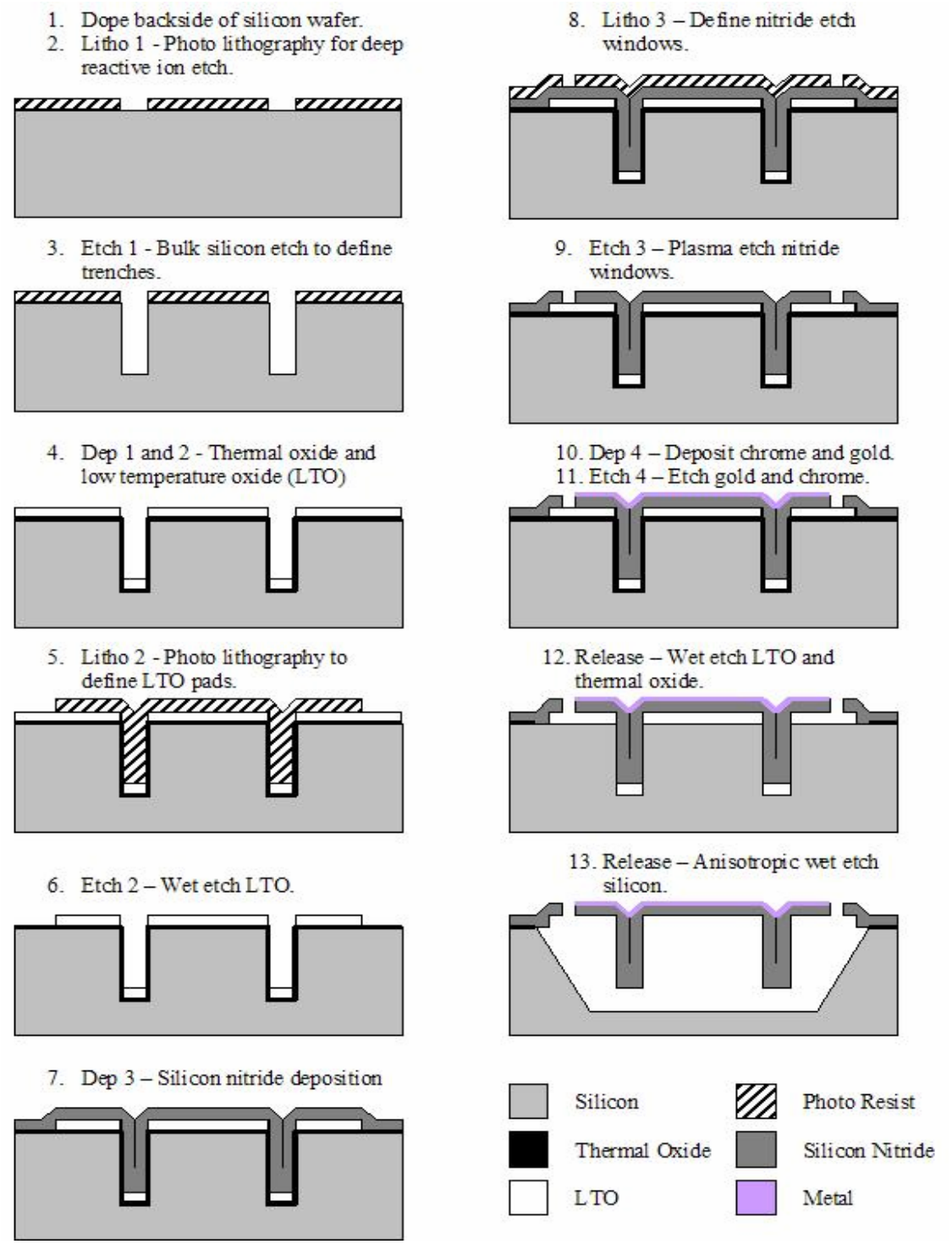


Figure 12 This figure details the fabrication process used to create a stiffened film of LPCVD silicon-nitride.

The fabrication process began by first cleaning the wafers in a 90°C mixture of 9:1 sulfuric acid and hydrogen peroxide, commonly referred to as piranha. A second thorough clean was performed to prepare the wafers for wet oxidation. The first oxidation protected the front sides of the wafers from the subsequent doping step. Approximately 1.0 um of thermal oxide was grown on the wafers at 1000°C. The front sides of the wafers were coated with 1.65 um of photo resist. The oxide was then striped from the backs of the wafers in a hydrofluoric bath leaving a protective oxide layer on the front. The photo resist was striped from the wafers and the wafers were cleaned for n-type doping in a phosphorous-rich gas.

The wafers were doped in a phosphorous-rich gas to increase the electron concentration on the backs of the n-type wafers. This was done to achieve adequate grounding of the substrate. The wafers were doped at 1000°C for three and one half hours giving a characteristic doping depth of approximately 0.25 um. This doping depth ensured that the doping volume was not completely removed during the subsequent silicon nitride plasma etch. The protective oxide layer was then striped from the front sides of the wafers preparing them for the trench etch.

A 1.65 um layer of photo resist was used for the first photolithography step. This lithography step defined the trenches in the bulk silicon, which were later backfilled with silicon nitride. A deep reactive ion etch was used to remove silicon from the unmasked areas on the silicon wafer. The reactive ion etch produced trenches in the silicon with nearly vertical sidewalls. A fine passivation/etch cycle minimized the scallop size in the trench sidewalls. The SEM in Figure 13 shows the back of a biaxial mirror and a zoomed

image of the stiffening fins clearly showing the scalloped sidewalls resulting from the deep reactive ion etch. The trenches were approximately 2.4 um wide and varied in depth from 25 um to 35 um.

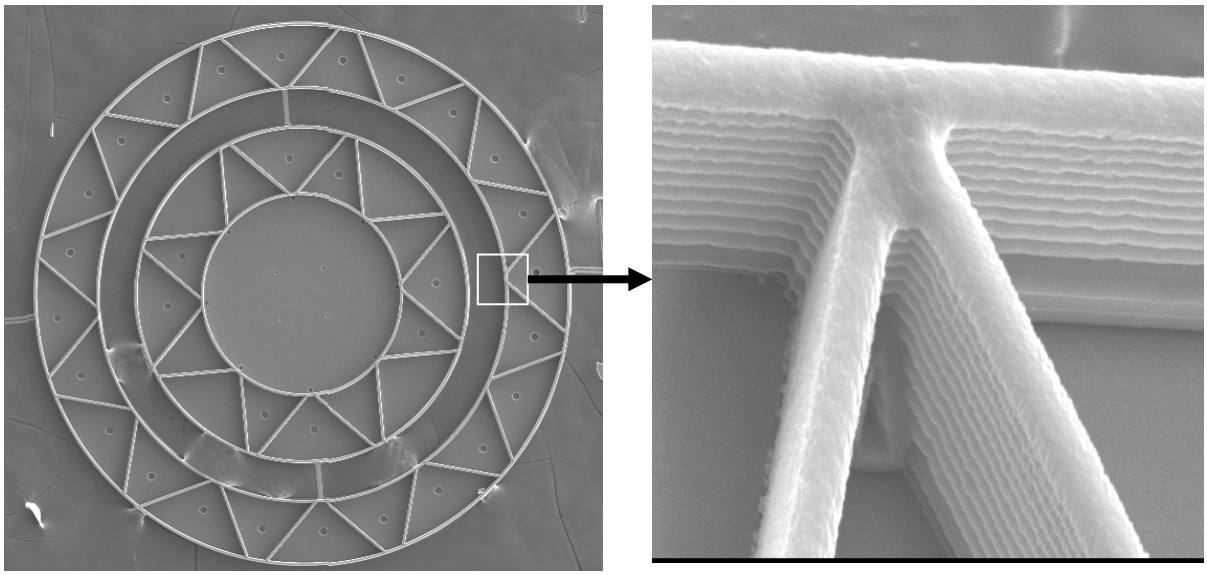


Figure 13 These SEMs show a detailed view of the stiffened silicon nitride film. The figure on the left shows the back of a biaxial mirror stiffened with the film. The SEM on the right shows a close up of the stiffening ribs.

The photo resist was removed from the etched silicon substrate. A high temperature wet oxidation process was used to grow 5000 A of thermal oxide on the silicon. The thermal oxide coated the wafer's surface and the trench sidewalls and trench bottoms. This was followed by a second 5000 A PSG oxidation growth at 400°C. The PSG etch did not cover the trench sidewalls.

A wet oxide etch was used to define the PSG pads under the nitride devices. A 6:1 BOE solution was used to etch the oxide. The etch rate for 6:1 BOE was approximately 900 A/min. The wafers were then coated with two 3.65 um thick layers of photo resist to

ensure uniform coverage over the filled trench topography. Originally, 7 um resist was used to define the PSG pads, however, the high viscosity of the resist did not adequately fill the trenches resulting in air pockets in the trenches. When spinning the resist on, the air pockets were forced out of the trenches emerging as small (~ 1 mm) air bubbles. The bubbles caused significant streaking of the photo resist on the wafer. Therefore, the 7 um resist was replaced with two applications of lower viscosity 3.5 um resist.

A diffusion clean was performed to prepare the wafers for LPCVD nitride. Approximately 1.6 um of nitride was deposited onto the wafer. The nitride deposition produced a conformal layer across the entire wafer completely filling the etched trenches to form the vertical stiffeners. The conformal nature of LPCVD silicon nitride is clearly shown in Figure 14 and Figure 15. Figure 14 shows the cross section of a cantilever beam with vertical stiffening fins and oxide removed. Figure 15 shows a close-up of a typical filled trench. The LPCVD silicon nitride was deposited at a low temperature to minimize the post-release thermal strain in the film. Guckle ring measurements indicated the post-release thermal strain in the silicon nitride was approximately 150 MPa, in tension [11].

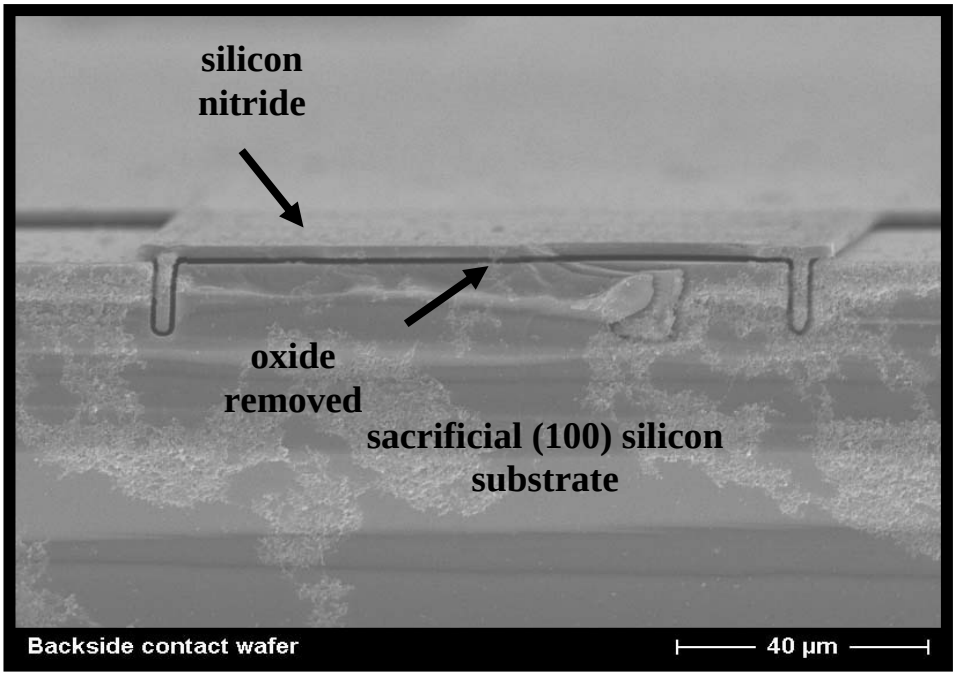


Figure 14 The SEM in this figure shows the cross-section of a stiffened silicon nitride cantilever beam. The oxide has been removed to increase the contrast between the silicon nitride film and the sacrificial silicon substrate.

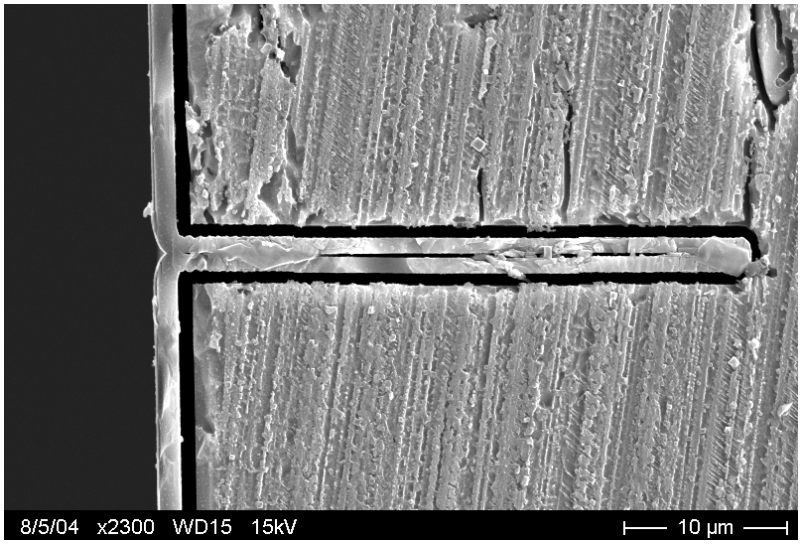


Figure 15 This SEM shows a close-up of a silicon nitride stiffening rib.

The wafers were then coated with a 1.6 um thick layer of photo resist to ensure uniform coverage over the filled trench topography. This lithography step was used to defined the devices. A reactive ion etch was then performed to etch the exposed silicon nitride.

Finally, the wafers were coated with chrome and gold. 50 A of chrome was sputtered onto the wafers followed by 1000 A of gold. A final photolithography step was used to define the metal patterns on the devices. An aqueous etch was used to pattern the chrome and gold. The chrome was deposited to serve as an adhesive layer between the silicon nitride and the gold. Sputtered chrome typically has a high post-release thermal strain with a significantly different coefficient of thermal expansions than silicon nitride. Therefore, it was important to minimize the thickness of the chrome as much as possible while maintaining adequate adhesion between the silicon nitride and the gold. Figure 16 shows an atomic force microscope (AFM) image of the top side of a gold coated honeycomb cell. Topside trench topography results when the silicon nitride has filled the trench and closes of the fin. The topside trench depth ranged from 140 nm to 270 nm deep. The trench topography shown in Figure 12 is 227 nm deep.

Mirror Release

Release begins with removal of the PSG and thermal oxide sacrificial layers. This etch step was accomplished with a 6:1 buffered oxide etch (BOE). An anisotropic etch in TMAH was used to remove the underlying exposed silicon. The release steps are shown in steps 12 and 13 of Figure 12.

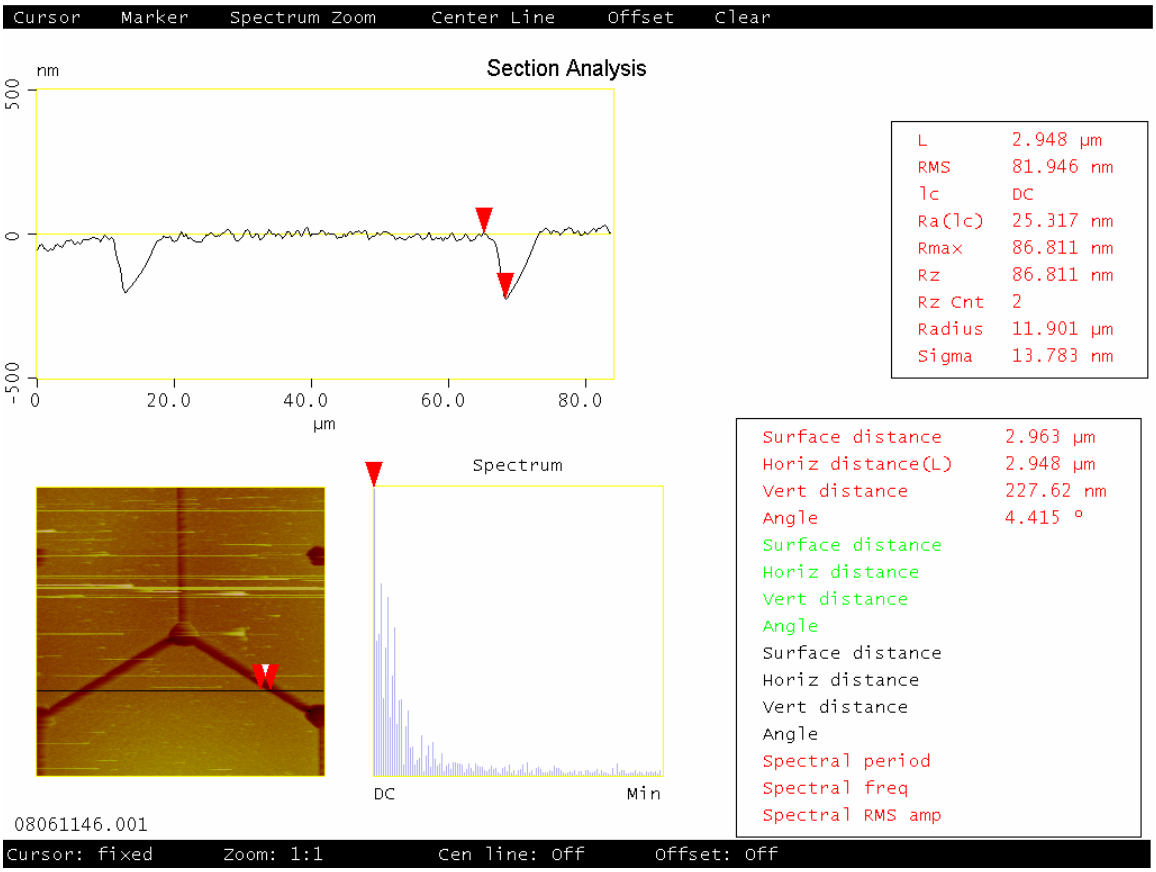


Figure 16 AFM output showing the surface characteristics of the stiffened silicon nitride film.

Sacrificial Layer Etch

The etch rate of the PSG and thermal oxide is governed by two parameters, the concentration of HF used and the diffusion rates of the products and reactants of the etch process. To remove the PSG and thermal oxide a 6:1 BOE solution was used (6 parts ammonium fluoride 1 part 49% HF in water). This concentration was found to have a sufficient etch rate for the geometries of the mirrors released in this research. The etch rate of the 8% PSG oxide is given as 6000 Å/min for 6:1 BOE in literature for open surfaces. The etch rate for thermal oxide is given as 900 Å/min for 6:1 BOE. 6:1 BOE

has good oxide selectivity when compared with silicon nitride. Silicon nitride is reported to etch at less than 10 A/min in 6:1 BOE (Kovacs). Due to the geometric constraints of several of the device cavities the PSG and thermal oxide etch rates are much lower than those cited above. This is most likely due to a reduction in the diffusion rate of the etchant and etched products within the cavities [6]. Oxide etch times in excess of 2 hours were required to completely remove the oxide from hexagonal and square cells. The extended oxide etch times make 6:1 BOE a better solution than concentrated HF (49% in water) which etches nitride at approximately 50 A/min. Figure 17 shows residual oxide (circles around the vias) on the back of a lattice stiffened mirror. The residual oxide was easily removed with a second oxide etch once the silicon etch had exposed most of the cells' interiors.

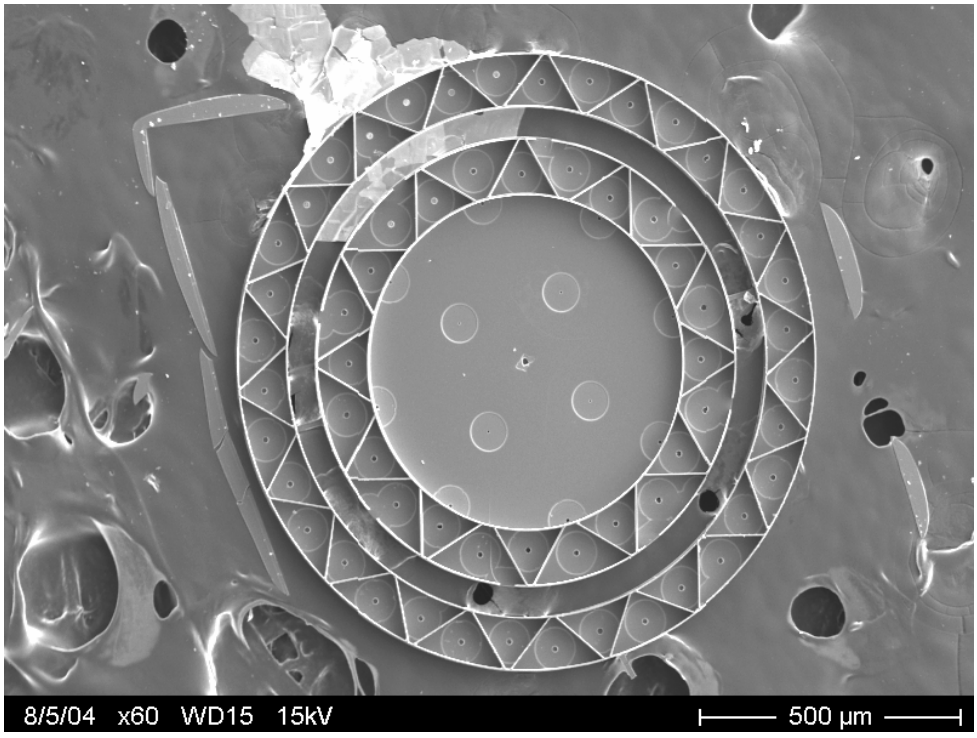


Figure 17 The circles surrounding the etch vias in this SEM clearly demonstrate the difficulty in detecting and removing residual oxide.

Long etch times for the sacrificial oxide layer, however, resulted in undercutting at the etch perimeter of devices leaving silicon nitride suspended over the silicon substrate. Figure 19 illustrates the oxide etch undercut. The previous fabrication process included a thermal oxide etch before nitride deposition to avoid undercutting. However, this pre-deposition oxide etch produced a region where the silicon and silicon nitride were in direct contact producing a potential short under the metal electrode traces. Figures 18 and 19 show a partially etched cross-section of a biaxial mirror. Note how the silicon etch front undercuts the silicon nitride frame.

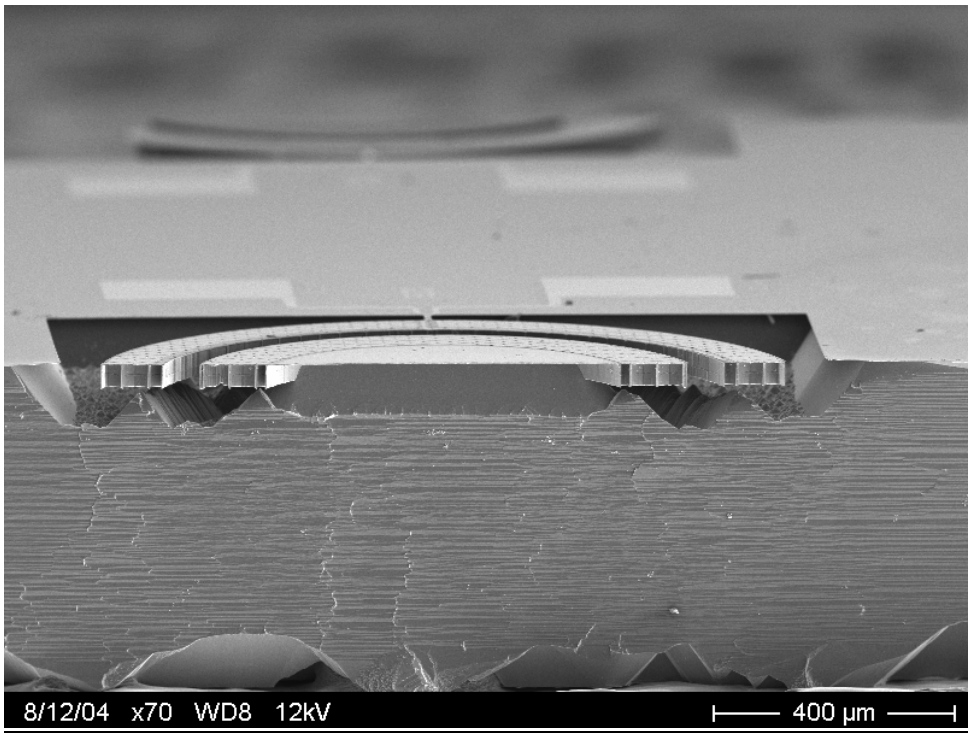


Figure 18 This SEM image shows the cross-section of a partially released biaxial scan mirror.

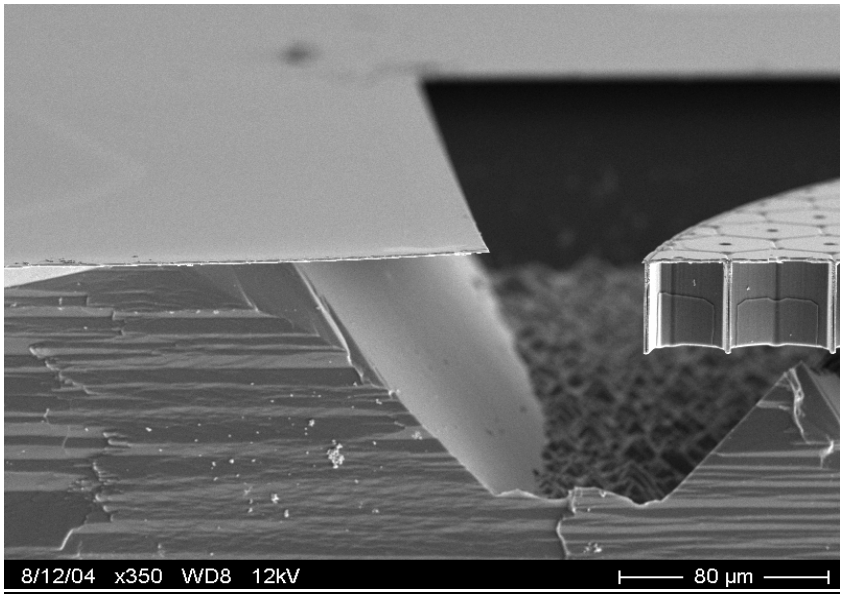


Figure 19 This SEM is a close-up of the same mirror shown in Figure 18. This figure shows how the silicon etch front undercuts the silicon nitride frame when an etch stop is omitted.

Numerical simulations of silicon-free and oxide-free mirrors predicted much less curvature due to post-release thermal strain than was observed in the mirrors after the first TMAH etch. Based on wafer bow measurements, Guckel ring measurements and cantilever tests, the post-release thermal strain in the silicon nitride was found to be insufficient to cause such curvature. Therefore, it was clear that a different mechanism was causing the excess curvature. An additional 35 min oxide etch indicated that the excess curvature was due to a stress differential between the silicon nitride and residual oxide. Curvature data take before and after the additional oxide etch demonstrates the potentially disastrous effects residual oxide can have on silicon nitride if not adequately removed. It was concluded that a stress differential between the silicon nitride and oxide

layers was responsible for producing excess curvature in the mirrors after the first silicon etch.

Once the oxide had been sufficiently cleared, the mirrors assumed their predicted shape. As expected, the mirrors with 25 um stiffening cells were flatter than mirrors with 50 um cells. Additionally, the square cells were flatter than the hexagonal cells. For all of these mirrors, the surface deformation after a complete etch remains below 1 um across the 1.5 mm diameter; and in the case of the 25 um square cells the surface curvature was not measurable with our current surface profilometer.

Figure 20 shows the effect of residual oxide on single axis mirrors. This plot shows surface profiles across 1500 um diameter single axis scan mirrors stiffened with 25 um square cells. The red curve shows the surface profile for a mirror with residual oxide inside the cells. The blue curve shows the surface profile across the same mirror with an additional oxide etch.

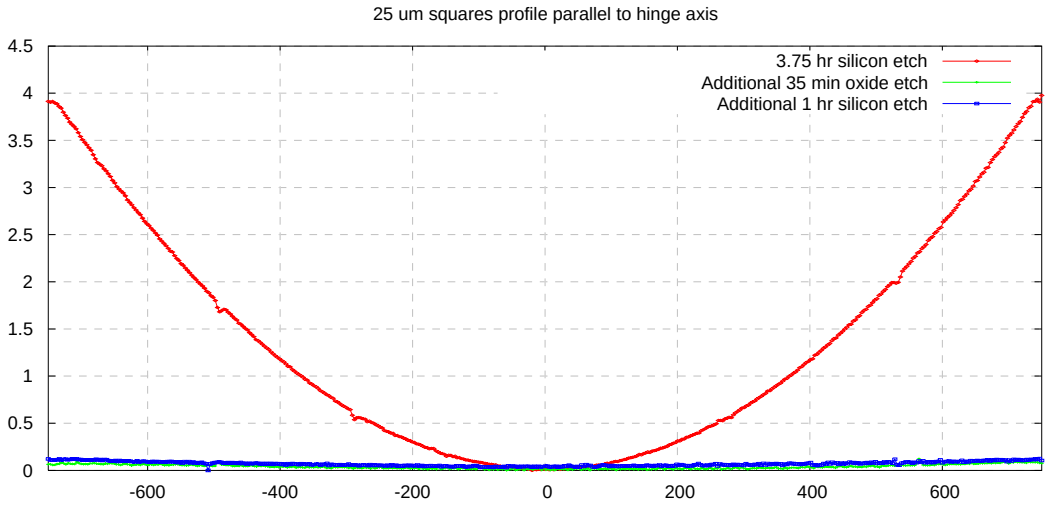


Figure 20 Both of the surface profiles shown were taken across the same 1500 um diameter fully stiffened mirror. The highly curved surface profile data was taken prior to an additional oxide etch intended to remove residual oxide from the back of the mirror.

Bulk Silicon Etch

Bulk etching of the silicon was accomplished with tetramethylammonium hydroxide (TMAH). TMAH is an anisotropic etchant of silicon, it attacks the (100) crystal planes of silicon with an etch rate up to 50 times that of the (111) crystal planes. A byproduct of the silicon etch is hydrogen gas. Formation of large H_2 bubbles beneath the devices during the TMAH etch can lead to failure. The release of hydrogen and subsequent build-up and release of hydrogen bubbles during the bulk silicon etch must be considered when designing devices for this fabrication method. Additionally, adhesion of hydrogen bubbles to the silicon is considered a cause of hillocks, which leads to a roughened surface. Surface roughness was not a concern for the devices tested therefore extra steps to reduce the size and adhesion of hydrogen bubbles were not taken. Figure 21 shows an extremely rough silicon surface under a partially cleared biaxial mirror. Himmer has experimented with various surfactants and TMAH concentrations to obtain smooth silicon surfaces for deformable membranes [13].

A TMAH concentration of 6% at 100°C was used to release the devices. This concentration and temperature corresponds to an etch rate ranging between of 100 um/hr to 120 um/hr. Higher TMAH concentration were also tested with no appreciable differences in survivability.

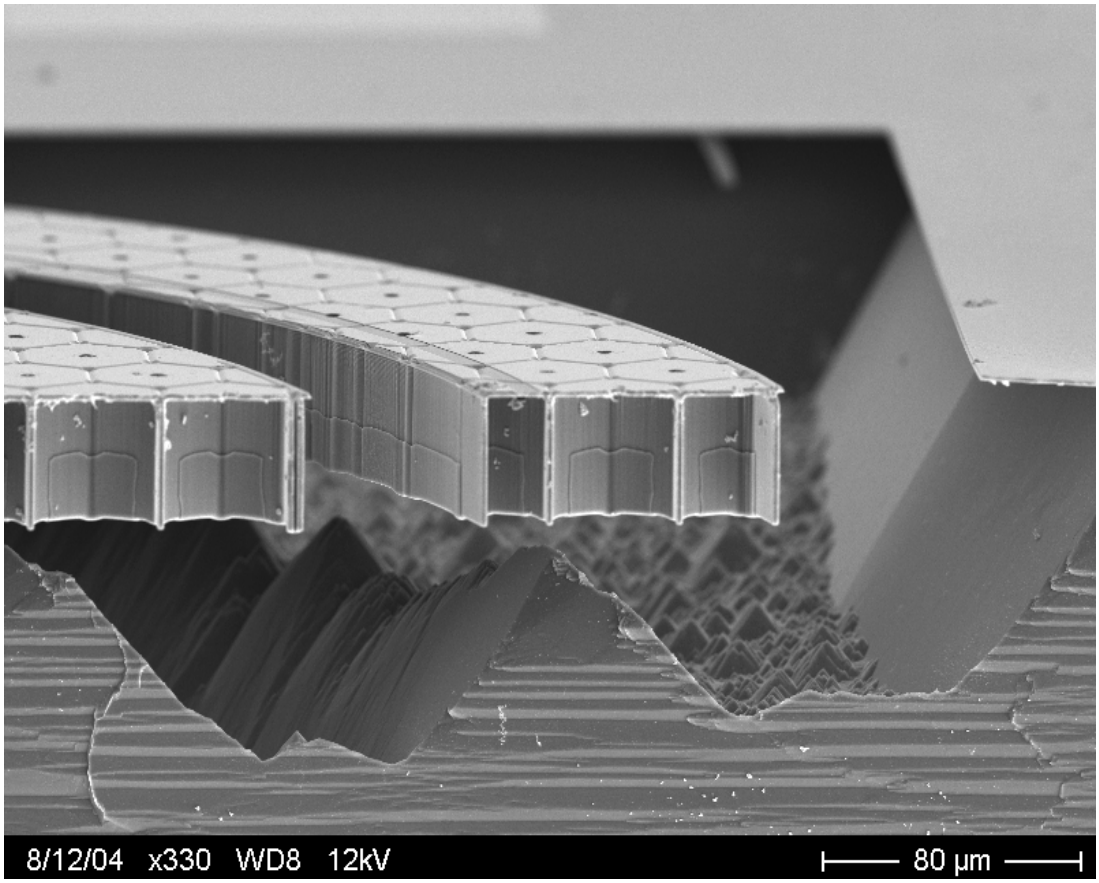


Figure 21 This SEM demonstrates the rough silicon bottom resulting from an aggressive silicon etch.

Fabrication Summary

The fabrication process presented in this chapter represents a novel technique to produce a structurally stiffened LPCVD silicon nitride film. A detailed fabrication procedure has been given to create a mechanically stiffened thin, 1.5 um, film of silicon nitride, with nearly arbitrary control over the depth and pattern of the vertical stiffening fins. The resulting material retains the excellent optical and electrical properties traditionally found in LPCVD silicon nitride films with the added benefit of increased

flexural rigidity and a high strength-to-weight ratio. The combination of bulk and surface micro-machining techniques results in a simple fabrication that requires only a few additional steps to produce the stiffening ribs. Of particular interest and worth consideration is the effect of residual oxide on film curvature, even in the presence of deep stiffening ribs. The removal of all residual oxide in such a film is vital if a flat, low-stress film is required.

CHAPTER 4

FIRST GENERATION BIAXIAL MICRO MIRROR

Background

This chapter describes prototype mirrors intended to serve as proof-of-concept devices supporting the development of a periodic stiffened film. The original goal driving the use of stiffened silicon nitride as a structural film was to produce light-weight, large area micro scan mirrors for optical telecommunication systems. Mirrors were fabricated in 2000 and 2001 during a preliminary fabrication run in which several mirrors with varying diameters and rib patterns were built. The most promising devices produced in this phase were biaxial gimbaled mirrors with a 400 um diameter optical surface. The mirrors were fabricated from a 1.5 um thick layer of silicon nitride stiffened with a latticed rib structure around the outer gimbaled ring and around the perimeter of the inner disk surface. A 1x2 optical switch was constructed with the mirrors to test their usefulness as switch elements in optical telecommunication systems. The curvature of the optical surface was also measured for a range of temperatures.

Motivation

As is common with most thin films used in modern microfabrication, unreleased silicon nitride can be highly stressed due to a combination of mismatched coefficients of thermal expansion between the substrate material and silicon nitride and elevated deposition temperatures. When cooled to room temperature and released from its

substrate, thermal strain in the film can cause large static curvatures to develop across the surface of a thin mirror fabricated from such a film. Coating the mirror surface with a reflective metal layer can contribute additional differential thermal strain. To resist the thermal strain induced surface curvature, ribs were molded to the backside of the silicon nitride micro mirrors. Since bending stiffness is proportional to the product of the elastic modulus and moment of inertia, the fins, which increase the cross-sectional moment of inertia, increase the in-plane bending stiffness of the mirrors [21], [22], [26] and [27]. When applied in a lattice structure around a mirror, the fins have been shown to reduce stress induced surface deviation. Furthermore, anisotropic etching of the (100) silicon substrate under the mirror produced large air gaps without the use of elevators or pop-up mechanisms commonly found in surface micromachined torsion mirrors that require a large range of motion.

Biaxial mirrors with optical surfaces up to 400 um were successfully fabricated from a 1.5 um thick layer of silicon nitride with mechanical stiffening flanges. A 1x2 optical switch was constructed with these mirrors, demonstrating their usefulness as switch elements in optical systems. These devices inspired a second-generation fabrication focused on further characterizing the mechanically stiffened silicon nitride film.

Fabrication and Release

The first generation process flow differed only slightly from the second-generation process flow as described in Chapter 3. Unlike the second-generation process flow, an additional oxide etch around the perimeter of the etch windows was performed

prior to silicon nitride deposition. This was intended to act as an etch stop by ensuring contact between the silicon nitride and sacrificial silicon substrate. Additionally, two silicon nitride layer were deposited to achieve thinned flexures. This was accomplished by first depositing a 1.0 um layer of silicon nitride. This layer was etched to define the mirror only. Then a second layer of 0.5 um silicon nitride was deposited over the first layer of silicon nitride. This layer was etched defining the mirror and flexures resulting in a mirror with a 1.5 um layer of silicon nitride with 0.5 um thick flexures.

The release process consisted of a sacrificial oxide etch and a bulk silicon etch. The underlying material (PSG and silicon) was exposed through etch vias and at the perimeter of the structure. The sacrificial PSG layer was etched in a hydrofluoric acid bath exposing the underlying silicon substrate. Tetra methyl ammonium hydroxide (TMAH) was used to etch the bulk silicon under and around the mirror. The anisotropic etching property of TMAH produces a nearly flat pit beneath the mirrors when using (100) silicon substrates.

Mechanical Characteristics

Figure 22 shows a molded silicon nitride mirror with an inner plate diameter of 600 um and an optical (rib free) surface diameter of 400 um. The diameter of the gimbaled ring is 1 mm. The flexure lengths for the inner and outer axes are 75 um and 100 um, respectively. The flexure widths for the inner and outer axes are 8 um and 10 um, respectively. The thickness of the flexures is 0.5 um and the distance from the mirror surface to the anisotropically etched substrate is 140 um. Wafers with fin depths ranging from 12 um to 28 um were fabricated. The mirrors are actuated via metal electrodes

patterned on top surface of the mirror. The substrate is grounded to act as a counter-electrode for actuation.

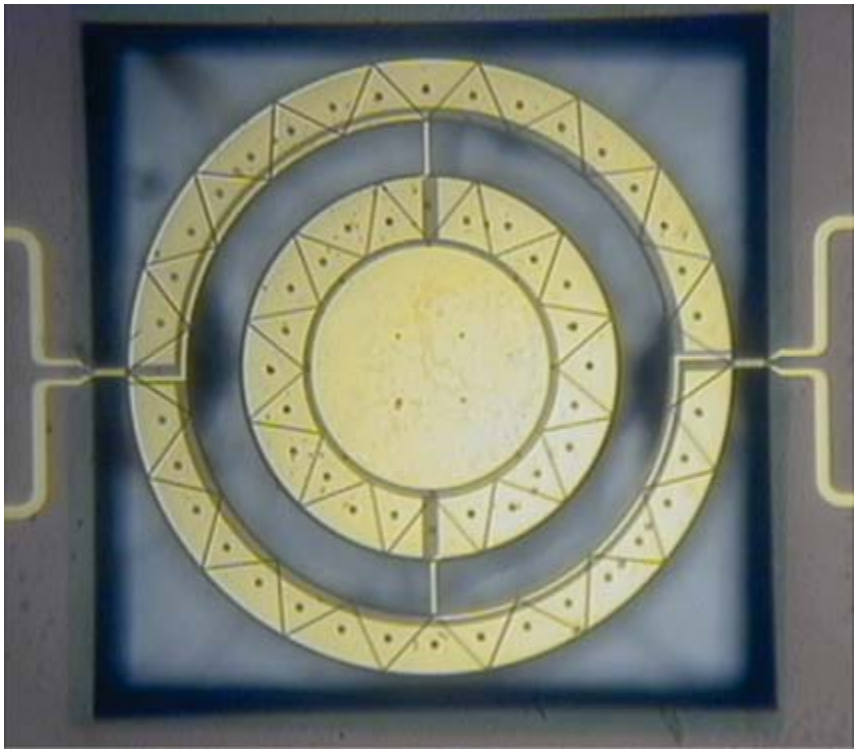


Figure 22 This image shows a rib reinforced biaxial scan mirror. The stiffeners are arranged in a lattice around the outer ring and the perimeter of the inner disk.

Tilt angle was measured for several actuation voltages using a two dimensional position sensitive detector (PSD) by reflecting visible light off the mirror and onto the PSD. Each axis of the mirror was driven with a high frequency (100 kHz) square AC waveform. A high frequency AC waveform was used to minimize charge accumulation in the nitride layer. The inner axis required 51 volts (square wave amplitude) to tilt the mirror 4.0°, while only 36 volts was required to tilt 4.0° on the outer axis.

Figure 23 shows step response data for the inner and outer axes of the mirror shown in Figure 22. The settling times for the inner (left and right) and outer (up and down) axes were approximately 40 ms and 25 ms, respectively. The resonant frequencies for the inner and outer axes were 400 Hz and 250 Hz.

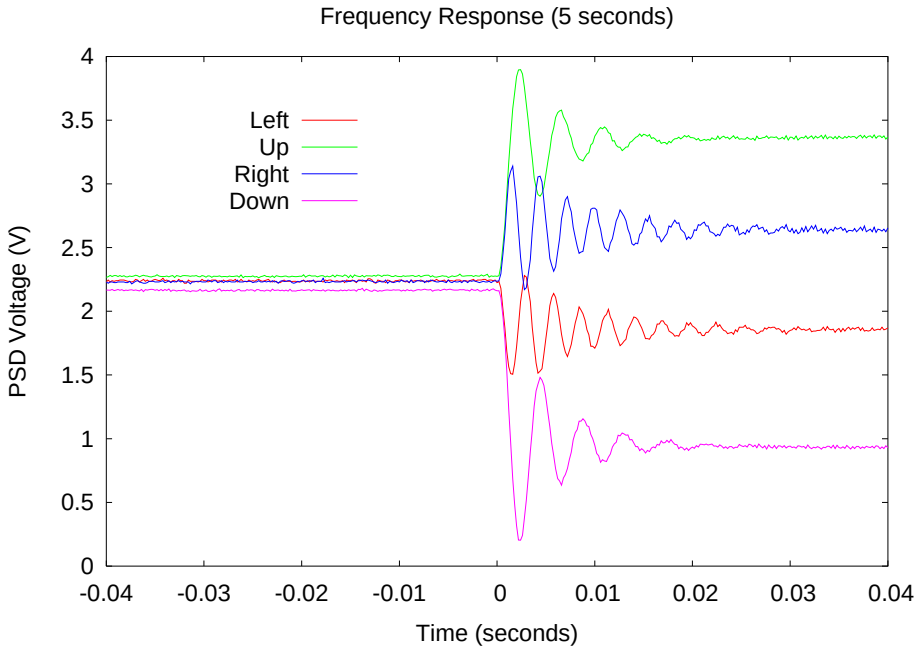


Figure 23 This plot shows the inner and outer step-response of the biaxial scan mirror shown in Figure 22.

Optical Characteristics

The scanning electron micrograph (SEM) in Figure 24 shows the latticed fins on the backside of a released mirror. The center (optical portion) of the mirror does not have latticed fins to avoid diffraction from the fin patterns. Figure 24 also shows an interferogram of a molded silicon nitride mirror using 660 nm illumination. The fringe lines in the interferogam correspond to less than 0.33 um deviation (peak to valley)

across the optical surface. Additionally, most of the aberration is confined to the extreme perimeter of the optical surface.

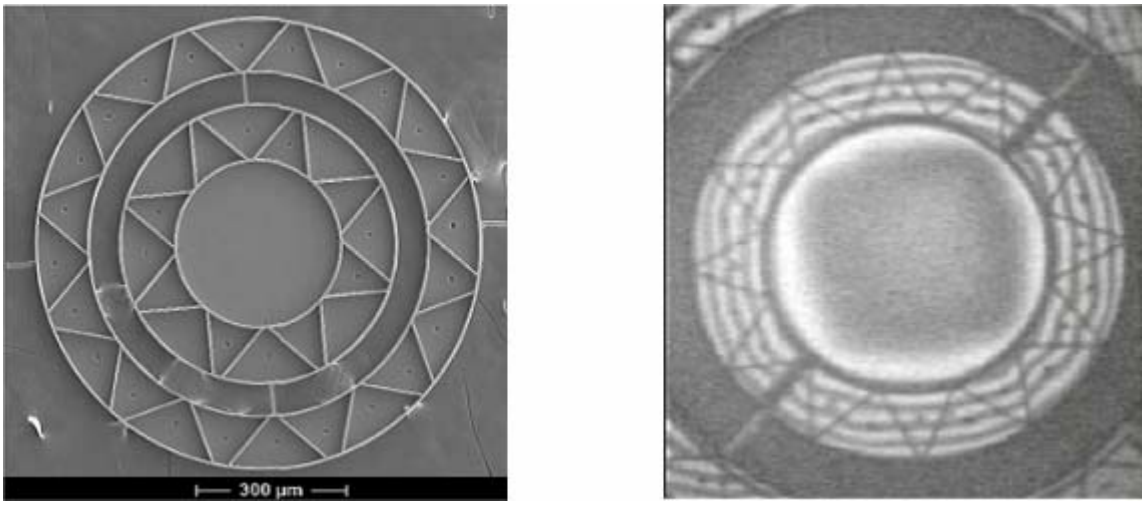


Figure 24 The image on the left is an SEM showing the backside of a laticed biaxial scan mirror. The image on the right is an interferogram imaged at 660 nm showing a diamond shaped optical surface.

The mirrors were used in the 1x2 optical switch depicted in Figure 25. Insertion loss as a function of mirror angle and incident power was measured with the switch. Light at 1550 nm wavelength was launched into the switch using single-mode fiber and a gradient index collimator. A lens with a 25 mm focal length was used to focus the beam on the mirror. The mirror was aligned to reflect the light back into a collimated single-mode fiber connected to an optical power meter with an infrared detector. The beam $1/e^2$ intensity diameter at the mirror was approximately 120 um. Launched power was measured with a patch cord from the power source to the power meter. Power loss measurements were made relative to launched power, and therefore included all components in the switch.

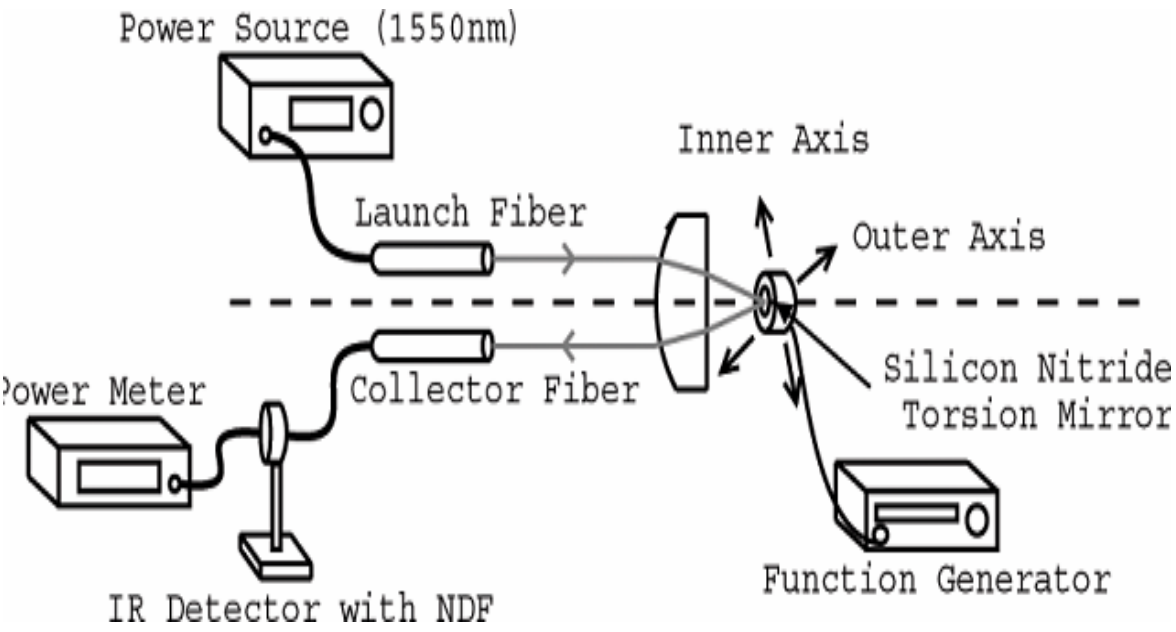


Figure 25 This figure shows a schematic of the experimental optical switch.

Figure 26 shows the power loss in decibels (dB) as a function of launched power at 1550 nm between 0.5 milliwatts and 4.0 milliwatts for four mirrors. As depicted in Figure 25 the insertion loss measurements include losses from the lens and coupling process. An unreleased mirror was measured to compare the power loss on a flat mirror to the power loss on a released mirror with stress induced surface curvature. The unreleased mirror shows approximately 1.2 dB power loss while the released mirrors show between 1.73 dB and 1.82 dB power loss.

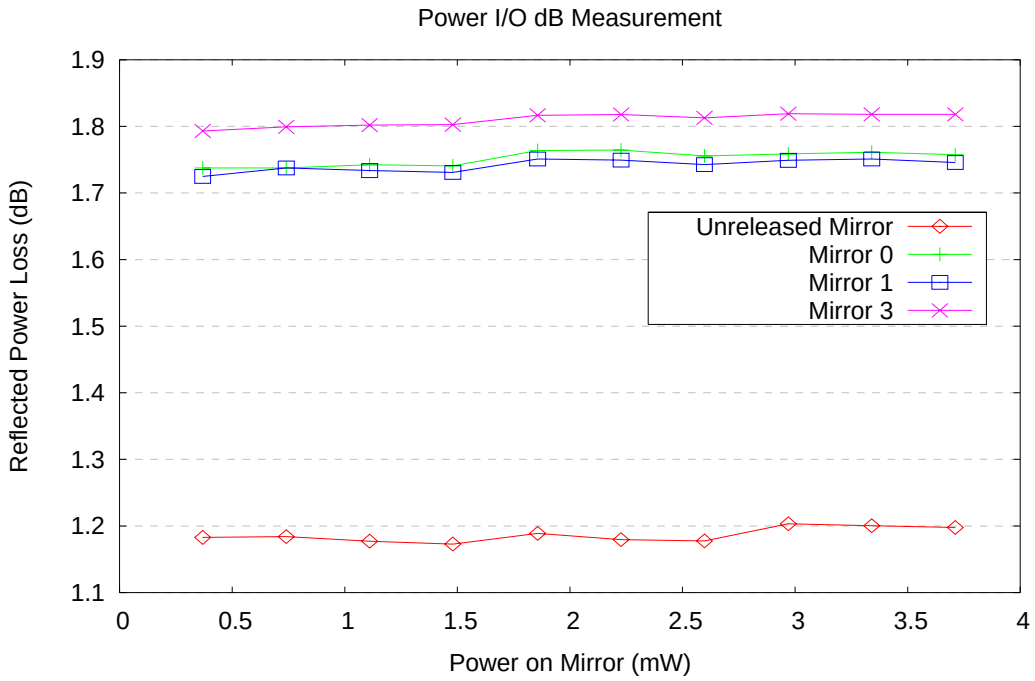


Figure 26 This plot shows the power loss measurements taken through the experimental switch for three released mirrors and one un-released reference mirror.

Power decoupling as a function of tilt angle is shown in Figure 27. Power decoupling in the switch was achieved down to 40 dB in all directions. Insertion loss was greater than 30 dB for mirror tilt in excess of 0.5° on either the inner or outer axes. Based on a +/- 4° range of motion for both axes and 30 dB isolation between output ports, a theoretical maximum number of addressable ports of 16x16 = 256 could be achieved with these mirrors.

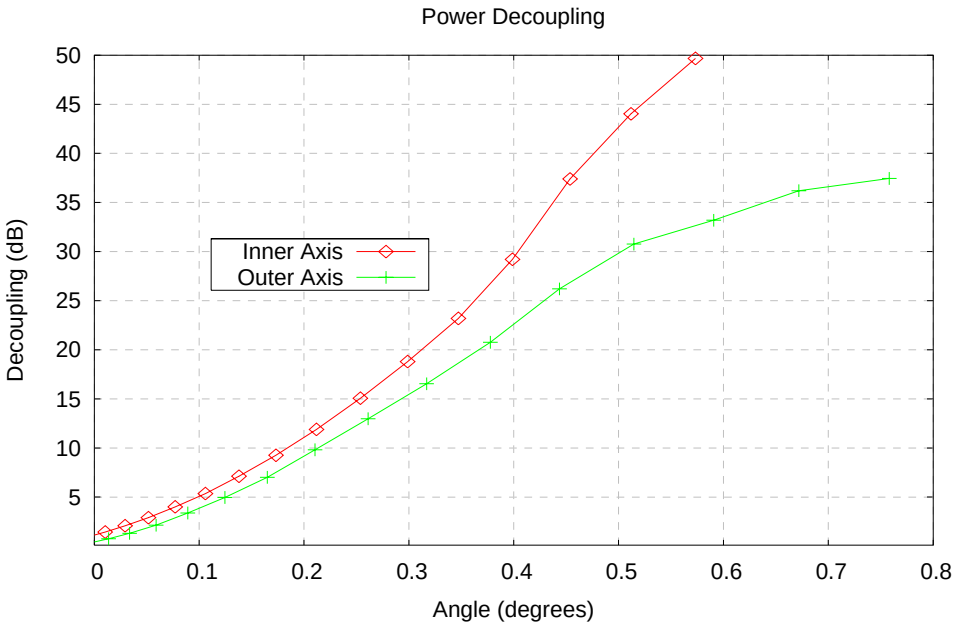


Figure 27 This figure shows power decoupling through the switch as the mirror is electrostatically tilted away from the the collector fiber.

Finally, surface profiles across the 400 um optical surfaces were measured for temperature ranging between 60°C and 120°C. Measurements were taken for mirrors with 28 um and 12 um deep fins to demonstrate the effect of rib depth on surface curvature due to thermal strain. Figures 28 and 29 show the surface profile across the 400 um optical surface for the mirrors. The profiles were taken along the inner and outer hinge axes of each mirror (labeled IHA and OHA, respectively). Note the astigmatism in both of the mirrors. According to the measured surface profile, the curvatures of the optical surfaces appear to be relatively insensitive to thermal variation within the tested temperature range. Figures 28 and 29 also illustrate the effects of deeper fins on surface flatness. There is significant decrease in surface deformation along the inner and outer hinge axes in the 28 um deep fin mirror when compared with the 12 um deep fin mirror.

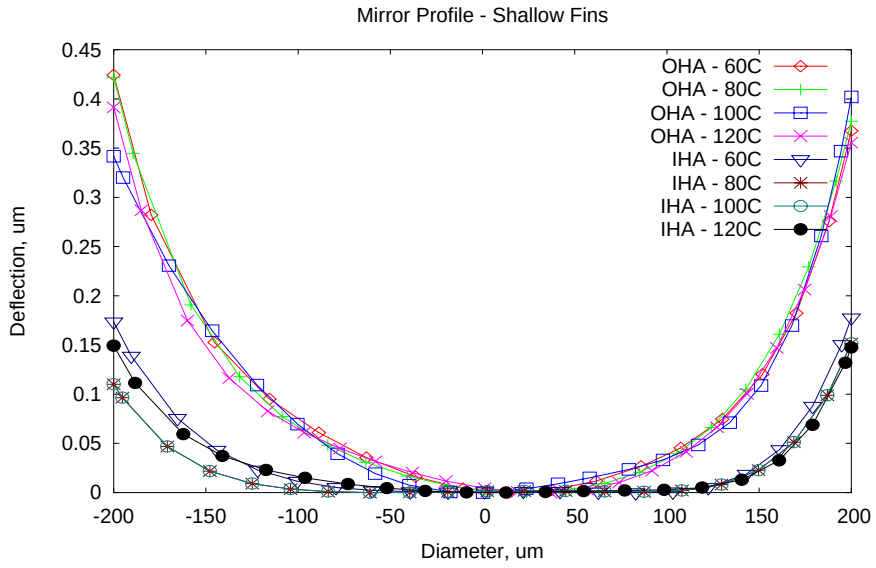


Figure 28 This plot shows the profile of the optical surface of a mirror with shallow fins taken along the outer hinge axis (OHA) and the inner hinge axis (IHA) for a range of temperatures.

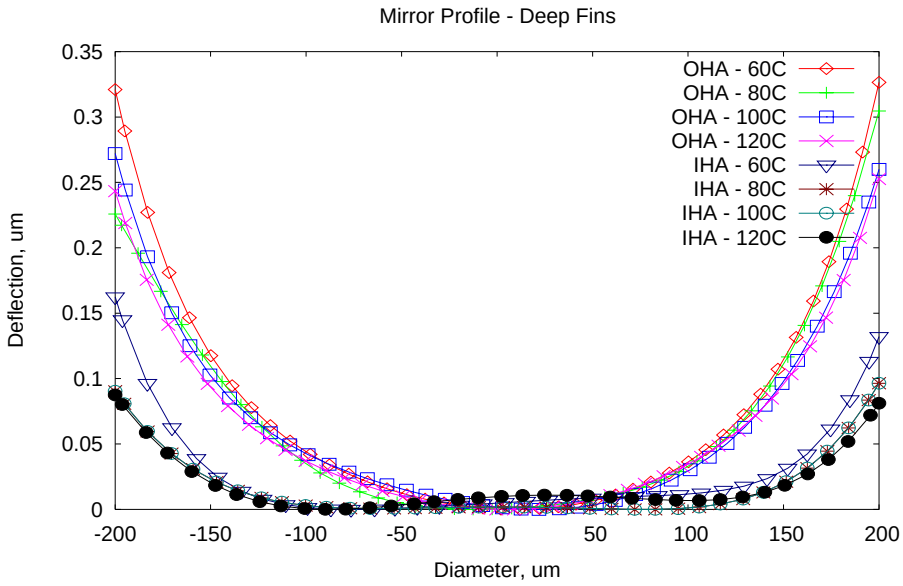


Figure 29 This plot shows the profile of the optical surface of a mirror with deep fins taken along the outer hinge axis (OHA) and the inner hinge axis (IHA) for a range of temperatures.

Conclusion

The mirrors performed well in the constructed switch. Power loss measurements revealed less than 2 dB insertion loss with 0.6 dB attributed to surface deformation. The optical quality and decoupling capability of the mirrors were well within acceptable operating tolerances for a variety of telecommunication applications. The molded fin structure adequately stiffened the mirror allowing large optical surfaces to be constructed from a thin layer of low-stress silicon nitride. Mirrors as large as 400 um in diameter were stiffened to reduce stress-induced surface deformation to less than 0.33 um. Angular rotations of +/- 4° rotation about two axes were achieved for voltages less than 55 volts. The excellent mechanical and optical characteristics coupled with a simple batch fabrication process make these mirrors an attractive alternative to traditional polysilicon micro mirrors. The excellent performance characteristics of these mirrors suggests that stiffening thin films with vertical fins can be a useful technique to increase the stiffness of an otherwise flexible film while maintaining a simple process flow.

CHAPTER 5

VALIDATION OF DETAILED NUMERICAL MODELS

Although periodic stiffeners significantly increase the bending stiffness of LPCVD silicon nitride films, simulating MEMS fabricated with such a film is not a trivial task. A naïve finite element simulation would employ a model in which each individual cell has been explicitly modeled. This approach has significant computational limitations. While simulations of simple devices are possible with such a naïve model, as the overall dimension of the MEMS to be simulated becomes large relative to the cell dimensions, the finite element model becomes computationally intensive. As an alternative approach, the periodically stiffened film can be treated as a two layer composite material. Simple fully detailed numerical models of films stiffened with a variety of cells shapes and sizes can be used to determine a simplified constitutive model for the periodic cell layer. This constitutive model can then be used to simplify numerical analyses of MEMS fabricated with a periodically stiffened film. However, the fully detailed numerical models must first be validated before any simplifications can be made.

In this chapter laboratory experiments and numerical analyses of mechanically vibrated micromachined cantilever beams are presented. These experiments are used to validate fully detailed numerical models of simple cantilever beams fabricated from stiffened silicon nitride. Ultimately, the fully detailed models are used to determine a simplified constitutive model for stiffened films with various cell types and sizes. The simplified constitutive model will be applied to a two-layer composite shell finite element

formulation. The application of simplified constitutive models to a two-layer finite shell element is covered in Chapter 6.

The first part of this chapter describes the geometry of the experimental micromachined cantilever beams. The experiment setup used to obtain resonant frequencies for the micro-cantilevers is also covered. The second part of this chapter compares measured resonant frequencies of the micro cantilevers with simulated resonant frequencies using fully detailed models of the cantilevers. The comparisons verify that fully detailed numerical models describe the experimental devices, and can be used to obtain simplified constitutive models of the periodic cell layer that can then be used with a two layer composite shell element formulation to simplify finite element models of complex MEMS fabricated from a periodically stiffened thin film.

Resonant Frequency Experiment Setup

Micromachined cantilevers were used to determine the bending stiffness of a stiffened silicon nitride film. The test structures were mechanically resonated with a piezoelectric shaker subjected to a variable frequency sinusoid signal. The response of the cantilevers was measured by reflecting a focused beam of light off the tip of the cantilevers and onto a photodiode array. The photodiode array measured the translation of the reflected beam due to cantilever vibration. The frequency of the sinusoid signal was varied to induce the first bending mode of the cantilever.

Figure 30 depicts the experimental setup described in this chapter. In this experiment the angle of the cantilever tip changes when the beam is deflected. The incident angle is defined as the angle that the reflected beam makes relative to horizontal.

A downward deflection of the cantilever tip results in a change in incident angle. The change in incident angle causes the reflected light beam to translate across the surface of the photodiode array. The photodiode array in the position-sensing detector (PSD) registers the translation as a voltage differential, which is captured by a data acquisition card. The resonant frequency was determined by locating the frequency at which maximum amplitude of oscillation occurred[2]. The support for the cantilever was designed to be as rigid as possible by extending the stiffening fins back into the silicon substrate.

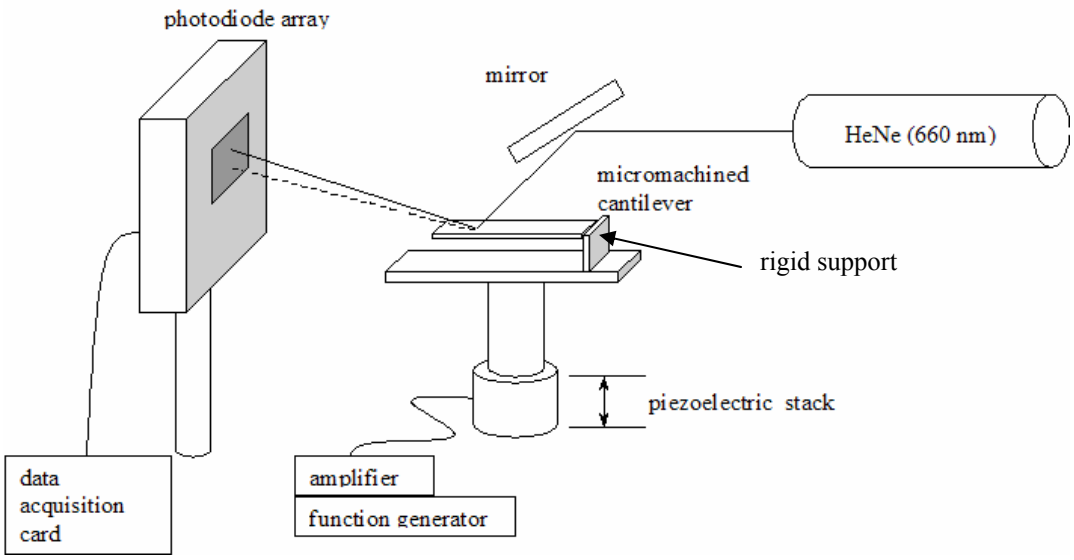


Figure 30 This figure depicts the experimental setup used to measure resonant frequencies of periodically stiffened cantilevers.

Cantilever Properties

The experiment described in this chapter was used to show that numerical simulations of fully detailed models can be used to accurately describe microfabricated stiffened cantilevers. The model was validated with experimental beams measuring 500

[2] Maximum amplitude of oscillation refers to the 1st bending mode of the cantilever.

um wide by 2000 um long with 50 um hexagonal and offset square cells. Figure 31 shows the characteristic dimension of each of these configurations.

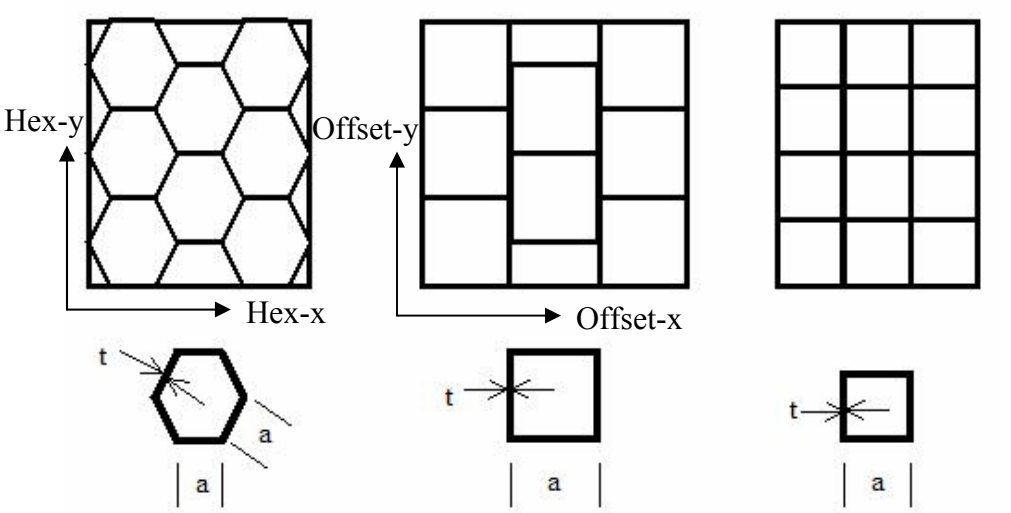


Figure 31 This figure shows the characteristic dimensions of each cell configuration. The x and y axes shown above correspond to the orientation of the cells with respect to cantilever width and length respectively.

Film Properties

In order to characterize the stiffened film, mechanical properties of the deposited (un-stiffened) film must be known. These properties include the film thickness, modulus of elasticity, Poisson's ratio and density. The nitride film thickness for these experiments varied between 1.4 um and 1.7 um, depending on the location of the wafer in the deposition chamber. The density of the film is assumed to be 3100×10^{-18} kg/um^3. This value has been well characterized [25] and is assumed to vary by less than 5% for the range of deposition parameters used in this process.

Poisson's ratio for silicon nitride is approximately 0.24. This value is valid for various deposition parameters and has been well characterized by [25]. The modulus of

elasticity for LPCVD silicon nitride, on the other hand, can range from 240 GPa to 270 GPa, depending on deposition conditions. Young's modulus for the film was determined experimentally by mechanically resonating a prismatic silicon nitride cantilever and measuring the response of the system as a function of frequency. This experiment served two purposes. First, the modulus of elasticity of the silicon nitride film was verified. Second, the validity of the experiment was verified on this simple cantilever beam before proceeding to the more complicated periodically stiffened beams.

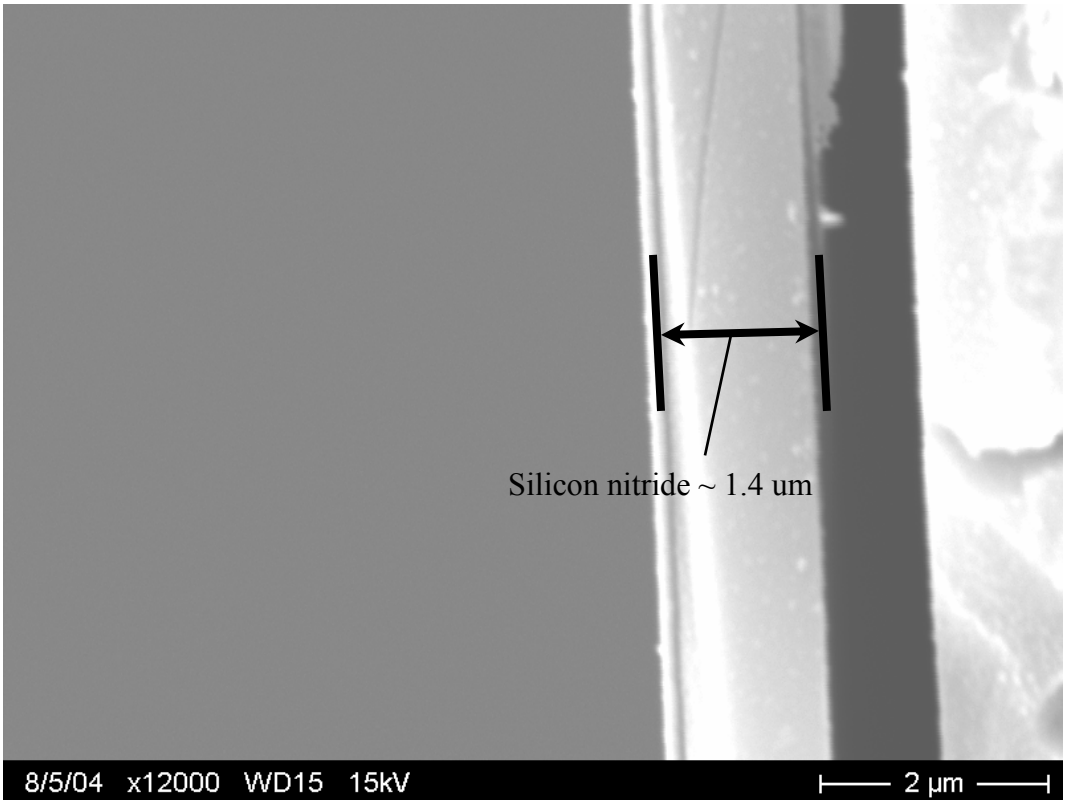


Figure 32 The SEM in this figure shows a 1.4 um thick layer of silicon nitride suspended over a silicon substrate.

Figure 33 shows a plot of the experimental and numerical frequency response for a 300 um long flat cantilever undercut at its base by 15 um. The film thickness for this

cantilever was 1.4 um thick as shown in Figure 32. Experimental data was collected with the setup shown in Figure 30. The numerical data was obtained by performing a harmonic analysis on an equivalent finite element model of the beam with an assumed Young's modulus of 240 GPa. The peak frequency response for the cantilever was found to occur at 20.3 kHz. The analytic solution for the resonant frequency of the beam based on the above Young's modulus agrees well with this result.

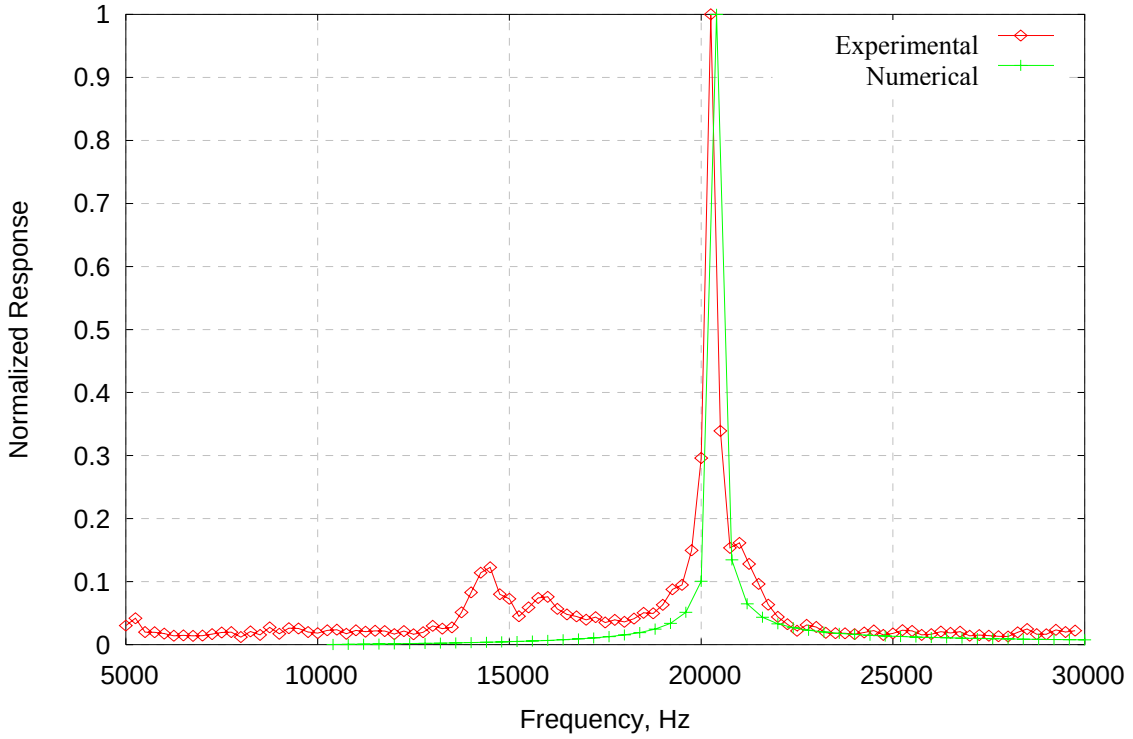


Figure 33 This figure shows a plot of the experimental and numerical frequency response for a 300 um long flat cantilever undercut at its base by 15 um. The peak frequency response occurs at roughly 20.3 kHz for both the experimental beam and the numerical simulation.

Analytic Solution of Young's Modulus

Young's modulus was estimated with analytic and numerical models. The analytic solution is derived below by developing an expression for the resonant frequency of a flat cantilever as a function of bending stiffness. The derived expression will be used later on periodically stiffened silicon nitride beams.

The equation of motion for a cantilever beam is found by considering the equation of motion for a simple single degree of freedom system,

$$m\ddot{x}(t) + c\dot{x}(t) + kx(t) = p(t)\,; \tag{8}$$

and its associated homogeneous form,

$$m\ddot{x}(t) + c\dot{x}(t) + kx(t) = 0\,. \tag{9}$$

In these equations *x(t)* is the displacement of the system, *m* is the mass of the system, *c* is a damping coefficient, *k* is the spring constant and *p(t)* is the forcing function applied to the system. The response for the un-damped system is given by:

$$x(t) = A_1 \sin \omega t + A_2 \cos \omega t\,. \tag{10}$$

where ω is the circular frequency of the system, measured in radians per unit time and has the following form:

$$\omega^2 = \frac{k}{m}\,. \tag{11}$$

The modulus of elasticity can now be determined by finding an expression for the free vibration of a cantilever in terms of *E* and *I*. This can be achieved with Rayleigh's method {ref here}, which has the following form:

$$\omega^2 = \frac{\int_0^L EI(x)\left[\psi''(x)\right]^2 dx}{\int_0^L m(x)\left[\psi(x)\right]^2 dx} \tag{12}$$

In this equation $\psi(x)$ is the normalized displacement at any position along the length of the beam and represents the 1st bending mode shape of the cantilever. The static deflection of a cantilever loaded only by its self-weight is given by:

$$\delta = \frac{\overline{m}gx^2}{24EI}\left(6L^2 - 4Lx + x^2\right) \tag{13}$$

and the maximum deflection at the tip is:

$$Z_0 = \frac{\overline{m}gL^4}{8EI} \tag{14}$$

Then the normalized shape function is:

$$\psi(x) = \frac{\delta(x)}{Z_0} = \frac{x^2}{3L^4}\left(6L^2 - 4Lx + x^2\right) \tag{15}$$

Substituting Equation 15 into Equation 12 and rearranging yields an expression for the modulus of elasticity, E, in terms of the circular frequency of the beam.

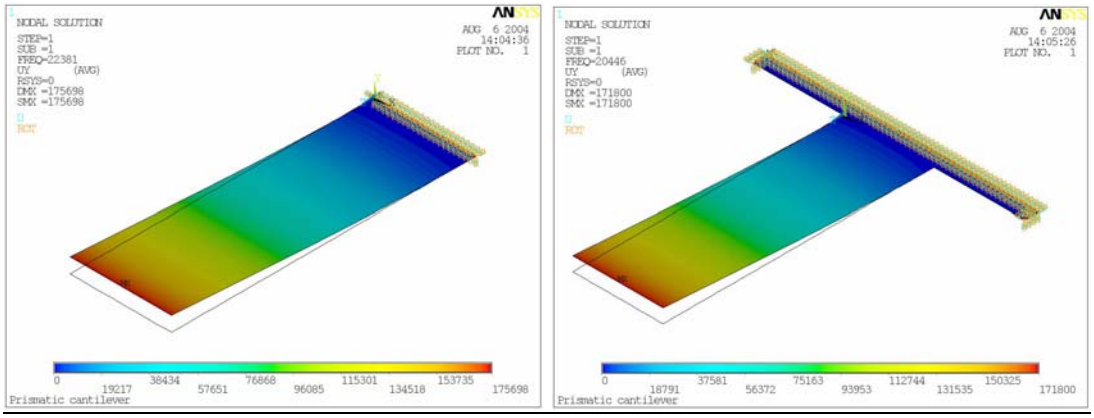
$$E = \frac{13}{162}\frac{\omega^2 L^4 \overline{m}}{I} \tag{16}$$

In this equation m is the mass per unit length of the film, L is the length of the cantilever, I is the cross-sectional moment of inertia, and ω is the circular frequency of the cantilever. Based on the experimentally obtained resonant frequency of 20.3 kHz and

assuming a characteristic beam length of 315 um, Equation 16 gives a modulus of elasticity of 244 GPa indicating that the assumed Young's modulus of 240 GPa is justified.

Numerical Solution to Young's Modulus

Numerical solutions for Young's modulus were obtained with a finite element simulation of the cantilever. Two models were considered for this study. The first model, shown in Figure 34 a, was a simple cantilever beam. In the second model, shown in Figure 34 b, the boundary conditions were modified to account for undercutting of the silicon nitride which occurred during the oxide etch (see Chapter 3 for details). In both of these models the translation and rotation degrees-of-freedom are fixed at the base of the cantilever (shown as wire-frame triangles in the Figure below). Both models gave reasonable resonant frequencies of 22 kHz and 20 kHz respectively, when an assumed Young's modulus of 240 GPa was used. Comparing the numerical and analytic models with experimental results as well as with published values for LPCVD silicon nitride, a modulus of elasticity of 240 GPa is a reasonable choice for this film.



(a) (b)

Figure 34 This figure shows a simple finite element model of a the experimental micro cantilever. The figure on the left shows the simplest boundary conditions with a perfectly supported base. The figure on the right shows a model with modified boundary conditions to account for undercutting of the silicon nitride which occurred during the oxide etch (see Chapter 3 for details).

Periodically Stiffened Cantilever Measurements

Resonant frequencies for the periodically stiffened film were determined using the experiment apparatus shown in Figure 30. Numerical solutions in the form of fully detailed finite element models of stiffened cantilevers were used to validate the experimental results. Numerical solutions for the 500 um by 2000 um cantilever with 50 um cells were found to be in good agreement with the experimental results. Figures 39-41 show the measured response of the micromachined cantilevers as a function of frequency. Numerical values for the first and second modes, corresponding respectively to bending and torsional vibration, are shown in Table 2. The close agreement between predicted and measured resonant frequencies for the first fundamental mode (bending) suggests that fully detailed finite element models of periodically stiffened micro cantilever beams can

be used to describe microfabricated cantilevers and as a reference to verify a simplified constitutive model for the periodically stiffened film.

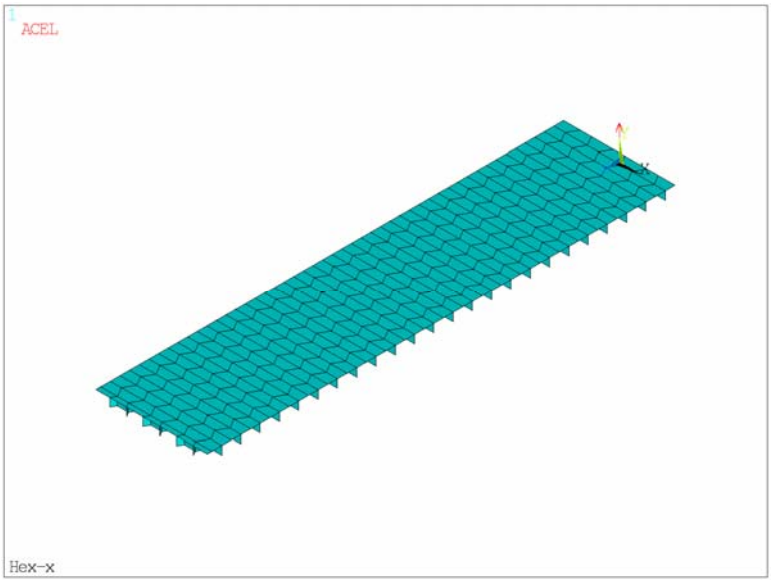


Figure 35 Finite element model of micro cantilever with hexagonal periodic stiffening cells.

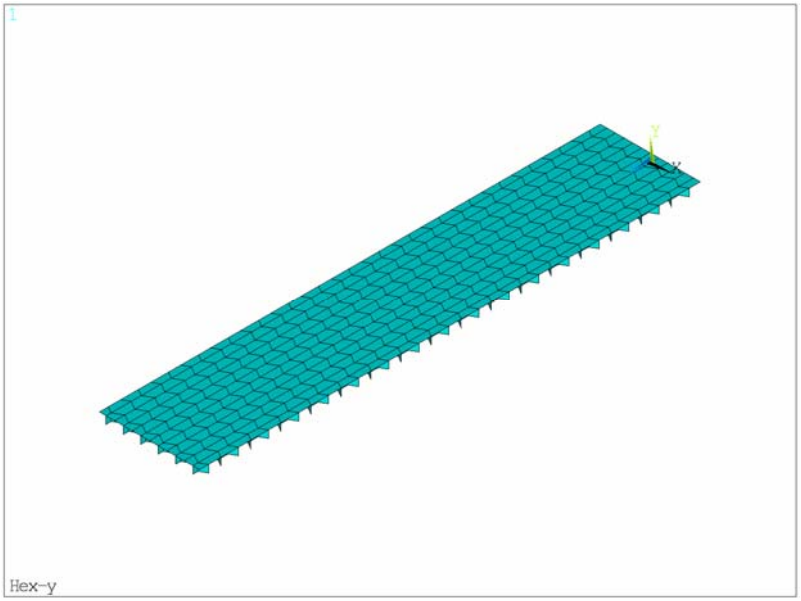


Figure 36 Finite element model of micro cantilever with hexagonal periodic stiffening cells.

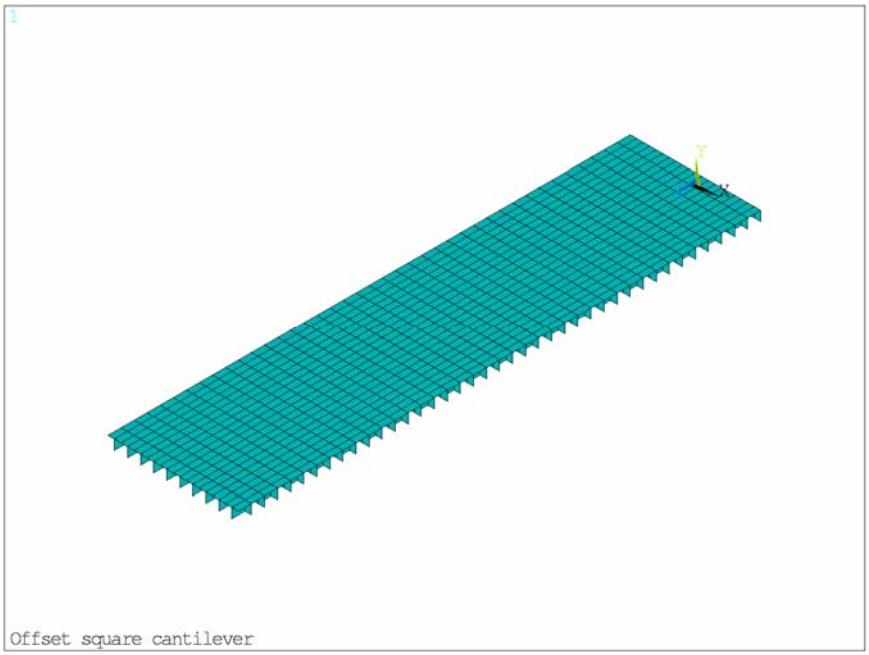


Figure 37 Finite element model of micro cantilever with offset square periodic stiffening cells.

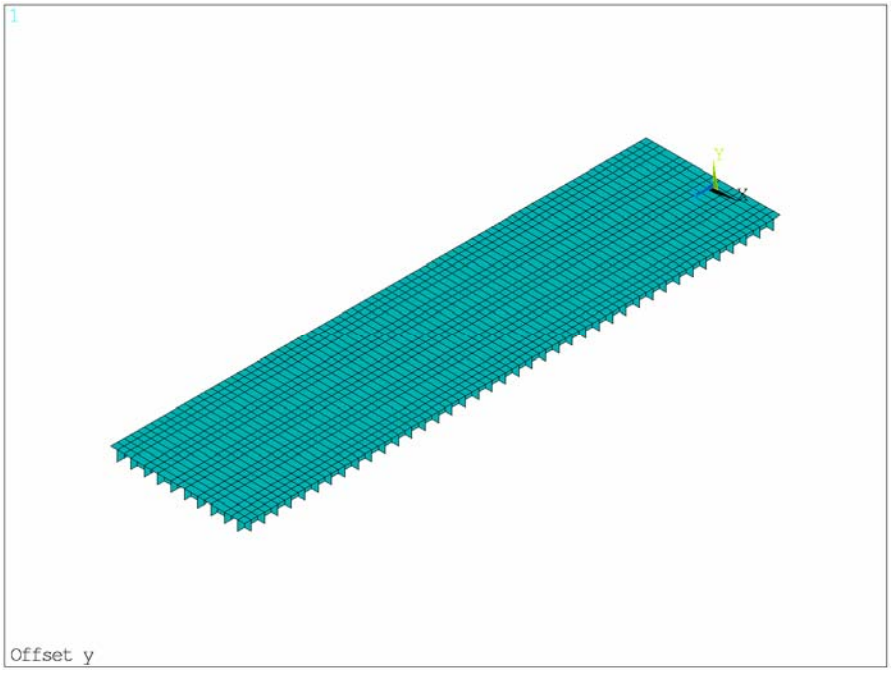


Figure 38 Finite element model of micro cantilever with offset square periodic stiffening cells.

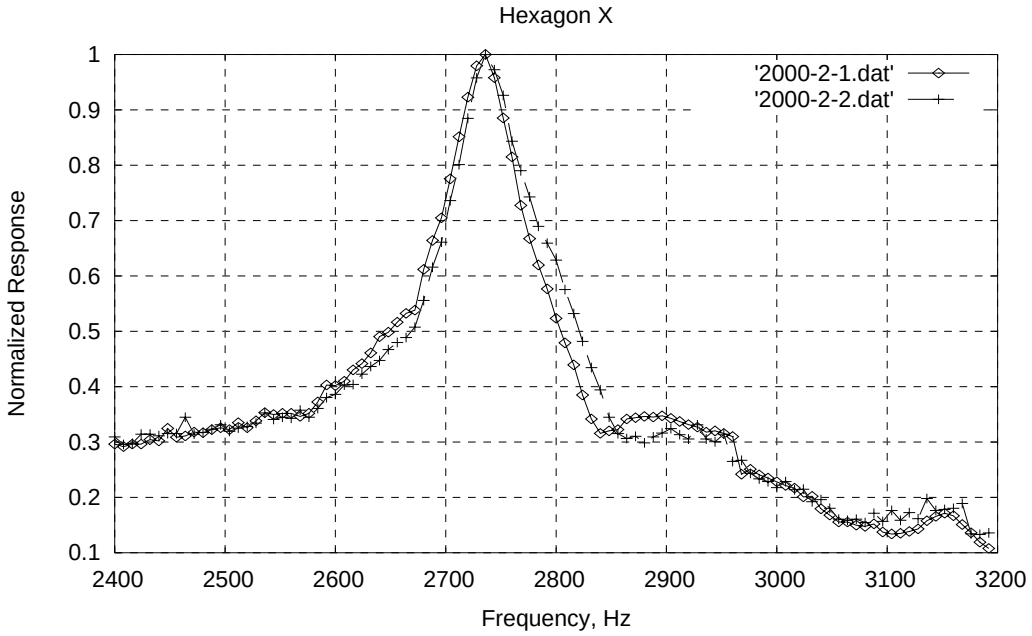


Figure 39 This plot shows the measured normalized tip response of two experimental periodic hexagonal cell-stiffened micro cantilevers as a function of excitation frequency.

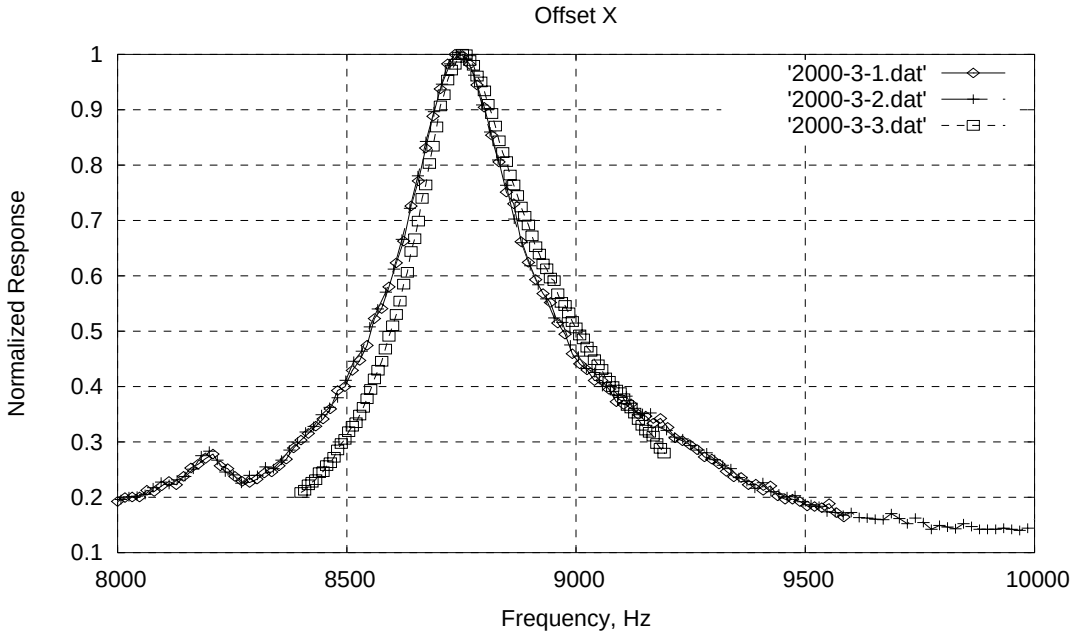


Figure 40 This plot shows the measured normalized tip response of three experimental periodic square cell-stiffened micro cantilevers as a function of excitation frequency.

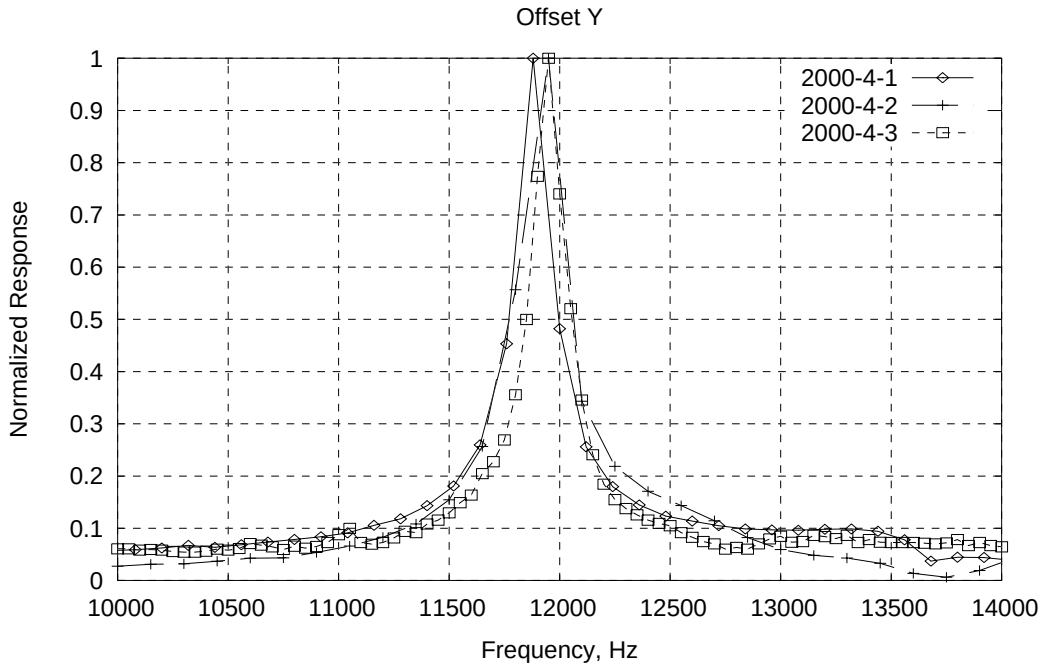


Figure 41 This plot shows the measured normalized tip response of three experimental periodic square cell-stiffened micro cantilevers as a function of excitation frequency.

Table 2 This table shows the measured and predicted resonant frequencies for the fundamental (bending) mode of the cantilevers.

Cell Type, h = 37 um	Cells Size, um	Experimental 1st Mode, Hz	Numerical 1st Mode, Hz
Hex-y	50	2800	2870
Hex-x	50	2740	2860
Offset-x	50	8740	8850
Offset-y	50	12000	12200

Conclusion

The study presented in this chapter shows that fully detailed numerical models of periodically stiffened micro-cantilevers can accurately predict the resonant bending frequency of experimental micro-cantilevers vibrated by a vertical base excitation. Resonant bending frequencies obtained with numerical models of the cantilevers were found to be in good agreement with measured resonant frequencies for each of the tested beams. This result verifies that fully detailed numerical models of simple periodically stiffened structures can be used to determine the behavior of such structures under bending loads. This result is used in the following chapter to obtain a simplified constitutive model for the periodic cell layer that can then be used with a two layer composite shell element to simplify models of complex MEMS fabricated from periodically stiffened thin films.

CHAPTER 6

STIFFENED FILM MODELS

In the previous chapter it was shown that finite element models can be used to model simple cantilever beams fabricated with periodically stiffened silicon nitride. In this chapter detailed finite element models are used to obtain simplified material properties for the stiffened film. In the first half of this chapter finite element models are used to obtain an equivalent bending stiffness, EI, and flexural rigidity, D, of rib-reinforced thin films with various cell shapes. Results from these simulations are used to obtain curves that describe the dependence of bending stiffness and flexural rigidity on cell type, cell breadth, film thickness and fin depth. The curves are useful for traditional analytic beam or plate models with relatively simple geometries.

In the second part of this chapter a method to obtain a simplified constitutive model for the periodic cell layer is presented. In particular, an effective modulus of elasticity, $E_{effective}$, of the rib-reinforced thin films with various cell shapes is determined from detailed finite element models. The effective modulus of elasticity is then applied to a layered composite shell element in ANSYS consisting of a solid top-sheet layer and a simplified cell layer representing the periodic cells. Although experimental results have been limited to square and hexagonal configurations (Chapter 5), the proposed numerical method is applicable to a wide range of cell configurations making it ideal for optimizing rib-reinforced thin films based on several different cell shapes.

The ultimate goal of this chapter is to present a method that significantly simplifies numerical models of MEMS fabricated with a periodically stiffened thin film. The simplifications introduced in this chapter result in a significant speed-up in analysis time.

Film Parameters

While variations of the proposed simplification methods have been applied to numerical models of large scale structures [31], we restrict our attention to material dimensions that are within an appropriate range for MEMS. For the numerical simulations presented in this chapter cell breadth, referred to as *a*, ranges between 25 um and 50 um. Film thickness, *t*, ranges between 1.0 um and 2.0 um and rib depths[3], *h*, vary between 20 um and 50 um. Figure 42 shows the critical dimensions for the square and hexagonal cells. The cell dimensions are shown in Figure 42.

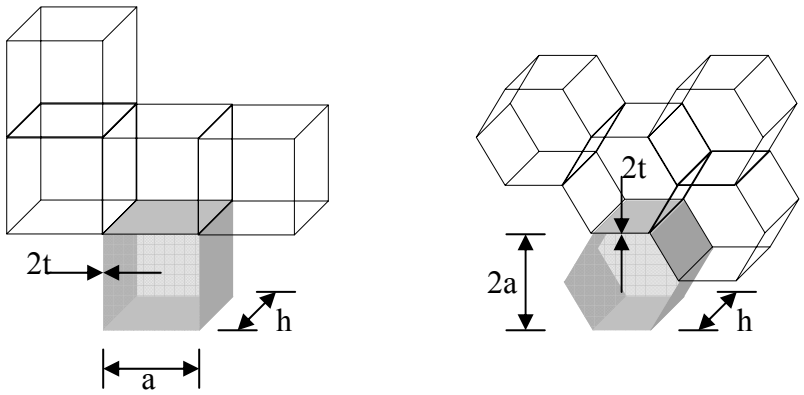


Figure 42 This figure shows the characteristic cell dimensions for a square and hexagonal cellular material. These dimensions will be referred to throughout the remainder of this thesis.

[3] Rib depth may also be referred to as fin height.

The isotropic material properties of LPCVD silicon nitride have been well documented (refs here). In order to validate the published results, Young's modulus was experimentally determined using a resonant method with cantilever beams fabricated from a 1.4 um thick layer of LPCVD silicon nitride. Experimental values were found to be in close agreement with previously published results. Young's modulus was found to be 240 GPa for the isotropic silicon nitride film. These results were described in detail in Chapter 5.

Stiffness Analysis

Bending Stiffness

The first method presented describes bending stiffness as a function of cell type, cell breadth, cell height and film thickness. This method is useful when analyzing MEMS with beam-like geometries. For this method and all subsequent methods, the cell wall is assumed to be twice as wide as the film thickness. This is due to the manner in which the silicon nitride fills the trenches as described in Chapter 3.

According to beam theory the bending stiffness of a prismatic beam is defined as the cross-sectional moment of inertia times the elastic modulus of the material. An inverse bending analysis can be performed to determine the bending stiffness, *EI*, of a beam for a given beam deflection and applied load. This is accomplished by considering that the curvature of a beam is related to the moment on the beam over the bending stiffness of the beam:

$$\frac{d^2w(x)}{dx^2} = -\frac{M}{EI}. \tag{17}$$

In the above equation w is the vertical beam deflection along the longitudinal axis, x. M is the applied moment on the beam and EI is the bending stiffness. The fourth derivative of the beam deflection with respect to x is related to the load on the beam as follows:

$$\frac{d^4w}{dx^4} = -\frac{q(x)}{EI}; \tag{18}$$

and the boundary conditions for a cantilever beam are:

$$-EI\frac{d^3w(0)}{dx^3} = \int_0^L q(x)dx, \tag{19}$$

$$-EI\frac{d^2w(0)}{dx^2} = \int_0^L xq(x)dx, \tag{20}$$

$$\frac{dw(0)}{dx} = 0, \tag{21}$$

$$w(0) = 0. \tag{22}$$

The deflection of a cantilever beam under a uniform distributed load can be obtained by solving the above differential equation and applying the above boundary conditions. The resulting deflection equation is:

$$w(x) = \frac{qx^2}{24EI}\left(6L^2 - 4Lx + x^2\right). \tag{23}$$

Substituting L for x and solving for EI yields an equation for the bending stiffness as a function of applied uniform load, beam length and tip deflection, δ:

$$EI = \frac{qL^4}{8\delta}. \tag{24}$$

The deflection of a uniformly loaded cantilever beam fabricated with a periodically stiffened silicon nitride film can be simulated using the finite element method. The resulting tip deflection predicted with numerical models can then be used with the above equation to determine the effective bending stiffness of the stiffened film.

The variables that have been considered for these analyses are listed below. These values represent common dimensions and geometries for the film considered in this research:

- Cell Type Hexagons and Squares
- Cell Size 25 um and 50 um
- Cell Height 30 um – 50 um
- Film Thickness 1.0 um – 2.0 um

The figure below shows the geometry and boundary conditions assumed for the finite element models. The equivalent finite element model for a 500 um by 2000 um cantilever stiffened with 50 um hexagonal cells is show in Figure 44.

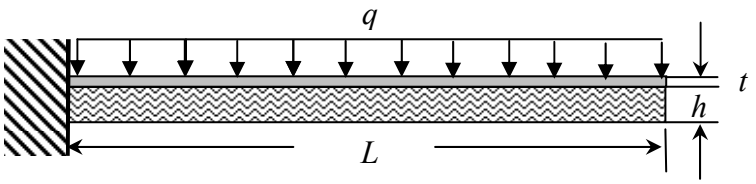


Figure 43 The figure above shows the geometry and boundary conditions for the finite element models used to determine bending stiffness, flexural rigidity and the effective modulus of elasticity for the stiffened film.

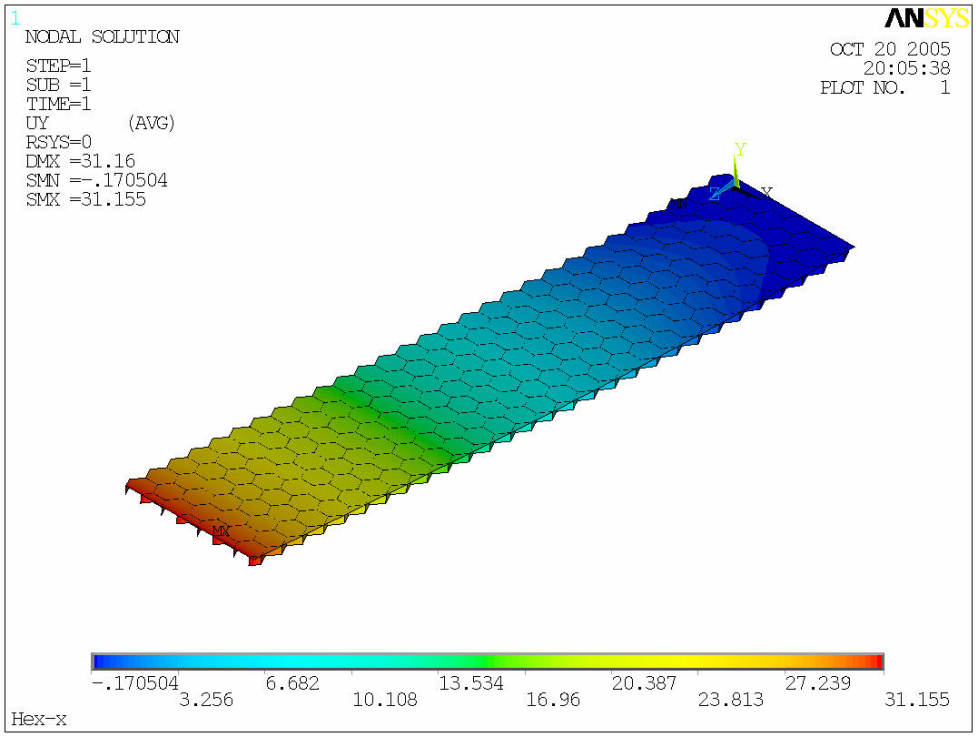


Figure 44 This figure shows the vertical displacement field of a fully detailed cantilever stiffened with 50 um hexagonal cells.

The plots below show the effect of cell breadth, cell height and film thickness on the simulated bending stiffness of a uniformly loaded cantilever beam fabricated with a periodically stiffened silicon nitride film. The bending stiffness in these graphs is given in terms of the calculated *EI* per unit width divided by the modulus of elasticity of silicon nitride.

Presenting the data in this way yields an *effective* moment of inertia. Bending stiffnesses can then be determined for a variety of thin films including silicon, silicon nitride or silicon carbide by multiplying the effective moment of inertia by the Young's modulus for a given material. For example, according to Figure 45 the bending stiffness

per unit width for silicon nitride stiffened with 50 um hexagonal cells is given by the product of the effective moment of inertia times the modulus of elasticity of silicon nitride. Then the bending stiffness for a 500 um wide beam can be found by taking the product of the modulus of elasticity, the effective moment of inertia and the width of the beam, in this case 500 um.

Figures 45 show numerical data for 25 um and 50 um hexagonal cells. The data in these figures tabulated below in Table 3.

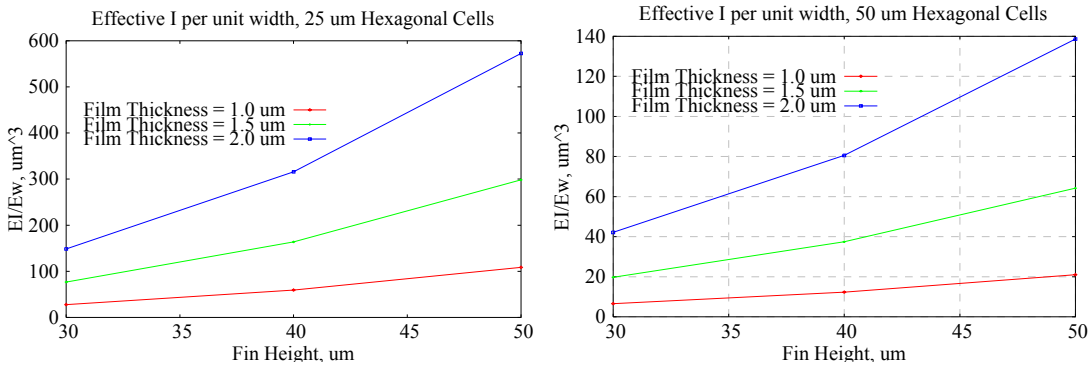


Figure 45 The plots above show the effective moment of inertia as a function of fin height and film thickness for a film stiffened with 25 and 50 um hexagonal cells.

Table 3 This table shows the effective bending stiffness for several hexagonal cell stiffened films.

t, um	h, um	a = 50, *EI/(Ew)*	a = 25, *EI/(Ew)*
1	30	6.54	27.60
1	40	12.28	59.20
1	50	21.00	108.69
1.5	30	19.77	76.65
1.5	40	37.44	163.66
1.5	50	64.23	298.33
2	30	42.12	148.48
2	40	80.53	315.93
2	50	138.64	572.52

Using the data in the above table a simplified polynomial can be used with the method of least squares to fit the data to a function that approximates the effective moment of inertia as a function of film thickness and rib depth. The following simplified polynomial is applied:

$$\frac{I}{E} = a_0 + a_1 t + a_2 t^2 + a_3 h^2 + a_4 th \tag{25}$$

The resulting coefficients for the effective moment of inertia per unit width as fit to the above equation are shown in the table below. These coefficients are valid for 25 and 50 um hexagonal cells.

Table 4 This table shows the coefficients for curves fit to the bending stiffness data presented in Table 3.

Coefficient	25 um Hexagon	50 um Hexagon
a0	224.97	79.95
a1	-656.04	-193.21
a2	103.43	38.84
a3	-0.14	-0.04
a4	15.66	3.76

To validate the above equation the calculated bending stiffness of a 500 um wide sample of 1.4 um silicon nitride fabricated with 50 um hexagonal cells measuring 37 um deep is compared with the experimental results from Chapter 5. Setting *t* to 1.4 um, *h* to 37 um and using the coefficients for the 50 um film with a Young's modulus of 240 GPa we obtain a calculated bending stiffness of 3.5e9 GPa um^4. Referring to Chapter 5 the experimentally measured bending stiffness for a stiffened silicon nitride film with the same configuration can be found by rearranging Equation 16. The effective bending

stiffness can be given in terms of the resonant frequency of the beam, the length of the beam and the mass per unit length of the beam:

$$EI = \frac{13}{162}\omega^2 L^4 \bar{m} \tag{26}$$

In Chapter 5 the resonant frequency for the first bending mode of a cantilever with the cell configuration given above was found to be approximately 2800 Hz. Using the value in the above equation gives an experimental effective bending stiffness of 3.7e9 GPa um^4 indicating that the above polynomial and calculated coefficients are valid. Furthermore, experimental and numerical results show that film stiffened with hexagonal cells behave as a transverse isotropic material therefore the coefficients in the above equation are invariant of the hexagon orientation in the plane of the film.

The figures and tables below show similar results for a thin film stiffened with regularly spaced square cells. Again, Equation 25 was used to fit the numerical data shown in Figure 6.5.

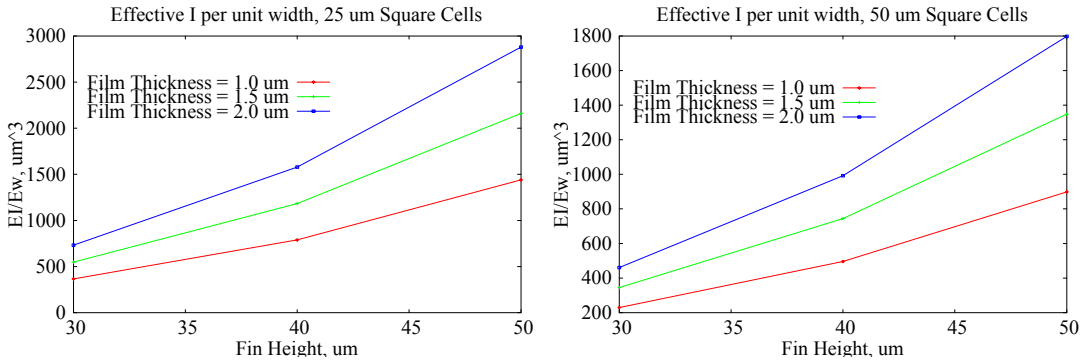


Figure 46 The plots above show the effective moment of inertia as a function of fin height and film thickness for a film stiffened with 25 and 50 um square cells.

Table 5 This table shows the effective bending stiffness for several square cell stiffened films.

t, um	h, um	a = 50, *EI/(Ew)*	a = 25, *EI/(Ew)*
1	30	230.00	365.39
1	40	495.78	789.10
1	50	898.50	1439.43
1.5	30	345.18	548.29
1.5	40	743.88	1183.89
1.5	50	1348.01	2159.43
2	30	460.57	731.38
2	40	992.20	1578.89
2	50	1797.74	2879.65

The resulting coefficients for the effective moment of inertia per unit width as fit to Equation 25 are shown in the table below. These coefficients are valid for 25 and 50 um square cells.

Table 6 This table shows the coefficients for curves fit to the bending stiffness data presented in Table 5.

Coefficient	25 um Hexagon	50 um Hexagon
a0	-198.56	-119.83
a1	-1047.34	-653.29
a2	0.43	0.43
a3	0.12	0.07
a4	47.78	29.85

Flexural Rigidity

The second method presented describes flexural rigidity of the stiffened film as a function of cell type, cell breadth, cell height and film thickness. This method is applicable when analyzing MEMS with plate-like geometry.

According to plate theory the curvature of a homogenous plate whose thickness is much smaller than its length and width is defined as follows:

$$D\frac{\partial^2 w(x,y)}{\partial x^2} = -M\ . \tag{27}$$

Where D is called the flexural rigidity and is defined as follows:

$$D = \frac{Eh^3}{12\left(1-\nu^2\right)}. \tag{28}$$

Now consider a long plate with thickness h simply supported at two opposing edges separated by a distance l and loaded with a uniform distributed load q. The moment due to the distributed load is:

$$M = \frac{q}{2}x - \frac{qx^2}{2}. \tag{29}$$

Substituting Equation 29 into Equation 27, solving for $w(x)$ and finally substituting $l/2$ for x yields and equation for the maximum deflection of the simply supported plate under a uniformly distributed load,

$$w_{\max} = \frac{5ql^4}{384D}. \tag{30}$$

The deflection of a simply supported, uniformly loaded cantilever plate fabricated with a periodically stiffened silicon nitride film can be simulated using the finite element method. The resulting center deflection predicted by numerical models can be used with the above equation to determine the effective flexural rigidity of the stiffened film. The same variables that were considered in the first method are again considered here. However, the geometry of the finite element models differs from the above examples as shown in the figure below.

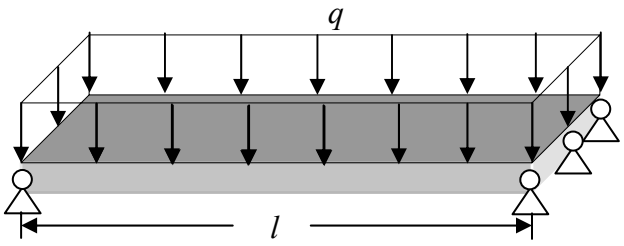


Figure 47 This figure shows the geometry of the simply supported plate used to determine the flexural rigidity of the stiffened film.

The equivalent finite element model is shown below. The model is a simply supported square plate with 50 um hexagonal cells and quarter symmetry as show in Figure 47.

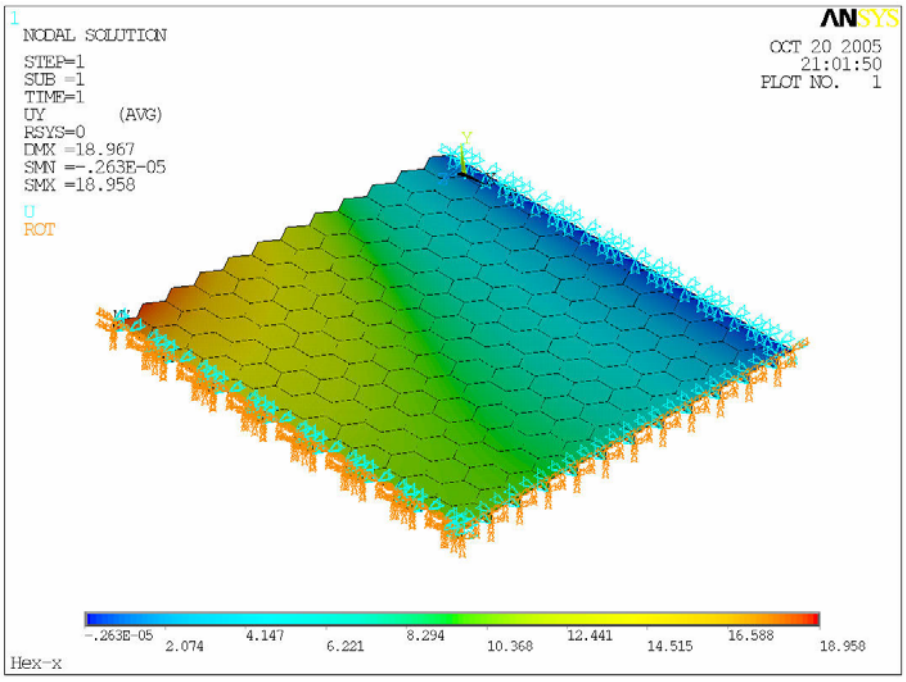


Figure 48 This figure shows the one of the simply supported plate models used to determine the effective flexural rigidity of the stiffened film. Symmetry planes are incorporated along two edges of the model.

The figures below show the effect of cell breadth, cell height and film thickness on the simulated flexural rigidity of a uniformly loaded, simply supported plate fabricated with a periodically stiffened silicon nitride film. The data is presented in terms of flexural rigidity, *D*, over the modulus of elasticity. Similar to the first method, presenting the data in this way yields an *effective* bending rigidity as a function of modulus of elasticity. In this case, the flexural rigidity for silicon nitride stiffened with 50 um hexagonal cells is given by the product of the effective flexural rigidity times the modulus of elasticity of silicon nitride.

Figures 49 shows numerical data for 25 um and 50 um hexagonal cells. The data for these figures is also given in Table 7.

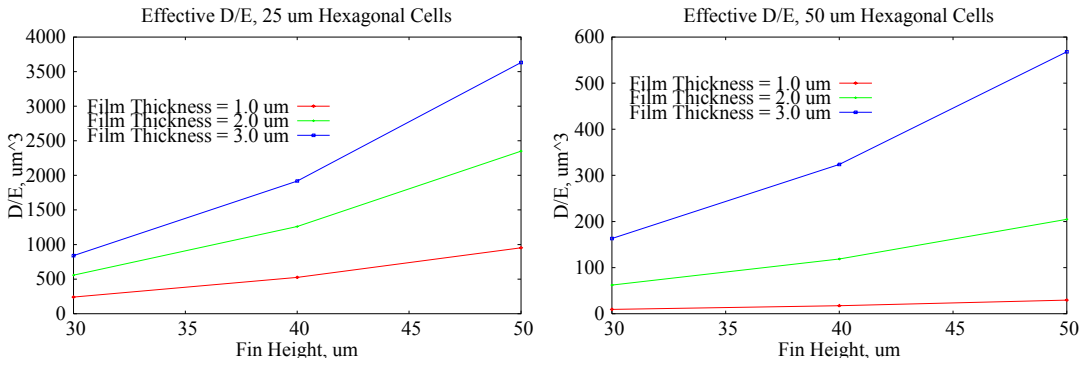


Figure 49 The plots above show the effective flexural rigidity as a function of fin height and film thickness for a film stiffened with 25 and 50 um hexagonal cells.

Table 7 This table shows the effective flexural rigidity for several hexagonal cell stiffened films.

t, um	h, um	a = 25, D/E	a = 50, D/E
1	30	240.771126	9.46372986
1	40	525.729796	17.4420647
1	50	953.660911	29.601938
2	30	556.956847	62.1720629
2	40	1259.7367	118.764898
2	50	2350.85184	204.863165
3	30	838.873754	163.201211
3	40	1918.75683	323.718307
3	50	3632.88024	568.147887

The resulting coefficients for the effective flexural rigidity as fit to Equation 25 are shown in the table below. These coefficients are valid for 25 and 50 micron hexagonal cells.

Table 8 This table shows the coefficients for curves fit to the bending stiffness data presented in Table 7.

Coefficient	25 um Hexagon	50 um Hexagon
a0	-115.33	207.44
a1	-1049.93	-429.68
a2	-37.40	56.66
a3	-0.12	-0.11
a4	49.45	9.24

The figures and tables below show similar results for a thin film stiffened with regularly spaced square cells. Again, Equation 25 was used to fit the numerical data shown in Figures 50.

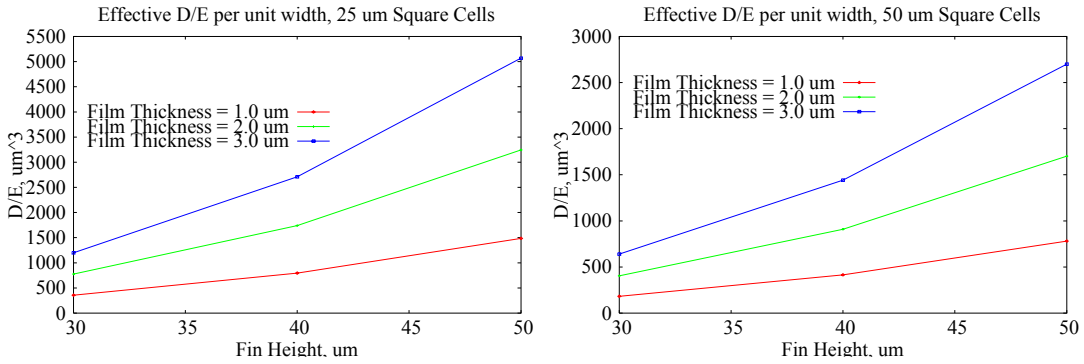


Figure 50 The plots above show the effective flexural rigidity as a function of fin height and film thickness for a film stiffened with 25 and 50 um square cells.

Table 9 This table shows the effective flexural rigidity for several square cell stiffened films.

t, um	h, um	a = 25, D/E	a = 50, D/E
1	30	354.703581	182.78086
1	40	794.639757	414.241798
1	50	1486.26991	781.228793
2	30	776.203112	404.485087
2	40	1738.35906	909.264238
2	50	3244.15556	1701.6152
3	30	1199.32859	640.400567
3	40	2709.56897	1441.81637
3	50	5069.02628	2699.83049

The resulting coefficients for the effective flexural rigidity as fit to Equation 25 are shown in the table below. These coefficients are valid for 25 and 50 um square cells.

Table 10 This table shows the coefficients for curves fit to the bending stiffness data presented in Table 9.

Coefficient	25 um Square	50 um Hexagon
a0	-41.51	14.31
a1	-1605.43	-905.03
a2	16.02	21.59
a3	-0.05	-0.34
a4	64.96	34.65

These two methods illustrate how the rigidity of a rib-reinforced film is affected by cell type, cell breath, film thickness and rib depth. The presented curves can be used with analytic solutions of beam and plate bending under various loads and boundary conditions to determine the deflected shape of simple models. However, as the complexity of the model geometry increases analytic solutions become increasingly difficult to obtain in which case numerical methods must be considered.

Effective Young's Modulus Calculation

While the two methods presented above work well for simple analytic approximations, a means to simulate MEMS with complex geometries fabricated with the proposed film is ultimately desired. The method presented below shows how layered shell elements can be used to simulate MEMS with complex geometries without the need to model each individual cell. This method is applicable only if an accurate effective Young's modulus for the cell layer can be determined. Once an effective Young's modulus has been determine it can then be used to approximate the detailed cell layer using a multi-layer shell element.

For the following analyses, it is assumed that the inhomogeneous periodically stiffened material can be treated as a homogeneous material. According to numerical experiments, this assumption is valid as long as the size of the inhomogeneity is much smaller than the overall dimensions of the material studied. In the case of periodically reinforced thin films presented in this research cell sizes ranged from 10 um to 50 um while the overall material being tested is on the order of several hundred microns.

Two slightly different approaches were considered for this study:

- Approach 1 – The entire rib-reinforced material was modeled with a single isotropic constitutive model.
- Approach 2 – The top sheet and underlying rib structure were treated as separate materials in a multi-layered shell element.

Obviously approach 1 is appealing because a single material model can be used for the rib-reinforced film. This approach however does not account for the asymmetric cross-section of the materials. For approach 2 the top sheet was considered to be a homogeneous isotropic material while the rib structure was considered to be homogeneous and isotropic but with a modified modulus of elasticity. This approach requires the use of a layered finite shell element to support the two separate material layers. The results presented in this research clearly show that the second approach results in models that are more accurate with only a slight increase in complexity over the first.

Both approaches were compared with fully detailed models to determine the accuracy and validity of the averaging techniques. The models were loaded as follows:

- Bending only,
- axial tension only.

Bending was achieved by applying a uniform distributed load to a cantilevered sample measuring 500 um wide by 2000 um long. Axial deflection was achieved by applying an axial displacement to the tip of the cantilever beam. The model dimensions are shown below in Figure 51.

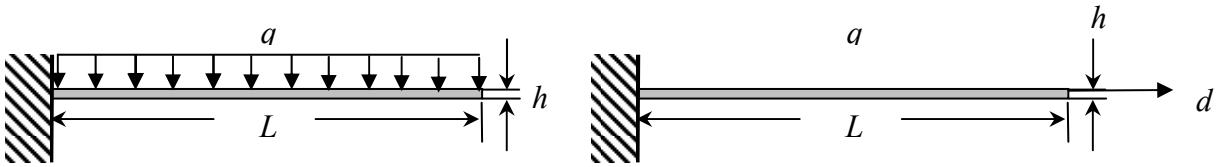


Figure 51 These figures show the two models and load cases used to determine the effective modulus of elasticity for the stiffened film. A uniform distributed load was applied to the cantilever to find the elastic modulus in bending while an eccentric axial displacement was applied to test the composite behavior of the shell elements.

The film parameters considered in this analysis are as follows:

- Cell types – square and hexagon
- Cell size – 50 um
- Rib depth – 37 um
- Film thickness – 1.4 um

Using Equation 24 to solve for *EI* based on the deflected cantilever model shown in Figure 52 and dividing *EI* by the moment of inertia for a homogeneous rectangular cross-section the effective modulus of elasticity can be determined for the film. This effective modulus of elasticity will be used in approach 1. Using a uniform load of 1e-5 uN/um^2 and assuming standard material properties for silicon nitride film with the above mentioned parameters the tip deflection of the cantilever shown in Figure 52 is 3.345 um. This results in an effective modulus of elasticity of 1267 MPa.

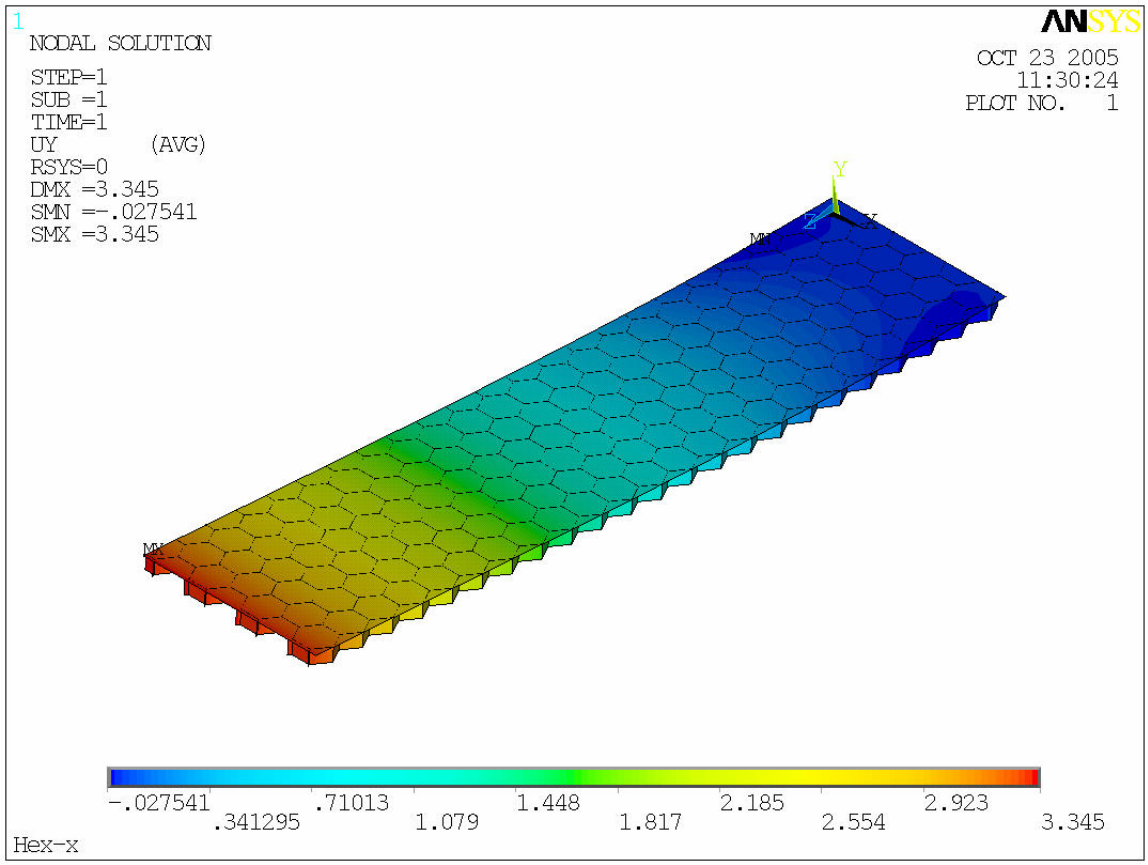


Figure 52 This figure shows the vertical displacement field of a fully detailed cantilever stiffened with 50 um hexagonal cells. The cantilever has been loaded with a uniform distributed load.

This value is used as the homogeneous equivalent modulus of elasticity for the cantilever simulated as a homogeneous material with single layer shell elements. The model consists of shell elements that are *t* plus *h* thick with a modulus of elasticity of 1267 MPa. The deformed shape of this model under the same uniform load as the previous detailed finite element model is shown in Figure 53. Note that the tip deflection is 3.345 um.

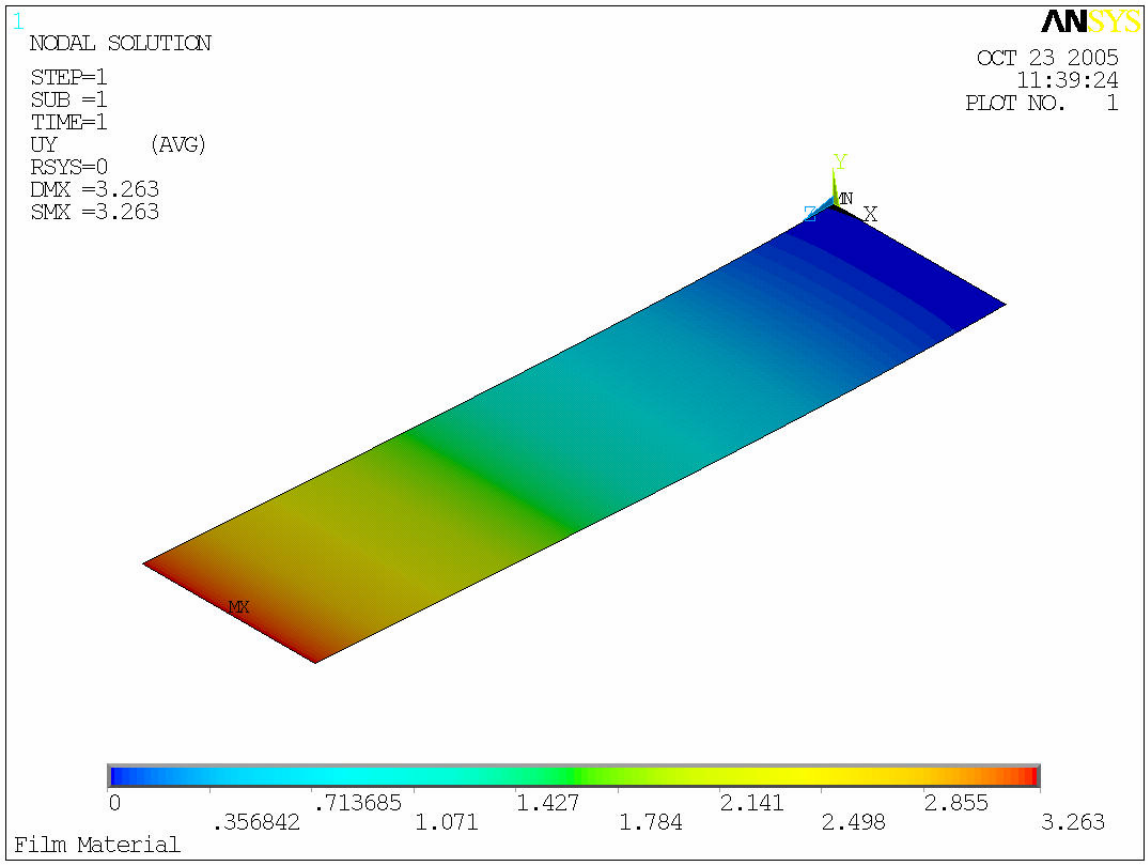


Figure 53 This figure shows the vertical displacement field of a simplified cantilever stiffened with 50 um hexagonal cells. The cantilever has been loaded with a uniform distributed load.

The above result is encouraging until an axial displacement test is considered. Since tensile post-release thermal strain has a significant effect on devices fabricated with stiffened silicon nitride films we must also verify that the proposed simplified approaches accurately handle in-plane axial loads. An axial displacement test is analyzed with the fully detailed model first. A 0.01 um axial displacement is applied to the tip of the cantilever sample. The asymmetric, composite cross-section of the material creates a bending moment in the material when it is axially loaded. Figure 54 shows the resulting

horizontal deflection. As show in Figure 55, the equivalent homogenous model cannot adequately account for the bending moment due to the composite cross-section.

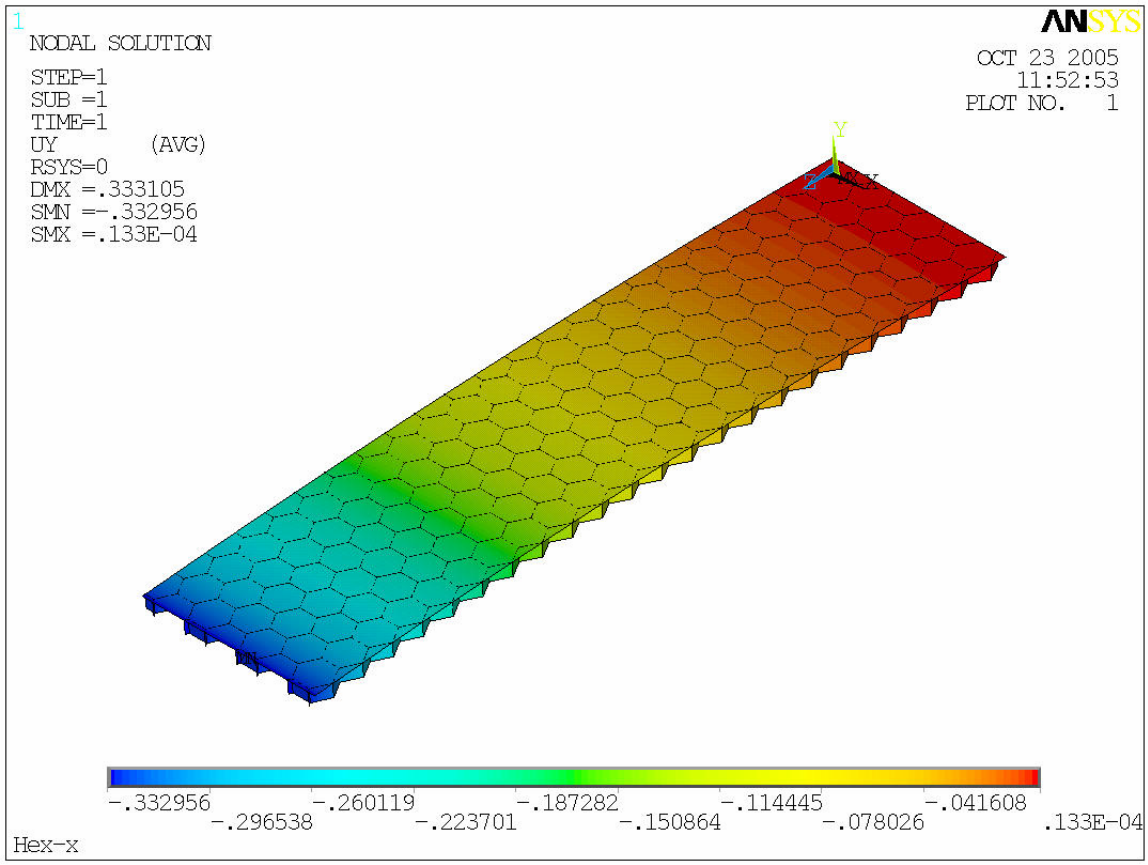


Figure 54 This figure shows the vertical displacement field resulting from a 0.01 um axial displacement applied to the tip of the cantilever.

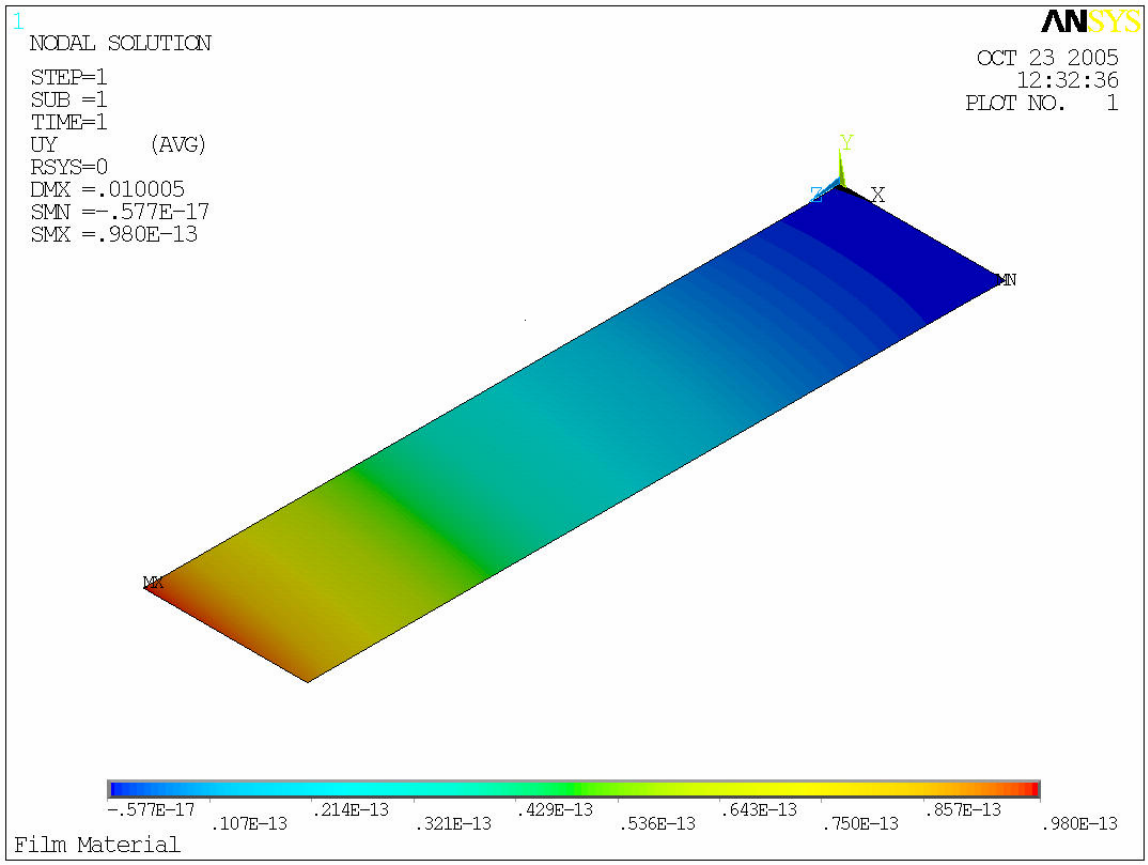


Figure 55 This figure shows the vertical displacement field predicted by the homogeneous model due to a 0.01 um axial displacement applied to the tip of the cantilever.

In order to account for the asymmetry a layered shell element is used. Two layers are used to describe the stiffened film. The top sheet material is modeled as isotropic silicon nitride while the bottom layer is taken to be a homogeneous isotropic material with an effective modulus of elasticity that approximates the stiffness of the honeycomb material. The critical task for this approach is in determining the effective modulus of elasticity. This is done by choosing a value for the effective modulus of elasticity that

results in a bending deflection most closely matching the bending deflection predicted by the fully detailed numerical model.

The effective modulus of elasticity for this example is determined using the bending deflection from the fully detailed model in the previous example. The procedure is enumerated below:

1. Determine the tip deflection of a fully detailed model loaded with a uniform distributed load.
2. Apply isotropic material properties to the top sheet material of the layered shell element.
3. Adjust the effective modulus of elasticity in the second layer of the layered shell element until the predicted bending deformation matches the fully detailed model.

Using a tip deflection of 3.345 um with the above procedure, the effective Young's modulus that most closely approximates the fully detailed model in bending is 8000 MPa. The vertical tip deflection resulting from an applied axial displacement can now be simulated with the layered shell element model. This test verifies that the layered shell element can adequately handle the asymmetric cross-section of the stiffened film. Figure 56 shows the vertical deflection of the layered shell element model resulting from an applied axial displacement of 0.01 um.

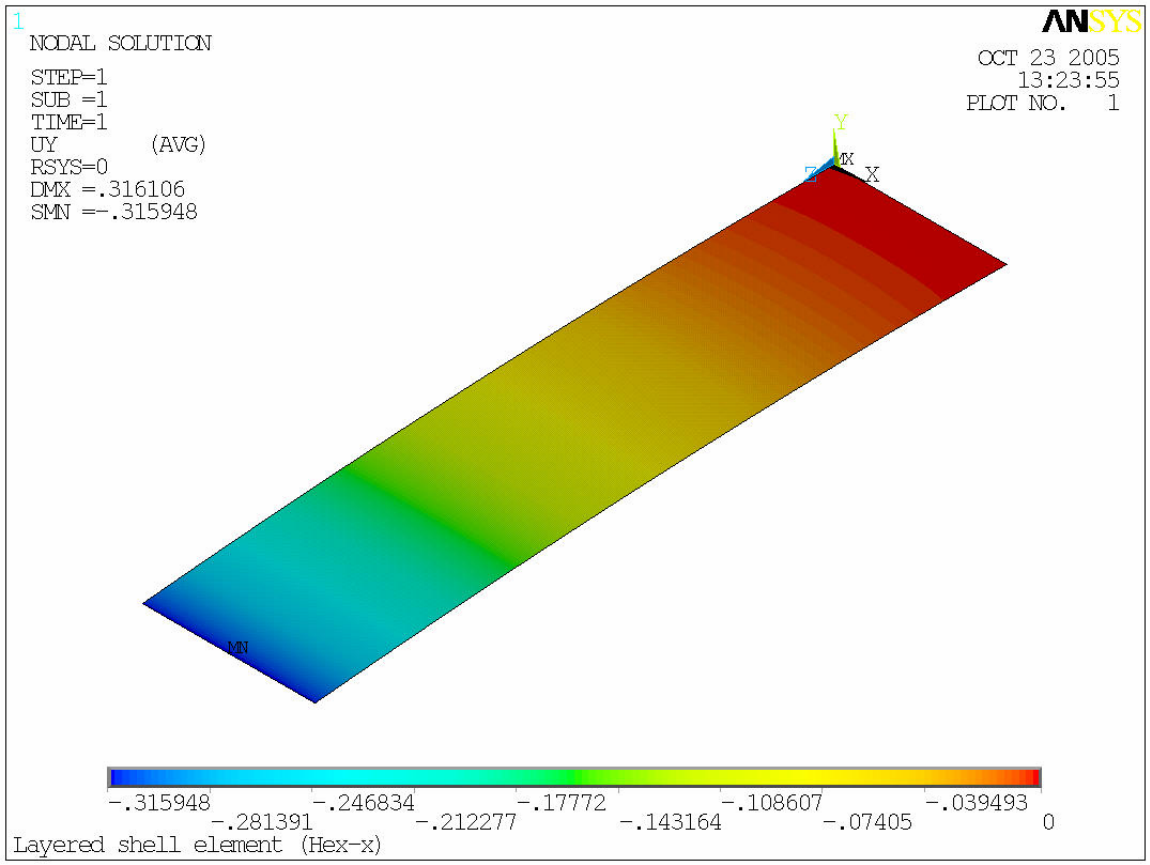


Figure 56 This figure shows the vertical displacement field resulting from a 0.01 um axial displacement applied to the tip of the layered shell cantilever model. Note that the layered shell element accounts for the film's composite cross-section.

Despite the 5% difference between the fully detailed model and the layered model, this result is promising as a simplification method since bending under an axial displacement can be accounted for. This approach will be used in the next chapter to model single axis and biaxial scan mirrors under a variety of loading conditions. The simplified models resulting from the proposed technique will be validated against fully detailed models and experimental data.

Summary

Finite element models were used to determine the equivalent bending stiffness, *EI*, and flexural rigidity, *D*, of rib-reinforced thin films with various cell shapes. The simulations were used to show the effect cell type, cell breadth, film thickness and fin depth on bending stiffness and flexural rigidity. A method was also introduced to obtain the effective modulus of elasticity, $E_{effective}$, of rib-reinforced thin films with various cell shapes. This method used detailed finite element models of the rib-reinforced film to determine an effective or average modulus of elasticity for the cell layer. The effective modulus of elasticity was then applied to a layered shell element in ANSYS consisting of a solid top-sheet and a homogenized cell layer. The resulting simplified layered model adequately predicted the deformed shape of simple cantilevers under bending and axial load.

CHAPTER 7

MIRROR ANALYSIS AND NUMERICAL MODEL VALIDATION

A layered shell element was used in the previous chapter to model the stiffened film. This material model will now be used to simulate single axis scan mirrors fabricated at the Stanford Nanofabrication Facility. Several load configurations will be simulated with the proposed material model using the finite element analysis software package ANSYS. Static and dynamic analyses will be performed with the software to investigate the effects of post-release thermal strain, electrostatic force and inertia on the surface deformation of the mirrors. The results of these simulations will be compared with similar simulations of fully detailed models as well as experimental results. The fully detailed models are employed to validate the proposed modeling simplification. The results will show that the simplified models employing the layered shell element can adequately simulate the mirrors while reducing the model complexity and computation time.

Experimental Mirrors

Single axis and biaxial scan mirrors were fabricated at the Stanford Nanofabrication Facility using the fabrication technique described in Chapter 3. The mirrors were electrostatically actuated by applying a voltage to electrodes on the perimeter of the mirror surface and grounding the substrate beneath the mirror. A single

axis scan mirror is shown in Figure 57. The single axis mirror is fully stiffened with stiffening fins across the backside of the mirror surface.

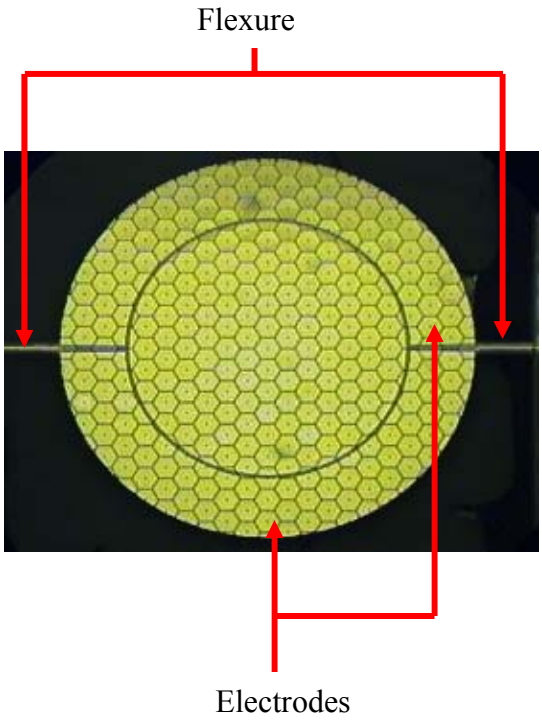


Figure 57 This figure shows a single axis scan mirror measuring 1500 um in diameter stiffened with 50 um hexagonal cells. The flexures are 200 um long, 20 um wide and 1.4 um thick. The film thickness is 1.4 um and the fin depth is 37 um. The electrode pads form two half annuli around the perimeter of the mirror with a width of 200 um.

The film thickness for the experimental mirrors is 1.4 um and the fin depth is 37 um. The bulk post-release thermal strain in the film, based on Guckel ring measurements, is 80 MPa and the post-release thermal strain gradient through the film thickness is 5 MPa, based on cantilever measurements. Geometry specifications for the single axis given in the table below.

Table 11 Geometric parameters for the validation single axis mirror.

Parameter	Value
Disk Diameter	1500 um
Electrode Width	200 um
Flexure Length	50 um
Flexure Width	20 um
Cell Type	Square and Hexagon
Cell Size	25 um and 50 um

Figure 58 depicts the front and back of a single axis micro mirror fabricated with a periodic hexagonal pattern. The accompanying scanning electron micrograph in Figure 58 shows the back side of a large area single axis scan mirror fabricated with 50 um honeycomb cells.

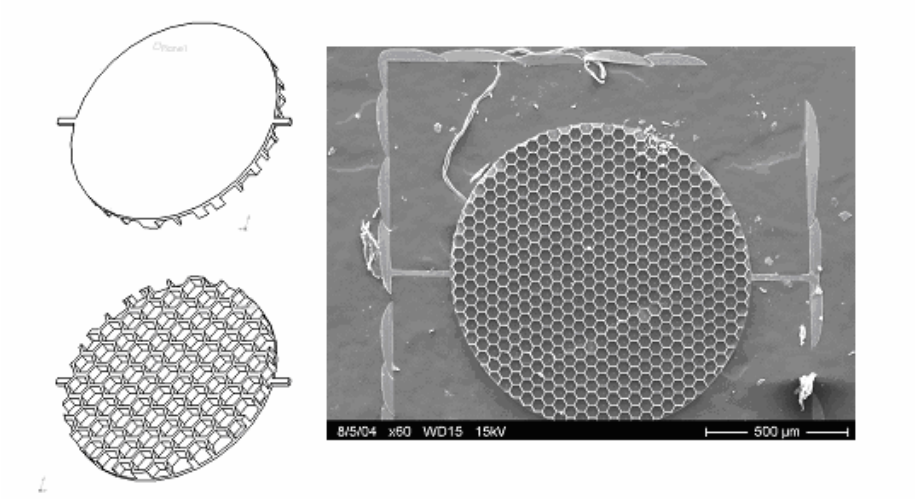


Figure 58 This figure shows a conceptual model of the stiffened single axis scan mirrors and a scanned-beam electron micrograph of the backside of one of the experimental mirror.

Surface Profile Analysis and Characterizations

Electrostatic Force

The first load case to be considered is also the simplest to simulate. For this analysis we examine the effect of a constant electrostatic force on the surface profile of a single axis scan mirror. The mirrors tested in this research have been actuated in a tilt and hold load configuration with up to 200 volts without any measurable surface deformation. In this configuration, an electrostatic force is applied to one electrode for a relatively long duration forcing the mirror into a temporarily fixed tilted configuration. The angular deflection of the mirror depends on the applied voltage and the distance between the mirror and the substrate as well as the length, width and thickness of the flexures.

An analytic solution for the angular deflection as a function of applied voltage is derived by starting with an expression for the torque on a bar as a function of the bar geometry and the torsional rotation of the bar. The expression is given as:

$$T = \frac{\theta k G}{l}. \tag{31}$$

Where theta is the rotation of the bar with respect to the bar's cross-section, k is the torsion constant for the flexure cross-section, G is the shear modulus of the film and l is the length of the flexure.

Torque is applied to the flexures via an electrostatic actuation force. The electrostatic force on the electrodes is derived from the equation for a parallel plate capacitor. The electrostatic force between two plates is given as by,

$$F = \frac{\varepsilon_o A}{2}\frac{v^2}{d^2}. \tag{32}$$

Where A is the area of the electrode, v is the applied voltage, d is the separation distance between the two plates and epsilon is the permittivity of free space. The torque on the mirror flexures is defined as the integral of the electrostatic force times xdx. Combining this with Equation 31 yields an expression for the angular rotation as a function of electrostatic torque,

$$\int x \cdot F dx = \frac{\theta k G}{2l}. \tag{33}$$

For a circular plate this equation takes the following form:

$$\frac{\varepsilon_o A v^2}{2}\int_0^R x\cos^2\theta \frac{\sqrt{R^2 - x^2}}{\left(D - x\sin\theta\right)^2} dx = \frac{\theta k G}{2l}. \tag{34}$$

Where D is the initial separation between the disk and the substrate and R is the radius of the disk. Solving for v in terms of theta yields the following equation for the voltage as a function of flexure geometry, shear modulus and angular rotation:

$$v = \sqrt{\frac{\theta k G}{C l \varepsilon_o \cos^2\theta}}, \quad C = \int_0^R \frac{x\sqrt{R^2 - x^2}}{(D - x\sin\theta)^2} dx \qquad (35)$$

Assuming a pit depth of 200 um and using the geometric configuration for the single axis mirror given above the flexure rotation versus applied voltage is plotted in Figure 59. Taking 10 degrees as the upper limit of mechanical rotation an approximate uniform force can be calculated based on the voltages in Figure 59.

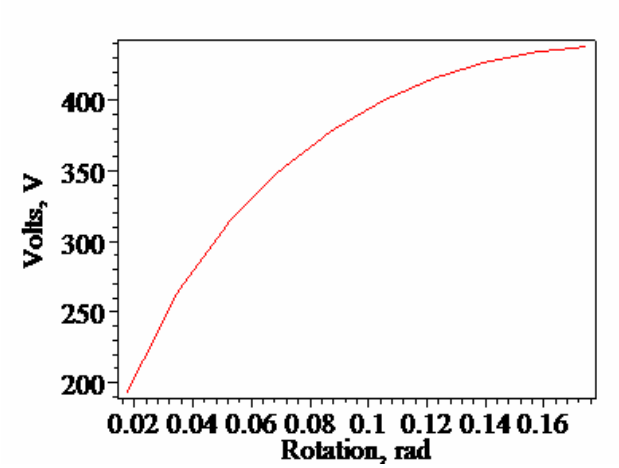
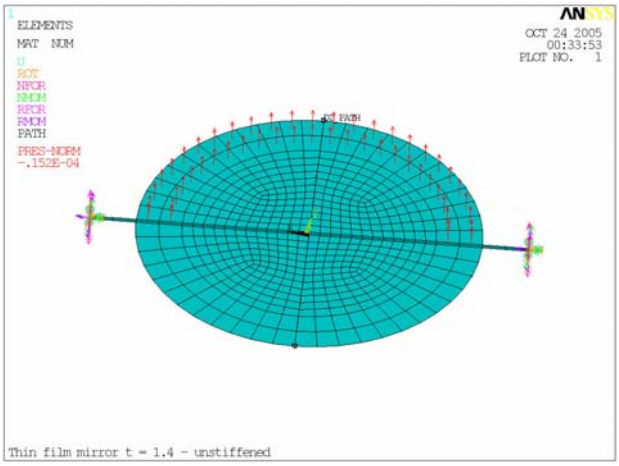


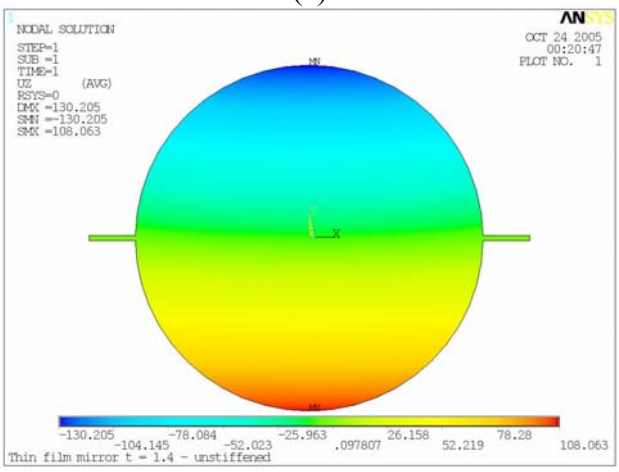
Figure 59 This figure shows a plot of the theoretical actuation voltage required to rotate a single axis scan mirror through 10 degrees. The mirror diameter is 1500 um and the gap depth is 300 um.

Although coupled electrostatic-mechanical analysis is possible with ANSYS the modeling complexity and computational overhead associated with such an analysis is impractical for rapid design and optimization. Therefore the nonlinear dependence of electrostatic force on mirror angle is ignored and a uniform load is used instead. This is a valid assumption for a first-order analysis. The uniform distributed load is calculated from the voltage corresponding to 10º mechanical rotation given in Figure 59.

A finite element model of a single axis scan mirror with a uniform distributed load applied to its upper electrode is shown in Figure 60. The vertical displacement of the mirror corresponding to the uniform load is also shown in this figure. Figure 61 shows the vertical deflection and nodal rotation about the x-axis (respectively) of an un-stiffened 1500 um diameter mirror with a continuous film thickness of 1.4 um tilted 10º due to a uniform load applied to the upper electrode.



(a)



(b)

Figure 60 Figure (a) shows a finite element model of an un-stiffened plate with a uniform distributed load applied to the outer electrode of the mirror. Figure (b) shows the vertical mirror deflection due to the distributed load.

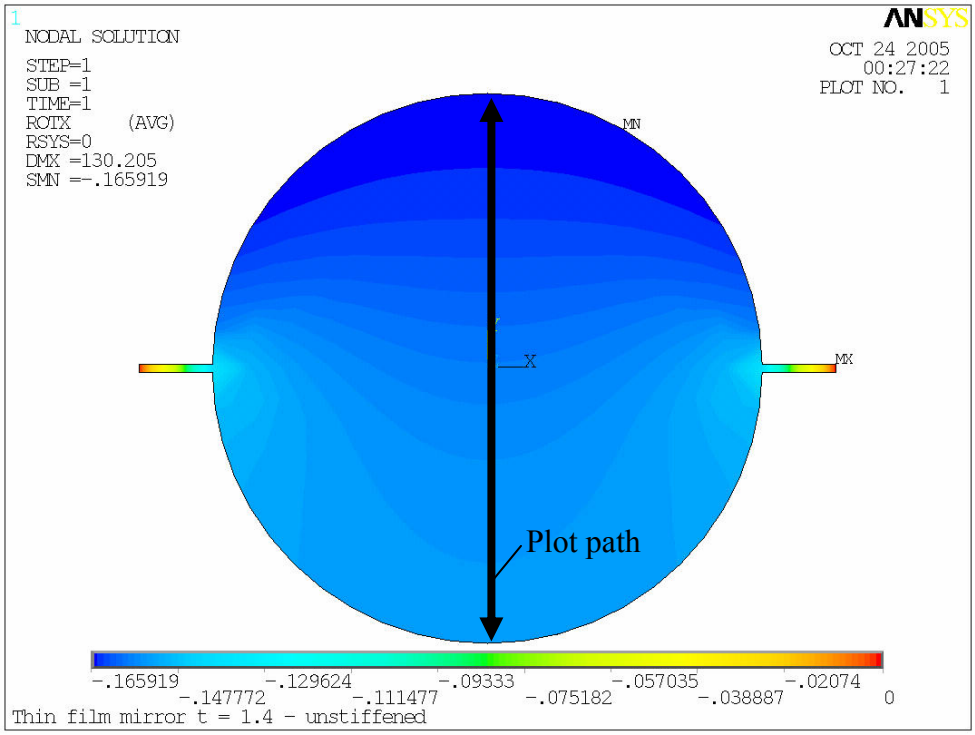


Figure 61 This image shows the nodal rotation about the x-axis of the mirror due to a uniform load applied to one electrode. A plot path is labeled indicating the direction and location of the surface profile data shown below.

An ideal mirror surface would remain flat as it is tilted through 10 degrees. This is obviously not the case as seen in Figure 61. Figure 62 shows a plot of the predicted nodal rotation about the x-axis taken along the plot path shown in Figure 61 above. This plot was created by fitting a fourth order polynomial to the simulated z-deflection. The constant term in the polynomial corresponds to the stroke of the mirror due to flexure bending, the linear term corresponds to the rotation of the mirror due to the applied load and the higher order terms correspond to the mirror curvature due to the deformation of the mirror surface under the applied load. The linear and constant terms are removed from the equation to emphasize the surface profile during mirror rotation. As can be seen in this plot using an un-stiffened 1.4 um thick film for the mirror surface results in a 3.31

peak-to-trough surface deformation across the mirror surface under electrostatic actuation. Assuming these mirrors will operate in an optical communication environment near 1550 nm with a desired resolution of at least lambda by 10 the corresponding surface deformation for this mirror of lambda by 0.45 makes the un-stiffened mirror unacceptable for this type of application.

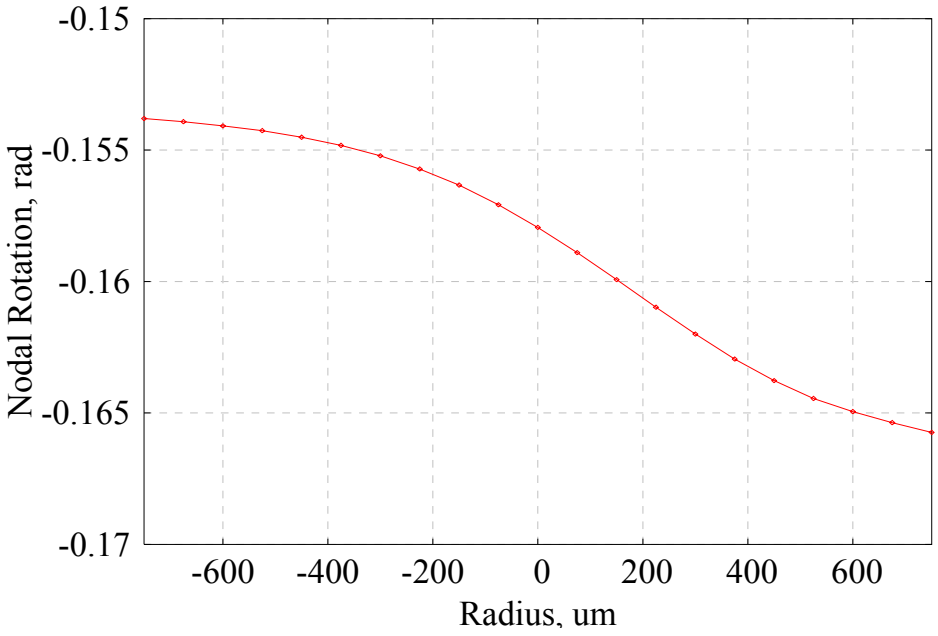


Figure 62 This figure shows a plot of the nodal rotations about the x-axis for an un-stiffened single axis mirror under a uniform distributed load which produces 10 degrees of mirror rotation. Note that a perfectly flat mirror would have a constant nodal rotation across its diameter.

A stiffened mirror is now considered. The mirror is stiffened with vertical ribs oriented in square patterns with a cell size of 50 um. The rib depth is 37 um and the film thickness is 1.4 um. The same load is applied to this mirror as was applied to the un-stiffened mirror shown above. Surface deformations predicted from the fully detailed and simplified models are both shown. A layered shell element was used for the simplified

model per the technique discussed in the previous chapter. An effective Young's modulus of 14 GPa was used for the periodic cell layer. The simulated nodal rotations for the stiffened mirror about the x-axis taken along the plot path shown in Figure 61 above are shown in Figure 63 below.

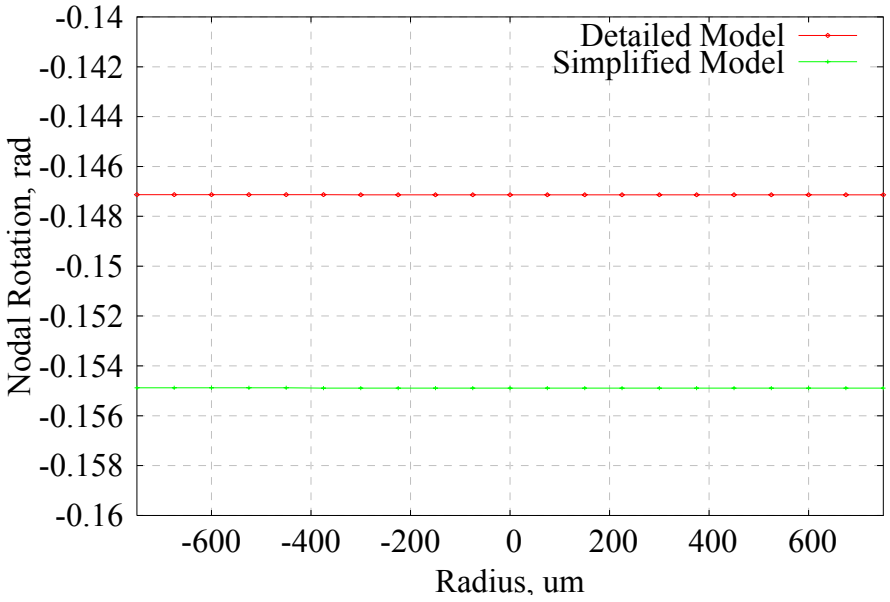


Figure 63 This figure shows a plot of the nodal rotations about the x-axis for an 50 um square stiffened single axis mirror under a uniform distributed load which produces 10 degrees of mirror rotation. Both the detailed and simplified models show the nodal rotations to be flat indicating that the curvature due to electrostatic force is negligible.

The predicted surface deformation due to the applied voltage is well below the lambda by 10 limit. Surface profile measurements of this stiffened mirror for a tilt-and-hold load case at 200V showed no measurable surface deformation due to the applied electrostatic force. The resolution of the surface profilomter used for this measurement is on the order of nanometers. Therefore, the experimental observation is justified.

Post-release Thermal Strain

The effect of post-release thermal strain on surface deformation is now considered. LPCVD Silicon nitride can have high residual or intrinsic stresses. This post-release thermal strain is often the extreme load case driving the design of MEMS fabricated form silicon nitride. Post-release thermal strain in LPCVD silicon nitride arises from a combination of high temperature deposition, typically between 800ºC and 1300ºC, coupled with a CTE (coefficient of thermal expansion) mismatch between the silicon nitride (CTE ~ 3.2) and the substrate material such as silicon (CTE ~ 2.6). The extent of this effect becomes apparent once the silicon nitride is selectively separated from its substrate. Once separation between the two materials has occurred the silicon nitride will tend to shrink in order to alleviate thermal strain built in during deposition. If however the silicon nitride is tethered to the substrate by a material with a different CTE a stress field is setup throughout the film with large stresses concentrated near the tethers and support. This phenomenon can lead to catastrophic failure of devices if not taken into consideration during the design phase of a device. For example, the theoretical un-stiffened mirror presented in the previous example would not survive release even at the lowest possible post-release thermal strain levels attainable with LPCVD techniques. Post-release thermal strain in the material coupled with the compliant film would cause the mirror surface to cup and pull inward on the flexures setting up a tensile stress field exceeding the ultimate stress of the silicon nitride.

The numerical models presented in this work have been extended to account for biaxial (in-plane) post-release thermal strain in the silicon nitride. This is accomplished in

ANSYS by specifying the appropriate coefficients of thermal expansion for each material and performing a thermal analysis on the model. The in-plane thermal strain in the silicon nitride combined with a density gradient through the thickness of the film is most likely the cause of the curvature observed in the devices. This curvature can be measured with simple prismatic micro-cantilevers. Simulating the curvature of such a simple device can be accomplished by applying a stress gradient through the thickness of the film. However, for devices any more complicated than a simple cantilever this simplification is not justified as the density gradient is suspected to be a function of boundary conditions and substrate topology. The density gradient property was not considered in the finite element models.

Figure 64 shows interference fringes in two orthogonal directions across a single axis scan mirror with a diameter of 1500 um (imaged at 660 nm). The mirror shown in this image is in a static, unloaded state. The slight curvature in the fringe lines shows the effect of post-release thermal strain and density gradient on the mirror surface. The fringes in the interference images correspond to less than 1 um surface deviation across the 1500 um optical surface.

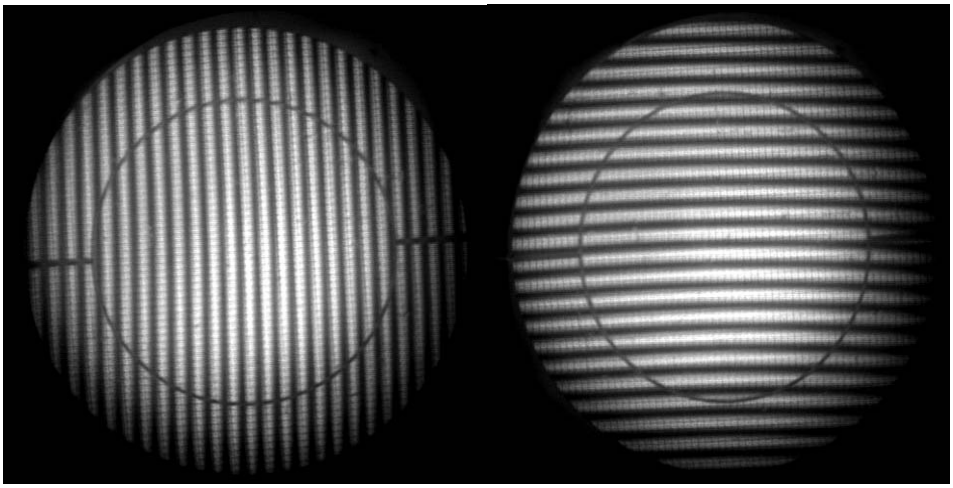


Figure 64 This figure shows interference fringes in two orthogonal directions across a single axis scan mirror with a diameter of 1500 um. The mirror shown in this image is in a static, unloaded state. The slight curvature in the fringe lines shows the effect of residual stress on the mirror surface.

The figures below show surface profile data taken for several single axis scan mirrors. The plots show surface profiles in two orthogonal directions across the surface of the mirrors. A slight astigmatism shown in these plots was observed in all of the mirrors tested. It is also interesting to note that the astigmatism is switched for the two cell types. This was also observed in all mirrors tested. Of particular interest in Figure 65 and Figure 66 is the effect of cells size and cell type on the overall flatness of the mirror. As predicted by numerical models, mirrors with 25 um stiffening cells were flatter than those with 50 um cells; and mirrors fabricated with square cells were flatter than those fabricated with hexagonal cells. The surface deformation remained below 1 um across the 1.5 mm diameter for all mirrors. In the case of the 25 um square cells the surface curvature was not measurable with our current surface profilometer.

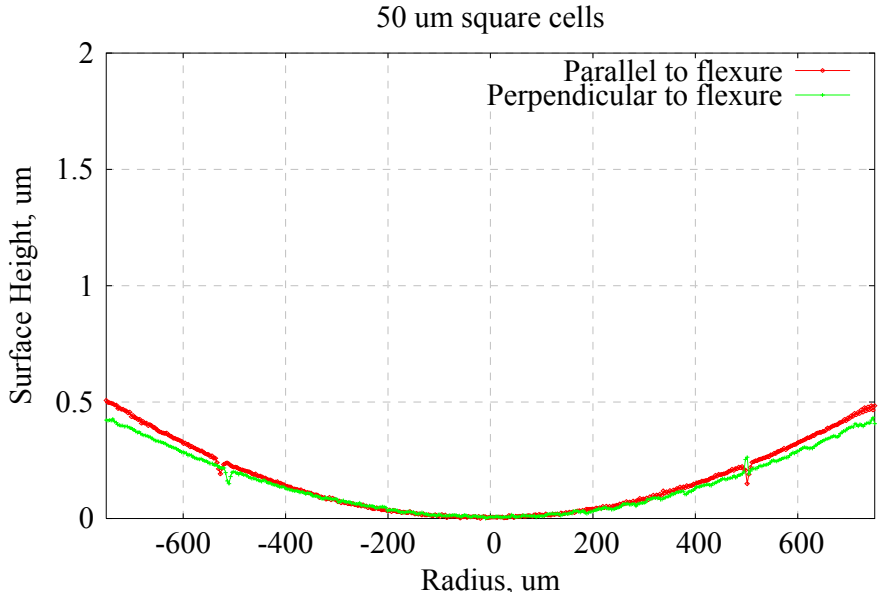


Figure 65 This figure shows the curvature across a 1500 um diameter single axis scan mirror stiffened with 50 um square cells. The surface profiles are measured parallel and perpendicular to the flexure axis.

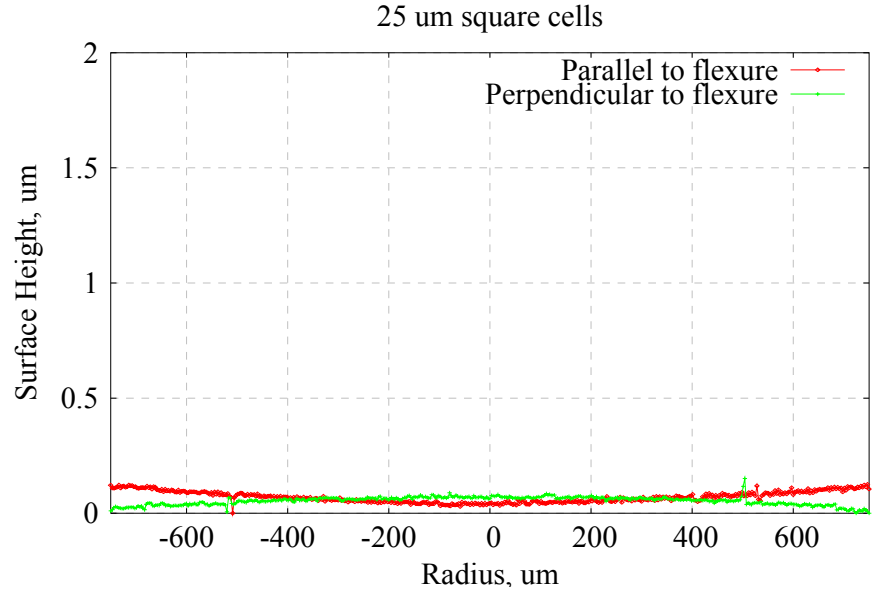


Figure 66 This figure shows the curvature across a 1500 um diameter single axis scan mirror stiffened with 25 um square cells. The surface profiles are measured parallel and perpendicular to the flexure axis.

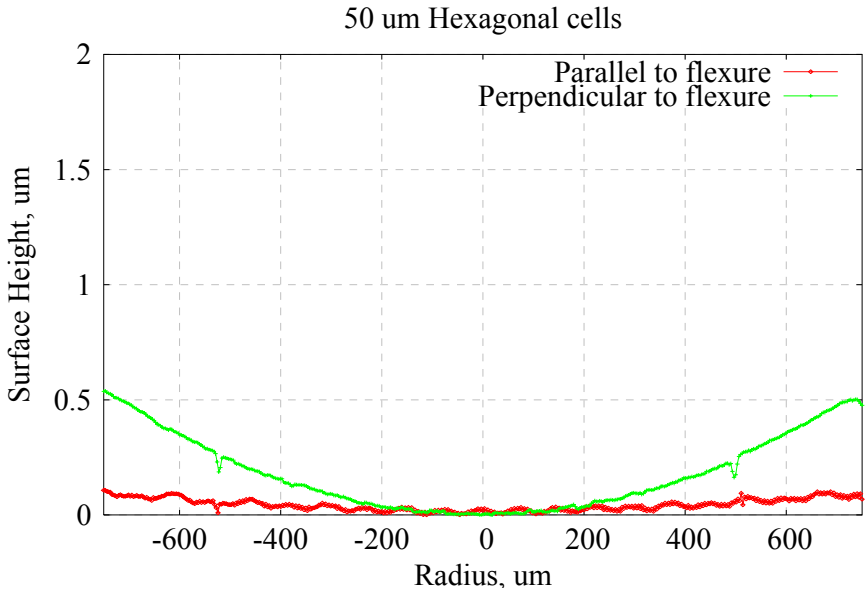


Figure 67 This figure shows the curvature across a 1500 um diameter single axis scan mirror stiffened with 50 um hexagonal cells. The surface profiles are measured parallel and perpendicular to the flexure axis.

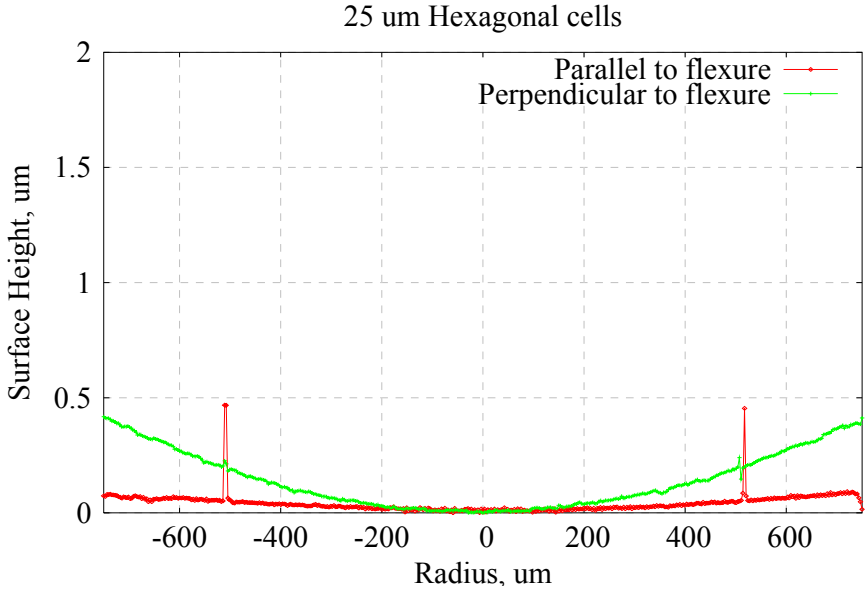


Figure 68 This figure shows the curvature across a 1500 um diameter single axis scan mirror stiffened with 25 um hexagonal cells. The surface profiles are measured parallel and perpendicular to the flexure axis.

While post-release thermal strain can be incorporated into the numerical models, it is clear that there are additional variables attributing to the static shape of the mirror surfaces. One explanation for the astigmatism as well as the upward bow in the 25 um square cell mirror is that the composite material is buckling due to the post-release thermal strain. As mentioned previously, this curvature may also be due to a density gradient through thickness of the film. The numerical models are currently incapable of predicting such behavior.

Dynamic Deformation

Surface deformation due to inertia can degrade the resolution of micro-scan mirror. An inertial load can be calculated for the rotating mirror and applied to the mirror in a static analysis. The inertial load in terms of distance from the flexure axis is derived by first multiplying the angular acceleration of the plate by the distance from the flexure axis of the plate giving the acceleration as a function of distance from the flexure axis. Multiplying this value by the product of the mass density of the plate and the thickness of the plate yields an equation for the force-per-unit area. The equation for the distributed load, q, is given below:

$$q = \ddot{\theta}\rho t y \,. \tag{36}$$

In the above equation $\ddot{\theta}$ is the angular acceleration of the mirror, ρ is the mass density of the plate material, t is the mirror thickness and y is the perpendicular distance from the

flexure axis. The angular acceleration is $\ddot{\theta} = \frac{\theta_o \omega^2}{2}$, where θ_o is the maximum mechanical rotation of the mirror and ω is the oscillation frequency of the mirror.

The torsion resonant frequencies of the single axis scan mirrors tested in this research ranged between 300 Hz and 500 Hz. However, before the distributed load due to inertia can be calculated for these mirrors the average mass density per unit volume is need for the stiffened film. The average mass density is determined by the product of the volume fraction of the material per unit cell times the mass density of the material. The volume fractions for square and hexagonal cells are shown below.

$$Vf_{square} = \frac{t(a+4h)}{a(t+h)} \quad . \tag{37}$$

$$Vf_{hex} = \frac{\sqrt{3}}{3} \frac{5ath + \frac{a^2 t}{2}\sqrt{3}}{a^2 (t+h)} \quad . \tag{38}$$

Using a film thickness of 1.4 um a cell size of 50 um, a cell height of 37 and a film density for silicon nitride of 3100 kg/m^3 the average mass density for the 50 um square cell material is 448 kg/m^3. The average mass density for a mirror fabricated with 50 um square cells oscillating at 500 Hz results in an equivalent inertial load at its peak mechanical rotation (10 degrees) of:

$$q = \frac{\pi}{18} 448 (2\pi 500)^2 (37 + 1.4) y = 2.96e10 y \quad . \tag{39}$$

The Figure below shows the predicted surface profile across one half of an un-stiffened single axis mirror due to calculated inertial load. Even for this relatively

compliant mirror inertial effects at 500 Hz are insignificant compared with the surface deformation due to post-release thermal strain and electrostatic actuation.

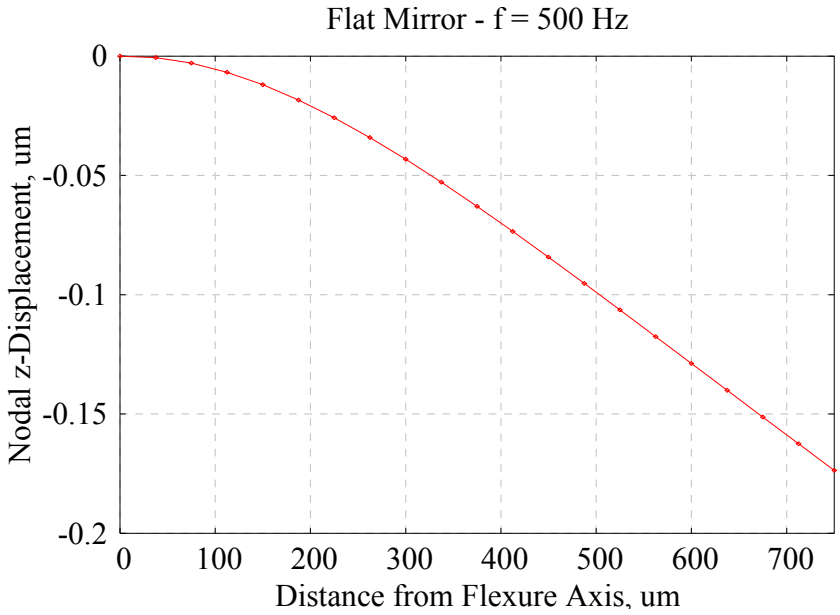


Figure 69 This figure shows the surface deformation due to inertia at 500 Hz across half of a single axis scan mirror measured perpendicular to the flexure axis.

Clearly inertial effects at this frequency range should not affect the surface profile of the stiffened single axis scan mirrors. The plots below verify this assumption. Figures 70 and 71 show measured surface profiles taken at the resonant frequency of the mirror. The resonant frequency for the 25 um square stiffened mirror was 400 Hz and the resonant frequency of the 50 um Hexagonal stiffened mirror was 530 Hz. The data was collected with a strobed, phase-shift profilometer. The initial curvature in the mirror is due to post-release thermal strain. Surface deformation due to inertial effects was not detectable in either of the data sets corresponding to the plots below.

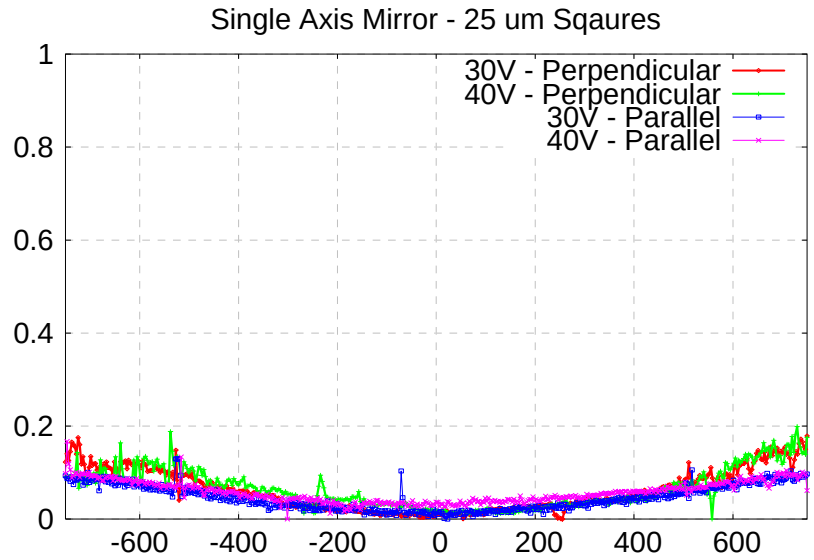


Figure 70 This figure shows the dynamic deformation of a single axis scan mirror stiffened with 25 square cells. The measurements were taken for 30 and 40 volts with a sinusoidal drive function at 400 Hz. Curvature was measured across the mirror parallel to the flexure axis and perpendicular to the flexure axis.

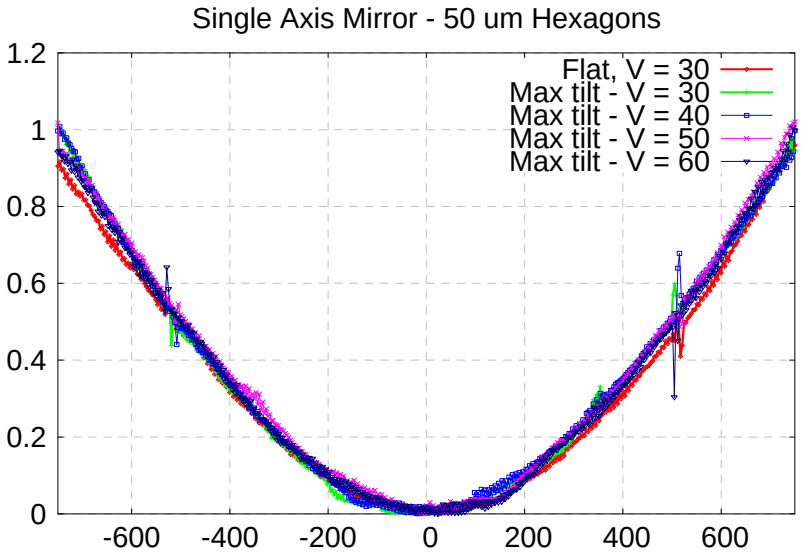


Figure 71 This figure shows the dynamic deformation of a single axis scan mirror stiffened with 50 um hexagonal cells. The measurements were taken for 30, 40 and 50 volts with a sinusoidal drive function at 530 Hz. Curvature was measured across the mirror perpendicular to the flexure axis.

Ideally, however, these mirrors would be actuated at a much higher frequency. As an example design case simplified numerical models of the 50 um square celled single axis mirrors are used to determine the frequency at which inertia in the film produces a peak-to-trough surface deformation in excess of lambda by 10 with lambda equal to 1550 nm. The plot below shows that for this design case the maximum actuation frequency with 10 degrees of rotation is just under 15 kHz. Of course this value can be significantly improved by decreasing the cell breadth and increasing the fin depth.

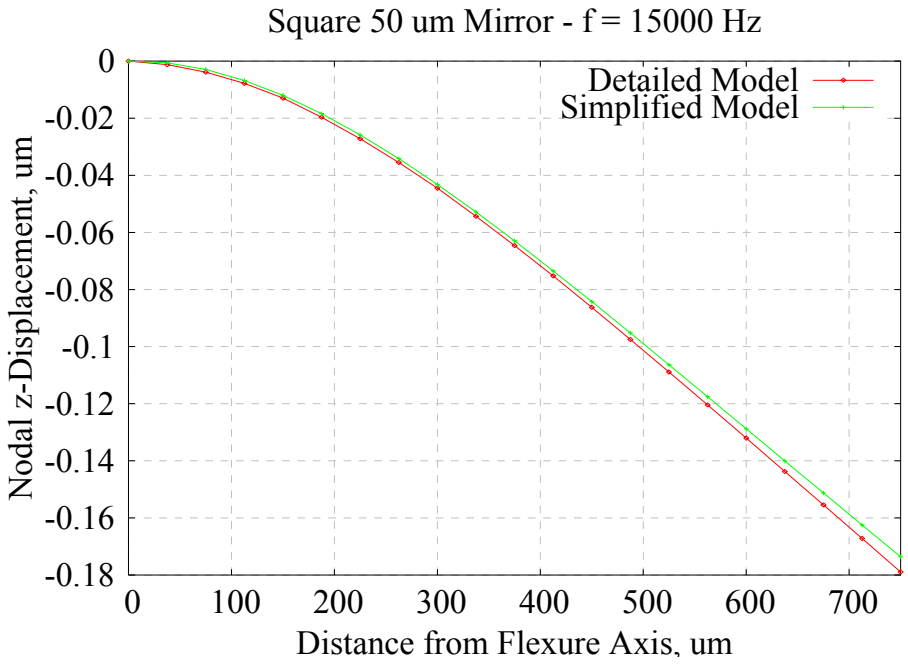


Figure 72 This figure shows the simulated surface deformation for single axis scan mirror stiffened with 50 um square cells oscillating at 15 kHz with a maximum rotation angle of 10 degrees.

Chapter Summary

A layered shell element was used to successfully simulate single axis scan mirrors. Several load configurations were simulated with the proposed material. Static

and dynamic analyses were performed to investigate the effects of post-release thermal strain, electrostatic force and inertia on the surface deformation of the mirrors. The results of the simplified numerical models were found to agree well with detailed numerical models and experimental results. The agreement between simplified models, detailed models and experimental results shows that simplified models employing layered shell elements can adequately simulate the mirrors primarily loaded in bending while reducing model complexity and computation time.

The example design case in the Dynamic Deformation section of this chapter illustrates the utility of simplified models. While the detailed model for this design case had a relatively simple geometry, it required almost twice as much processor time to solve. However, the simplified models become increasingly more attractive as the geometric complexity and/or cell density increases.

The proposed simplification method has been shown to be viable for first-order analysis of complex models. The simplified material model allows the cell type and geometry to be easily modified in a finite element model without requiring modification to the physical finite element model. This technique is ideal when designing and optimizing models with complex geometries that employ periodically stiffened thin films as a primary structural material.

CHAPTER 8

DISCUSSION AND CONCLUSION

This research has addressed the challenge of designing and fabricating MEMS using periodic rib-reinforced thin films. A novel fabrication technique to produce the stiffened film was presented. The resulting material retained the excellent optical and electrical properties of a traditional LPCVD silicon nitride film with the added benefit of increased rigidity. A simplified numerical model of the stiffened film was also presented. The model was able to account for cell size, cell type, fin thickness and fin height.

The challenges of designing and fabricating MEMS form the proposed stiffened film were addressed by approaching the research in two phases. First, the fabrication technique was developed in a series of design/build iterations using micro mirrors and micro cantilevers as test devices. Numerical models were then developed that were capable of predicting the behavior of the MEMS fabricated with the film. The models were validated with the experimental devices fabricated in the initial design phase. The models relied on an averaging technique that allowed the cellular material to be treated as a homogeneous material. This assumption simplified model complexity and decreased computation time. Simulations of experimental devices using the proposed simplified models showed that the simplified modeling technique is ideally suited for first-order analysis of MEMS fabricated from the proposed stiffened film especially when designing devices with complex geometries in which several cell types and sizes must be considered.

Fabrication Discussion

The fabrication process presented in this research represents a novel technique to produce a structurally stiffened LPCVD silicon nitride film. A detailed fabrication procedure has been given to create a mechanically stiffened thin, 1.5 um, film of silicon nitride, with nearly arbitrary control over the depth and pattern of the vertical stiffening fins. The resulting material is both rigid and lightweight. The combination of bulk and surface micro-machining techniques makes the presented technique simple requiring only a few additional steps to produce the stiffening ribs responsible for the increased stiffness and strength-to-weight ratio.

As noted in Chapter 3, residual oxide can have a significant effect on film curvature, even in the presence of deep stiffening ribs. The removal of all residual oxide in the film after it has been release from the substrate is vital if a low-stress, flat film is desired. Additionally, the temperature at which the nitride is deposited should be kept as low as possible to reduce the post-release thermal strain in the material after it has been deposited and cooled.

Fabrication Limitations

The proposed fabrication technique has some limitations with regard to geometry and film thickness. While almost any cell type with vertical sidewalls can be fabricated, the size of the cell is limited in two ways. First, the depth of the cell is limited by the rate at which the ammonia and dichlorosilane can penetrate the trenches. While this limit was not observed in the current test devices with ribs as deep as 50 um, it may become apparent at anything beyond 50 um if the fin width is kept near 3.0 um or less. Second,

the cell breadth is limited by the etchant used to remove the silicon form the cells. If an anisotropic etchant is used then the rate at which silicon is removed from the cells can be driven by the etch rate on the (111) plane of the silicon which is significantly slower than the (100) etch rate. This case is illustrated in the figure below:

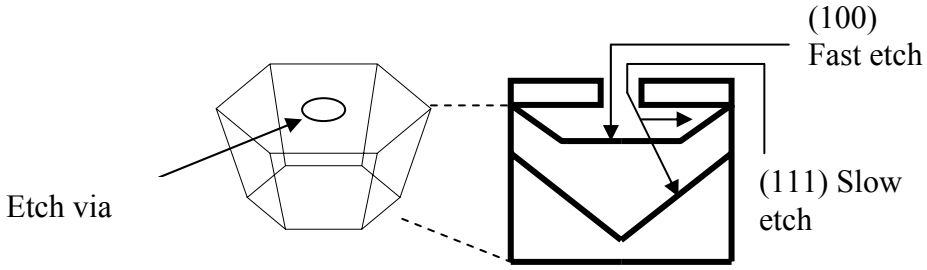


Figure 73 This figure shows the how cell size can limit the etch in an anisotropic etch.

Mirror Discussion

Surface deformation due to post-release thermal strain and inertia remained below 1 um across the 1.5 mm diameter for all the single axis scan mirrors tested in this research. In the case of the 25 um square cells the static surface curvature was not measurable with our current surface profilometer. Surface deviation due to inertial forces was not measurable with our current testing equipment and is suspected to be less than 10 nm for actuation frequencies at or near resonance for 25 um square and 50 um hexagon stiffened mirrors.

Ultimately, the periodic rib-reinforced LPCVD silicon nitride was shown to be a viable and efficient material to use in the fabrication of large area scan mirrors. The film has a high strength-to-weight ratio and can be easily fabricated using modern

microfabrication techniques. When molded into a 25 um and 50 um square and hexagonal periodic pattern the rib-reinforced film was shown to minimize surface curvature due to post-release thermal strain across a 1.5 mm diameter mirror to less than 1 um. Surface deformation due to dynamic actuation was found to be less than 10 nm. Although limited to micro mirror fabrication in this research, this structurally enhanced film can be applied to almost any MEMS where a lightweight material with a high flexural rigidity is desired.

Mirror Limitations

The main limitation with the proposed mirrors is in the surface of the nitride where the sidewalls of the fins are closed off. These patterns lead to diffraction of a focused beam when reflected off the surface of the mirror. This limitation can be rectified by applying a chemical-mechanical polish to the topside of the wafer to smooth the top of the mirror.

Modeling Discussion

A layered shell element was used to simulate single axis scan mirrors under several load configurations. Static and dynamic analyses were performed to investigate the effects of post-release thermal strain, electrostatic force and inertia on the surface deformation of the mirrors. The results were found to agree well with detailed numerical models and experimental results. The agreement between simplified models, detailed models and experimental results showed that the simplified, layered models could adequately simulate mirrors while reducing model complexity and computation time.

The proposed simplification method was shown to be a viable first-order analysis technique. The simplified material model allows the cell type and geometry to be modified without requiring geometric modification to the finite element model. This simple and robust analysis technique can significantly simplify the design and optimization of MEMS fabricated from the proposed periodically stiffened thin film.

Modeling Limitations

While the proposed technique works well for first order analyses of complex MEMS fabricated with periodically stiffened thin films, the technique is most applicable for structures loaded primarily in bending. This limitation is due to the composite nature of the material and is illustrated in Chapter 6. However, the proposed technique can significantly reduce analysis time by allowing several cell configurations to be considered quickly during the design phase of a MEMS fabricated with periodically stiffened thin films. Once a cell configuration has been established, a fully detailed model can be used as a final refined analysis.

Future Work

Modeling Refinements

Closed-form solutions for the bending stiffness, flexural rigidity and effective Young's modulus for the cell layer of finite element layers are needed. Equations for these values in terms of dimensionless parameters are currently under investigation. These equations could then be used to quickly obtain values for the stiffness of the film

as a function of cell geometry without needing to first simulate a detailed sample or rely on curve fitting techniques.

Self Assembled Devices

A relatively new and exciting area of MEMS research worth mentioning is self-assembled devices. Several attempts have been made to reconfigure MEMS into fully 3-D structures using thermal mechanisms, post-release thermal strain, foldout hinges and most recently, surface tension-power (Bright et al). These techniques still rely on thin materials as the primary structural material resulting in compliant 3-D structures. As useful devices are designed and fabricated with these methods, deformation of the structural material due to post-release thermal strain and arbitrary acceleration must be considered. Although not addressed in detail in this research, stiffened thin films may also be appropriate for MEMS fabricated with the reconfiguration techniques mentioned above.

Conclusion

Periodic stiffeners were shown to significantly increase the bending stiffness of LPCVD silicon nitride films while achieving a high strength-to-weight ratio. Larger aperture, silicon nitride micro mirrors were fabricated with the mechanically stiffened silicon nitride film. The film adequately controlled deformation due to post-release thermal strain and inertial effects. The silicon nitride film was successfully modeled as a layered composite material yielding accurate simulations for biaxial and single axis torsion mirrors at a reduced computational cost. Fabrication of the mirrors was achieved

with a minimal amount of processing making the proposed microfabrication technique an attractive solution for various MEMS applications. Numerical analyses were shown to simplify model complexity while simultaneously reducing the computational cost associated with simulating MEMS build from a periodically stiffened thin film.

REFERENCES

[1] V. A. Aksyuk, F. Pardo, C. A. Bolle, S. Arney, C. R. Giles, D. J. Bishop, "Lucent Microstar Micromirror Array Technology for Large Optical Crossconnects," Proceedings of SPIE, 4178, pp. 320-324, 2000.

[2] I. V. Andrianov and L. I. Manevich, "Shell design using the homogenization method," *Uspekhi Mekh.,* vol. 6, pp3-29, 1983.

[3] M. Artolaand G. Duvaut, "Homogeneisation d'une plaque reinforcee," *C.R. Acad, Sci., Ser,* vol 284, pp. 707-719, 1977.

[4] A. Bensoussan, , J. L. Lions and G. Papanicolaou "Asymptotic analysis for periodic structures", vol. 5, 1978.

[5] Stein A. Berggren, Dag Lukkassen, Annette Meidell and Leon Simula, " Some methods for calculating stiffness properties of periodic structures," *Applications of Mathematics,* vol. 48, n. 2, p 97-110, 2003.

[6] J. Buhler, F.P. Steiner, and H. Bates, "Silicon dioxide sacrificial layer etching in surface micromachining", *Journal of Micromechanical microengineering*, 7, 1997, pp. R1-R13

[7] G. Duvaut "Analyse fonctionnelle et mechanique de milieux continues. Application a l'etude des materiaux composites elastiques a structure periodique – homogeneisation," *Theoretical and Applied Mechanics Proceedings of the 14th IUTAM congress.* pp. 11-132, 1976.

[8] G. Duvaut and A. M. Metellus, "Homogeneisation d'une plaque mince en flexion de structure periodique et symetrique," *C. R. Acad, Sci., Ser* vol. 283, pp. 947-950, 1976.

[9] L.J. Gibson and M. F. Ashby, "Cellular Solids – Structure and Properties," Oxford: Pergamon, 1988.

[10] Staffan Greek and Nicolae Chitica, "Deflection of surface-micromachined devices due to internal, homogeneous or gradient stresses," *Sensors and Actuators*, vol. 78, p. 1-7, 1999.

[11] H. Guckel, D. Burns, C. Rutigliano, E. Lovell, B. Choi, "Diagnostic microstructures for the measrurement of intrinsic strain in thin films," *J. Micromechanics and Microengineering*, vol. 2, p. 86-95, 1992.

[12] Dan Haronian and Noel D. MacDonald. “Spring suspended corrugated membranes,” *Journal of Micromechancis and Microengineering,* vol. 5, p 289-296, 1995.

[13] Phillip A. Himmer, “Silicon nitride deformable mirrors for focus and spherical aberration correction in micro-optical systems,” Ph. D. Dissertation, Montana State University – Bozeman, 2002.

[14] L. J. Hornbeck and W. E. Nelson, “Bistable Deformable Mirror Device,” *OSA Technical Digest Series, Vol. 8, Spatial Light Modulators and Applications*, 1998, p. 107.

[15] David A. Horsely, Angad Singh, Albert Pisano and Roberto Horowitz, “Angular micropositioner for disk drives,” *Proceedings 10th Annual International Workshop on Micro Electro Mechancial Systems (MEMS ’97)*, p 72-77, 1997.

[16] J. H. Jerman , “Fabrication and use of micromachined corrugated silicon diaphragms,” *Sensors and A Sensors and Actuators, A: Physical*, v 23, n 1-3, Apr, 1990, p 988-992.

[17] C. G. Keller and R. T. Howe, “Hexsil bimorphs for vertical actuation,” *Proceedings 8th Conference on Solid State Sensors and Acutators IX*, vol. 1, p. 99-102, 1995.

[18] C. G. Keller and R. T. Howe, “Hexsil tweezers for teleoperated micro-assembly,” *Proceedings 10th Annual International Workshop on Micro Electro Mechancial Systems (MEMS ’97)*, p 72-77, 1997.

[19] S. Kelsey, R. A. Gellatly, B. W. Clark, “The shear modulus of foil honeycomb cellular cores,” *Aircraft Engineering,* vol. 30, p. 294-302, 1958.

[20] G. T. A. Kovacs, “Micromachined Transducers Sourcebook,” McGraw-Hill, 1998.

[21] H-Y Lin, M. Wu and W. Fang, “The improvement of micro-torsional-mirror for high frequency scanning,” *MOEMS Miniature Systems*, vol. 9178, pp. 98-105., 2000.

[22] H-Y Lin, M. Wu and W. Fang, “A rib-reinforced micro torsional mirror driven by electrostatic torque generators,” *Sensors and Actuators*, vol. 105, n 1, pp. 1-9, 2003.

[23] B. Jeffrey Lutzenberger, David L. Dickensheets; Todd J. Kaiser. Large area molded silicon nitride micro mirrors. *Photonics Technology Letters, IEEE*, v 15:10, October 2003, p. 1407-1409.

[24] B. Jeffrey Lutzenberger, David L. Dickensheets, Vertical stiffening members for flatness control of surface micromachined structures. *Proceedings of SPIE - The International Society for Optical Engineering*, v 4561, 2001, p 238-246.

[25] MEMS and Nanotechnology Clearinghouse, 1895 Preston White Drive, Suite 100, Reston, Virginia 20191. www.memsnet.org.

[26] R. S. Muller, R. T. Howe, S. D. Senturia, R. L. Smith, and R. M. White, "Microsensors," IEEE Press, New York, MY, 1991.

[27] Lilac Muller, R. T. Howe, Albert P. Pisano, "High-aspect-ratio, molded microstructures with electrical isolation and embedded interconnects," *Microsystem Technology,* vol. 7, p. 47-54, 2001.

[28] V. Z. Parton and B. A Kudryavtsev, "Use of homogenization method in the design of ribbed plates and shells with regular structure," *Probl. Prochn.,* vol. 8(b), 101-106, 1988.

[29] C. Serre, A. Perez-Rodriguez, J. R. Morante, P. Gorostiza and J. Esteve, "Determination of micromechanical properties of thin films by beam bending measurements with an atomic force microscope," *Sensors and Actuators, A: Physical*, v 74, n 1-3, Apr, 1999, p 134-138.

[30] G. Shi and P. Tong, "The derivation of equivalent constitutive equations of honeycomb structures by a two scale method," Computational Mechanics, v 15, p. 395-407, 1995.

[31] G. Shi and P. Tong, "Equivalent transverse shear stiffness of honeycomb cores," *International Journal of Solids Structures,* vol. 32, n. 10, p. 1383-1393, 1995.

[32] J. R. Vinson and R. L. Sierakowski,"The behavior of structures composed of composite materials," Boston, Kluwer Academic, 1990.

[33] Bing Xu, Francisco Arias, George M. Whitesides, "Making honeycomb composites by soft lithography," *Advanced Materials,* vol. 11, n. 6, p. 492-495, 1999.

[34] Xin Zhang, Tong-Yi Zhang, Yitshak Zohar, "Measurements of residual stresses in thin film using micro-rotating-structures," *Thin Solid Films*, v 335, p. 97-105.